Probing the effect of oxygen vacancies in strontium titanate single crystals

Shams ur Rahman
Linacre College
University of Oxford

A thesis submitted for the degree of

Doctor of Philosophy

Hilary Term 2014

Abstract

This thesis describes investigations into the role of non-stoichiometry in the surface and bulk properties of $SrTiO_3$ single crystals. A family of (n×n) reconstructions, where n = 2, 3, 4, 5, 6 are produced by argon ion sputtering of the $SrTiO_3$ (111) single crystals and subsequent annealing in UHV or in an oxygen rich environment. The sputtering process introduces defects or oxygen vacancies in the surface region of the sample, whilst the annealing gives rise to surface reconstructions. The surface preparation conditions such as sputtering time, annealing temperature and environment are optimized to obtain various reconstructions in a controlled and reproducible manner. High resolution STM images of these reconstructions are also obtained and utilized in the investigation of the surface reactivity. Fullerene molecules are deposited on the reconstructed surfaces to elucidate the surface reactivity through template assisted growth. Fullerene molecules are first deposited with substrate surfaces held at room temperature. Being the most highly reduced among the (n×n) family, the 5×5 reconstruction significantly influenced the growth of fullerenes. Both C_{60} and C_{70} adsorb as individual molecules and produce clusters with magic numbers. The 4×4 and 6×6 reconstructed surfaces encourage the formation of close-packed structures upon the deposition at room temperature. When the surface covered with fullerenes is heated to a temperature of around 200 °C, epitaxial islands are observed. The 6×6 reconstructed surface appeared to be less reactive than the 4×4.

Electrical transport, cathodoluminescence (CL) and electron spin resonance (ESR) experiments are also carried out to investigate the effect of oxygen vacancies on the bulk properties of UHV annealed $SrTiO_3$ single crystals. Thermal reduction leads to carrier doping of the material, which not only gives rise to electrical conduction but also induces room temperature luminescence. Both the electrical conductivity and CL intensity increases with annealing time. The work presented in this thesis provides insight into the defect driven properties in both the surface and bulk of $SrTiO_3$ single crystals, which could play an important role in the development of oxide-based electronic devices.

Preface

The work described in thesis was carried out by the author under the supervision of Prof. M. R. Castell. It has not been previously submitted for a degree at this or any other university.

Acknowledgments

The completion of this thesis would not have been possible without the immense support of many generous people around me. I feel privileged to avail this opportunity to owe a huge thanks to everyone who helped and encouraged me throughout this work.

First and foremost, I would like to express my heartfelt special gratitude to Prof. Martin R. Castell for giving me the opportunity to work in this exciting field of research. I was so fortunate to have Martin as my supervisor who has always been motivating, encouraging, and enlightening since the day this project started. During the project, Martin was always there to provide me with every bit of guidance, expertise and valuable suggestions when necessary. He persuasively conveyed an interest in my work, and I am grateful for the precious time he dedicated to both my personal and academic development. His patience, flexibility, genuine caring and concern, and valuable feedback enabled to achieve this milestone. I am also deeply indebted to Martin for providing me with the opportunity to attend different conferences, to present my results to an international audience.

Completing this work could not have been achieved without the immense support of my colleagues and collaborators, who gave me the opportunity to learn from their experience. I am greatly indebted to Olga Shvarova, Jingyu Sun for teaching me the use of STM machines belonging to our group. Many thanks to Chen Wu, Xiao Hu, Yakun Gao and Merel Lefferts who made my time in Oxford very special. I would like to express my sincere gratitude to Kyriakos Porfyrakis for his immense support and providing me with fullerene molecules. I deeply acknowledge the support of Richard George, who has been extremely helpful and knowledgeable figure. I owe a huge thanks to him for helping me to analyse the ESR results and setup different experiments in the CAESR laboratory. Furthermore, I am grateful to him for proof reading parts of this thesis and his valuable suggestions on improving the writing. I would like to extend my gratitude to Arzhang Ardavan and Jeffrey Harmer for their support and giving me access to the CAESR. I owe special thanks to Chris Salter for his valuable time in assisting me with the CL measurements. I am greatly indebted to Naureen Akhtar for performing the electrical measurements on my samples. I highly appreciate all her intellectual contributions, fruitful scientific discussions and incredible support throughout this doctorate.

I would like to express my utmost gratitude to Chris Spencer, the JEOL engineer, who has been extremely helpful in fixing the STM machines whenever it was required. The Surface Nanoscience group is very lucky to have Chris as support. I cannot thank him enough for his incredible support and the time we spend together during his visits. In addition, I am greatly indebted to the departmental support staff, one of the best in the world. Adrian Taylor, Marion Beckett, Paul Warren, Lyn Richmond, Barry Fellows,

Rebecca Bradford, Peter Flaxman, Richard Cripps, Chris Akinola and Khalid Schofield have lent an immense support during the entire period to make my life easier at Oxford.

I am grateful for funding from the COMSATS Institute of Information Technology (CIIT) Pakistan, which covered my tuition fees and other expenses for three years. I am extremely grateful to Linacre College not only for giving me financial support in difficult times, but also for providing me the opportunity to be part of a great social community. I would like to express my sincere gratitude to Jackie Favarin for her incredible support since the very first day. I am also very grateful to my college advisors, Aleksey Kolmogorov and Shonil Bhagwat, for their immense support and valuable advice regarding my future career.

Of course no acknowledgments would be complete without giving tremendous and deep thanks to my family who have given me the motivation, confidence and support throughout this DPhil. My parents, especially, have believed in me and supported my decisions. There are no words that can express my appreciation for their love, support and sacrifices that enabled me to stand where I am today.

Contents

Chapter 1

Introduction

1.1 Background

Strontium titanate ($SrTiO_3$) belongs to the family of perovskite oxides, and has stimulated ongoing interest for its wide range of intriguing properties. Paradigmatic examples include blue light emission [1], photovoltaic effect [2, 3], magnetism [4, 5], strain induced ferroelectricity [6], photoconductivity [7], superconductivity [8], and so on. At room temperature it has a simple cubic structure with a lattice parameter of 3.905 Å and formal ionic charges of Sr^{2+}, O^{2-} and Ti^{4+} [9]. In a typical unit cell of $SrTiO_3$, Ti ions occupy the cube corners, Sr ion at the centre and O are at the midpoint of the cube edges. Stoichiometric $SrTiO_3$ is a good insulator having a band gap of 3.2 eV [10], and is an easily functionalizable material. In recent years, the formation of two dimensional electron gas (2DEG) at the interface between $SrTiO_3$ and $LaAlO_3$ [11] has motivated further scientific endeavours to elucidate several fascinating phenomena. For instance, though $SrTiO_3$ and $LaAlO_3$ are both insulating and diamagnetic, their interface has been suggested to exhibit superconductivity [12], photoconductivity [13], ferromagnetism [14] as well as the co-existence of both superconducting and ferromagnetic behaviour [15, 16]. Moreover, an insulator-to-metal transition that can be reversibly controlled through the application of an electric field has also been reported

[17]. Such intriguing properties of the $SrTiO_3/LaAlO_3$ interface make it a promising material for many novel applications including spintronics, high electron mobility field effect transistors and oxide electronics [18-22].

The $SrTiO_3$ surface has been the subject of intense research because of a multitude of remarkable properties. The $SrTiO_3$ surface itself is an excellent platform material for the growth of high temperature superconductors [23], metal nanocrystals [24], epitaxial islands of anatase TiO_2(001) [25] and so on. Complementing the scientific endeavours in surface science, the surface of $SrTiO_3$ is full of surprises and challenges our understanding by giving a plethora of exceptional properties by accommodating a range of non-stoichiometric surface structures [26]. In the last few decades, there has been a rapidly growing appreciation of the role of non-stoichiometry in the surface properties of $SrTiO_3$. Argon ion beam bombardment of the $SrTiO_3$ surface generates non-stoichiometry in the vicinity of the surface layers leading to a high defect density in the surface/near surface region of the crystal. As a result of surface modification, interesting PL emissions have been reported at room temperature [1]. Moreover, annealing the sputtered surfaces results in the formation of reconstructions and even surfaces decorated with nanostructures [27-29]. The nature of the surface structures is dependent on the surface preparation conditions such as annealing temperature, annealing time, whether the specimens are annealed in an ultra-high vacuum (UHV) or an oxidizing environment, sputtering and etching. In order to further explore and design new functionalities, the $SrTiO_3$ surfaces have been used to order fullerene molecules and other functional materials [30-32].

The role of non-stoichiometry is not only limited to the surface properties of $SrTiO_3$. Instead, the physical and chemical properties of this material can also be strongly modified through a controlled introduction of bulk defects. The structure of $SrTiO_3$ is highly flexible, and can accommodate a range of non-stoichiometry or dopant

concentration. For example, doping with transition metals or oxygen vacancies can lead to various properties ranging from magnetism [33-35] to luminescence [36]. These intriguing properties of $SrTiO_3$ have spurred the research community to utilize its capabilities for oxide-based electronic devices [37, 38]. In addition to the magnetic properties, the electrical properties can also be strongly modified through electron doping. It becomes semiconducting and even metallic when chemically doped with electron donor or acceptor species e.g. when doped with Nb, it becomes n-type semiconductor [39]. Electron doping through the introduction of oxygen vacancies can also lead to a metallic behaviour of the material. The oxygen vacancies can easily be incorporated through various processes such as ion bombardment and annealing in a reducing atmosphere.

1.2 Plan of thesis

This thesis is based on studying and understanding the effect of non-stoichiometry on the structural and physical properties of $SrTiO_3$ single crystals. The non-stoichiometry is introduced through the Ar^+ ion sputtering or annealing of the samples in a reducing environment. A range of surface reconstructions on $SrTiO_3$(111) surface have been reported previously that are produced through Ar^+ ion sputtering and subsequent annealing in UHV or in an oxygen rich environment [29]. The reconstructed phases are often found to coexist on the $SrTiO_3$(111) surface, and obtaining a mono-phased surface with required reconstruction remains an elusive target. Moreover, investigation of the surface reactivity of these surface phases is of vital importance for their utilization in the growth of functional materials for technological applications. The $SrTiO_3$(111) surface in the present work is studied in detail in the context of producing the reconstructed phases in a controlled and reproducible way. The surface reactivity of different reconstructed phases is also addressed through the deposition of large guest molecules. In this regard scanning tunnelling microscopy is a powerful technique that

provides an opportunity to obtain real space images of the reconstructed surfaces at the atomic scale. The atomic resolution images are essential not only for identifying the specific adsorption sites of adsorbates but also for the development of theoretical models that could extend our knowledge behind many fascinating phenomena at the surface.

Oxygen vacancies also play a dominant role in altering the bulk properties of the material. They generate additional electronic levels within the bandgap of the material and hence modify its electrical transport and luminescence behaviour. Although there is a significant body of literature on physical properties of oxygen deficient $SrTiO_3$, understanding the nature and underlying mechanisms of oxygen vacancy defects is still the subject of intense research which is of vital importance in controlling and tuning the corresponding properties. Part of the thesis is devoted to develop an understanding of the role of bulk defects in modulating the structural, electronic and optical properties of $SrTiO_3$ single crystals. The structure of the thesis is as follows:

Chapter 2 provides an introduction to the characterization techniques that are used to carry out the research work presented in this thesis.

Chapter 3 gives an overview of the previous research contributions that broadly span the defect driven properties of $SrTiO_3$. The review begins with a brief overview of several types of surface reconstructions reported on the $SrTiO_3$(111) surface. The influence of $SrTiO_3$ reconstructed surfaces on the arrangement of fullerene molecules is also discussed. In addition, the ordering of fullerene molecules on semiconducting surfaces is outlined. Such work is of significant importance in delineating the influence of template surface on self-assembly of molecules as well as for the development of molecular based technological applications. Moreover, the electrical transport, ESR and luminescence properties of the $SrTiO_3$ are also reviewed.

Chapter 4 presents a systematic STM study of the family of (n×n) type reconstructions on $SrTiO_3$(111) surface. Surface reconstructions are produced in a controlled way such that different reconstructed phases evolve from each other by simply varying the processing parameters. High resolution STM images are shown and utilized to identify the adsorption sites for large guest molecules.

Chapter 5 concerns the elucidation of surface reactivity of $SrTiO_3$(111) reconstructed surfaces through the deposition of fullerene molecules with samples held at room temperature. The experiments are performed by taking STM images as a function of deposition time. The extent of bonding between molecules and surface is used to anticipate the surface reactivity. The 5×5 reconstructed surface arranged fullerenes into various exotic configurations, including individual adsorption and clusters with magic numbers.

Chapter 6 further extends the work to investigate the surface reactivity through templated ordering of fullerenes on the reconstructed $SrTiO_3$(111) surfaces. This is achieved through annealing of the substrate surface covered with fullerenes molecules. The extent of molecule-substrate interaction is envisioned to explore the reactivity of the reconstructed surfaces relative to each other.

Chapter 7 reports the effect of oxygen vacancies on the bulk properties of $SrTiO_3$ (001) single crystals. This includes a detailed study of the electrical and luminescence properties in combination with electron spin resonance spectroscopy (ESR) of the as-received and reduced single crystals.

At the end, a brief summary of the research work reported in this thesis along with an outlook of future research direction is given in **chapter 8**.

Chapter 2

Experimental Techniques

2.1 Background

Non-stoichiometry/defects play a crucial role in altering the physical and chemical properties of solid materials [40-44]. Quantifying and understanding the nature of defects and their influence on the properties of functional materials and devices have been of great interest for several decades [45, 46]. Defects at surfaces, in particular, play a vital role in determining the chemical and electronic properties and have attracted the attention of current research in the field of surface science to unravel various fascinating phenomena [47, 48]. Studies of the surface structures or properties that arise from surface defects require highly sophisticated tools. With the emergence of numerous techniques, fundamental properties of materials arising intrinsically or extrinsically have been better understood [49, 50]. For example, the discovery of scanning probe microscopes opened doors to the nanoworld by exploring the surface structures with atomic resolution and at the same time made it possible to detect various defects at the atomic scale that is not possible with other diffraction and spectroscopic techniques [47, 51]. Since then researchers all over the world, in the field of nanoscience, are trying to unravel nature's secrets by studying materials at the atomic scale [52].

Since the defect structure at the bulk of a material is different from that at the surface, it can also lead to various fascinating properties. Therefore, it is essential to choose the right techniques and methods to probe the corresponding defect induced properties of the material. For example, scanning tunnelling microscopy uses electrons to probe the surface structure of a material [53]. The chemical nature of a material surface can be studied with the help of spectroscopic techniques that uses highly energetic electrons to interact with the materials surface and are extremely sensitive to the topmost surface layers [49]. Similarly, electron spin resonance spectroscopy and other spectroscopic techniques such as cathodoluminescence, UV-Vis etc. can be used to study the bulk properties of materials. This chapter introduces the experimental techniques and methods employed to investigate the effect of non-stoichiometry, particularly oxygen vacancies, in $SrTiO_3$ single crystals.

2.2 Characterization techniques

2.2.1 Scanning tunnelling microscopy (STM)

2.2.1.1 The equipment

The majority of experiments reported in this thesis were carried out using ultra high vacuum (UHV) systems that operate at base pressures of 10^{-8} Pa. The Surface Nanoscience group at the Department of Materials is facilitated with three UHV systems. These are JSTM-4500XT, JSPM-4500S and JSTM-4500S which are designed by the Japanese Electron Optics Laboratories (JEOL) and described elsewhere in detail [54-58]. JSTM-4500XT and JSTM-4500S are equipped with a variety of surface and chemical characterization techniques including scanning tunnelling microscope (STM), scanning electron microscope (SEM), low energy electron diffraction (LEED), X-ray photoelectron spectroscopy (XPS) and Auger electron spectroscopy (AES) [54-56]. In addition, they are facilitated with Knudsen cells and electron beam (e-beam)

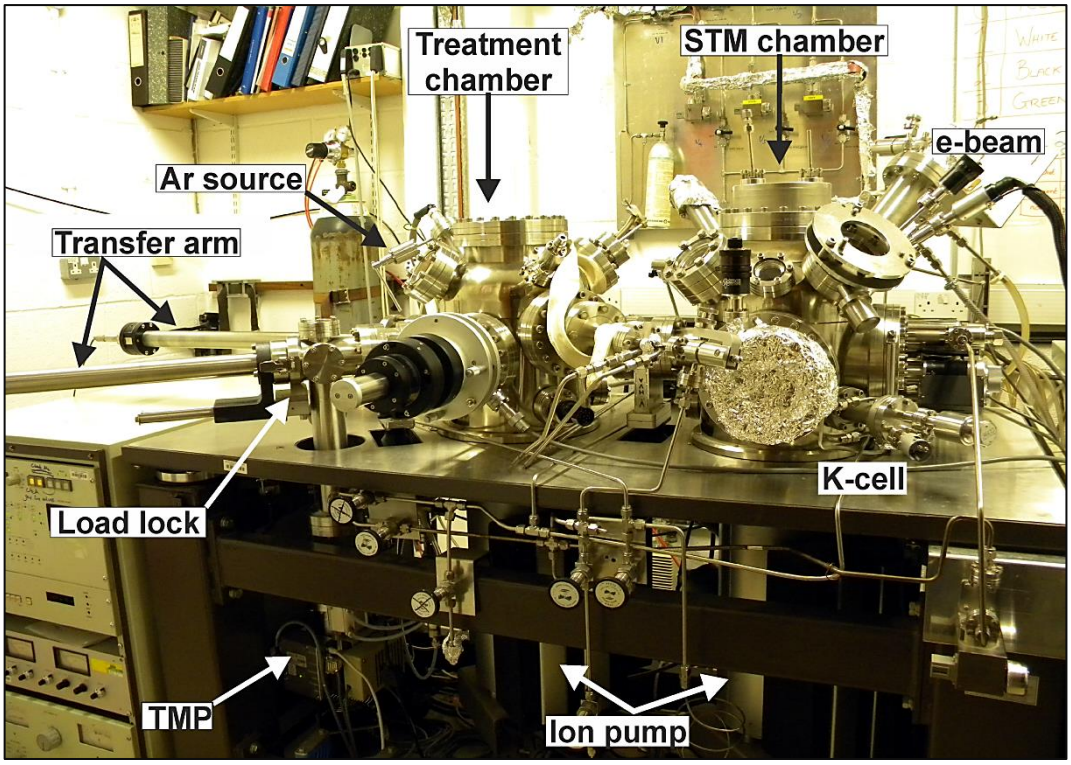

Fig. 2.1 Photograph of the JEOL designed JSTM-4500XT system, supported on an air table to create vibration isolation. Both the treatment and STM chamber operates in UHV with the help of ion pumps. Vacuum can be created in the load lock with the aid of TMP. Treatment chamber is used for specimen preparation and for LEED experiments. STM chamber is incorporated with two K-cells and an e-beam evaporator for the deposition of molecules and metals, respectively.

evaporators that allows the dosing of well controlled amount of molecules and metals on to the sample surface.

The JSTM-4500XT comprises two ultra-high vacuum (UHV) chambers as shown in Fig. 2.1. A specimen is first mounted on the transfer arm of the load lock which is pumped down to a pressure in the low 10^{-6} Pa range with the aid of turbo molecular pump (TMP). The sample can then be transferred from load lock into the treatment chamber that operates at a base pressure of 10^{-8} Pa with the help of an ion pump. The treatment chamber is mainly used for sample preparation such as degassing, sputtering and annealing. The sputtering of a sample can be performed with the help of PSP vacuum technology ion source ISIS3000 [59] attached to the treatment chamber. Degassing/annealing can be performed by resistively passing a current through the

sample. Once the sample is prepared, it can be checked with LEED to verify the surface reconstruction by obtaining the diffraction pattern or can be transferred into the STM chamber for imaging. The STM chamber is also equipped with an e-beam evaporator and two Knudsen cells for the deposition of metals and molecules, respectively.

The JSTM-4500S is also state of the art equipment. In addition to sample preparation and STM chamber, it contains a third chamber that is equipped with further characterization techniques [54]. The chamber contains a scanning electron microscope (SEM), model JSM-5600 [57]. Here it is possible to investigate the near surface chemistry by using the AES and XPS as well as the optical properties (Raman spectroscopy, photoluminescence and cathodoluminescence) of the specimens without exposing them to high pressures [54, 58]. Moreover, the UHV SEM imaging can also be performed. The STM chamber is equipped with a cryostat that allows performing the STM experiments at cryogenic temperatures.

2.2.1.2 Basic theory of STM

The scanning tunnelling microscopy (STM) was invented 1981 by Gerd Binning and Heinrich Rohrer, who reported the first atomic resolution images of reconstructed surfaces [60, 61]. In 1986, they received the Nobel Prize in Physics for their pioneering invention. After the invention of STM, the atomic force microscopy was developed to resolve the surface structure of non-conducting and conducting materials [51]. The invention of scanning probe microscopes have since become a real revolution and been widely employed techniques in the field of surface science [51, 52].

STM provides real space atomic resolution images of electrically conductive and relatively flat surfaces. The working principle of STM (Fig.2.2) is based on the concept of quantum tunnelling that play an important role to reveal the surface structure of a given surface. When a finely sharpened metallic tip is brought very close (a few atomic

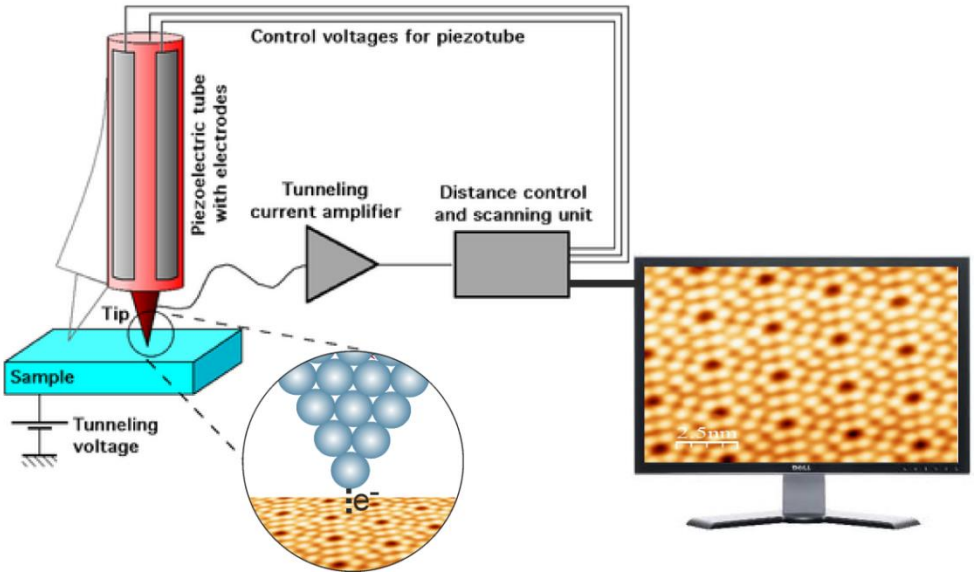

Fig. 2.2 An illustration of a scanning tunnelling microscope (STM). Image on the display screen is an atomic resolution of the Si (111)-7×7 reconstructed surface, obtained on the JSTM 4500S (Micheal Schmid, TU Wien http://www.iap.tuwien.ac.at/www/surface/stm_gallery/stm_schematic).

distances) to a conducting surface, an applied bias voltage between the tip and the surface allows electrons to tunnel through the vacuum barrier, hence, give rise to the tunnelling current. Once a tunnelling current is established between the tip and sample, an atomic resolution STM image can be obtained by scanning the tip across the sample surface. The tip is mechanically connected to a piezoelectric scanner, which precisely scans the tip over the sample surface in all three x, y, z directions to create a topographic map of the surface.

STM reveals both the topographic and electronic information of the surface under investigation with the help of an applied bias between the sample and tip that determines the direction of electron tunnelling. Fig.2.3 depicts the schematic of energy-band diagram illustrating the tip-sample interaction in various conditions [62]. When the separation between the tip and sample is of the order of macroscopic vacuum gap, regarded as insulator, they are independent of one another. This is shown in Fig.2.3a, where the Fermi levels of the tip and sample are at different energies and their wave functions are not close enough to overlap. It means there is no chance for the tunnelling

current to establish between the sample and tip at such separation. However, when the tip and specimen to be examined by the STM are close enough that the separation between them is of the order of few nanometres then their wave functions overlap. This is shown in Fig.2.3b, where the Fermi levels of the tip and sample are at the same energy level when the applied bias is zero. If a small and positive bias V is applied to the sample at such separation, the Fermi level of the sample effectively moves down by eV relative to that of the tip (Fig.2.3c). Electrons are now able to tunnel from the filled tip states into the empty states of the sample as indicated by the blue region of the band structure in Fig.2.3c. Similarly, the Fermi level of the sample moves up by eV relative to that of the tip when a negative bias V is applied to the sample. This is shown in Fig.2.3d, where electrons tunnel from the filled states of the sample to the tip.

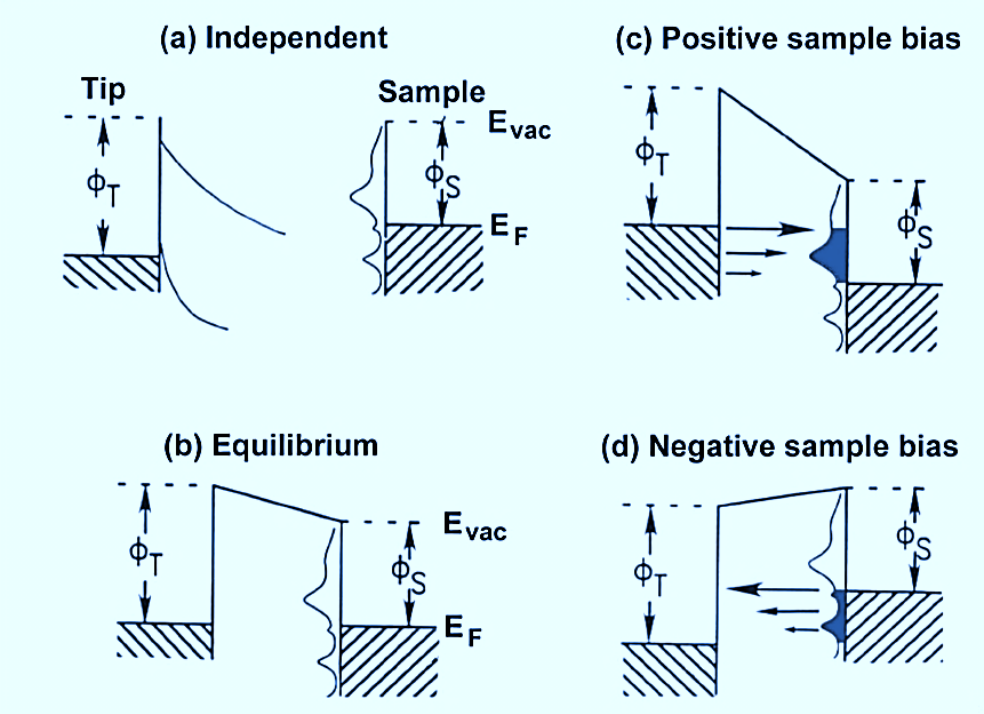

Fig. 2.3 Band diagrams showing the interaction of the sample and tip under various conditions. (a) Fermi levels of the tip and sample when they are separated by a large vacuum gap. (b) An illustration of the Fermi levels when the tip and sample are brought in contact with each other in zero applied bias. (c) The case when a positive bias is applied to the sample that raises the tip available states with respect to sample states. (d) Fermi level of the sample is raised with respect to the tip when a negative bias is applied to the sample. The figure is taken from [62].

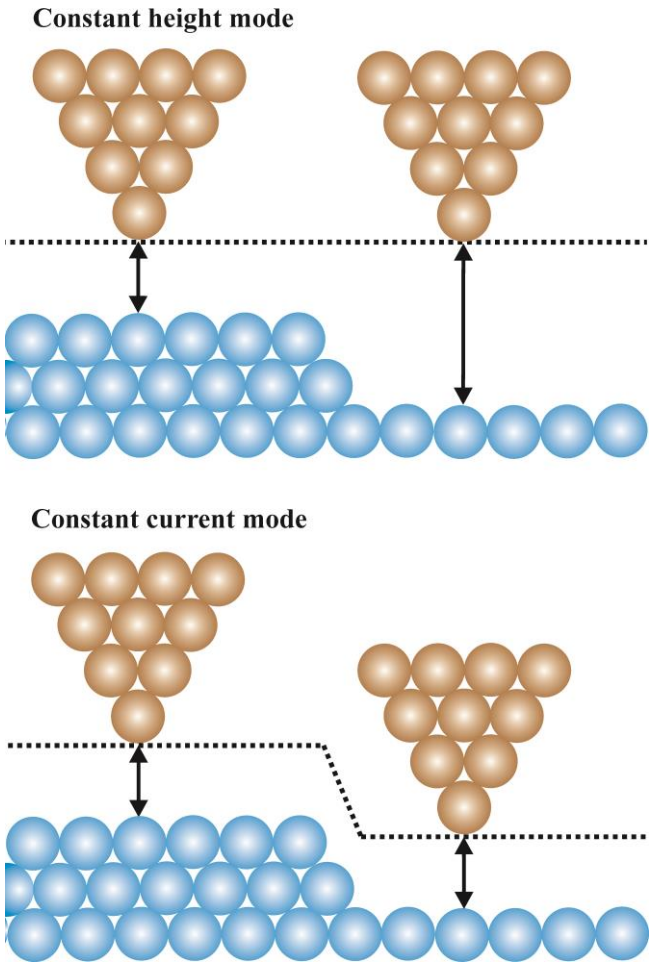

Fig. 2.4 A schematic showing the two operating modes of STM.

The magnitude of tunnelling current is highly sensitive to the tip-sample separation and decreases exponentially as the separation increases [62]. The vertical resolution of STM arises due to this exponential relationship. This means that electrons tunnel out through a leading atom on the tip into the closest atoms on the surface. The relationship can be described according to the following equation, where tunnelling current is a function of an applied bias V, work function φ, tip sample separation d, local density of states of the sample and tip ρ_s and ρ_t, respectively [62]:

$$I_t \propto V\phi^2\rho_s\rho_t\exp(-kd)$$

Where k is a constant.

In order to create a surface topography map, two modes are mainly used. One is the constant current mode and the other constant height mode as illustrated in the Fig.2.4. In constant height mode, the height of the tip, z-parameter, is kept constant at a certain distance from the sample whereas the tip is raster scanned over the surface and the tunnelling current is monitored as a function of x and y. The image obtained in constant height mode represents variation in the recorded tunnelling current. The constant height mode, however, can be used to image very smooth surfaces. The most commonly employed mode is the constant current mode. In this operating mode, a topographic STM image can be obtained when the tunnelling current is kept constant at each x and y position while the tip height is adjusted by the computer.

2.2.2 Molecular vapour deposition (MVD)

Molecular vapour deposition (MVD) is a key technique used in this thesis to investigate the reactivity of reconstructed surfaces by depositing fullerene molecules. The main advantage of MVD is to deposit the molecules at constant evaporation rates and free of any contamination. MVD works by heating the crucible to evaporate the material toward the sample placed on the stage of STM chamber [55, 58]. A Createc^{TM} Knudsen cell [63] comprises a heating element, shields and a crucible that are mounted on the STM chamber. The crucible is a closed rectangular container made of boron nitride with a small opening at one end, aligned in the direction of the STM stage when mounted in the Knudsen cell. A movable thin sheet of metal covers the small opening that can be used at the time of deposition to allow and stop the deposition of molecules. A digital temperature controller is then used to heat the coil surrounding the crucible to a desired temperature. Temperature of the crucible is accurately controlled with the help of a thermocouple and a water cooling system is used to maintain a constant temperature by preventing excessively fast heating. This is done by pumping water through pipes that fills the water jacket surrounding the K-cell.

In order to fill the crucible with molecules, the K-cell can be removed from the STM chamber by venting the system and exposing it to atmospheric pressure. The crucible is carefully removed from the K-cell by using tweezers to avoid any damage and then cleaned with acetone and methanol using an ultrasonic bath. The crucible is then heated in a tube furnace to temperature around 800 °C for half an hour to remove any remnants of molecules left from previous experiments. Since any material used for MVD will have evaporation below the annealing temperature, the crucible become clean upon heating. Once cooled, crucible can be filled in with molecules (fullerenes are used in this thesis) and placed into the K-cell. The K-cell is then re-assembled and attached to the STM chamber. The machine is then baked out for two or more days to re-establish the vacuum. During the bake-out process the system temperature is about 200 °C that helps to partially clean the K-cells. Before starting the experiments, it is important that the K-cells are well cleaned and free of any contamination present in the crucible. Any sample in the STM chamber is removed to avoid chances of contamination and water pipes are connected to the K-cell. Water is allowed to run through the K-cell to provide cooling to the system while heating it to temperatures around 30 degrees below the evaporation temperature of the molecules. Pressure in the STM is maintained below 10^{-6} Pa while slowly heating the K-cell. This whole normally takes up to three weeks to fully degas the K-Cell. After this, a sample can be introduced into the STM chamber to perform the deposition for a desired period.

2.2.3 Electron spin resonance spectroscopy (ESR)

Electron spin resonance spectroscopy (ESR), also known as electron paramagnetic resonance (EPR), has been used in this thesis to investigate the paramagnetic defects in $SrTiO_3$ single crystals. Since its invention by the Russian physicist Zavoisky [64], ESR has evolved into one of the most widely used technique to study the properties of paramagnetic materials [65-67]. The principle of ESR

spectroscopy can be explained by considering the interaction of an unpaired electron system with an external applied magnetic field **B**. The spin angular momentum, **S**, of the electron give rise to a magnetic moment

$$\boldsymbol{\mu} = -g\mu_B \boldsymbol{S}$$

where g is called the g-factor or g-value with value ≈ 2.00232 for a free electron, μ_B denotes the Bohr magneton with value equal to 9.274×10^{-24} J.T^{-1}. In general form, the magnetic moment of a paramagnetic system can be written as:

$$\boldsymbol{M} = \sum_{i=1}^{N} \boldsymbol{\mu}_i = -\sum_{i=1}^{N} g\mu_B \boldsymbol{S}_i$$

Here, $\boldsymbol{\mu_i}$ represents the magnetic moment and $\boldsymbol{S_i}$ corresponds to the spin angular momentum of the i^{th} electron. The spin angular momentum **S** can be described by its eigenvalue, spin quantum number m_s, that can take two values either (+1/2) or (-1/2). The two spin states will have same energy in the absence of an external field. However, when an external magnetic field **B** is applied along an arbitrary direction z, the degeneracy of the spin energy levels is lifted (Fig.2.5). This splitting of energy levels in the presence of magnetic field is known as *Zeeman effect* [68]. The energy difference between the two levels is then given by the equation,

$$\Delta E = h\nu = g\mu_B B$$

This basically means that electron will have a lower energy state when its magnetic moment is aligned in the direction of applied magnetic field, and a high energy state if the alignment is antiparallel relative to magnetic field. Resonance absorption occurs when the magnetic field tunes the two spin states such that their energy difference equals to that of radiation energy. At resonant condition, energy is absorbed from the microwave radiation and power reaching the detector is reduced. For a given system,

absorption can occur when the number of spins located in the lower level is greater than that in the upper level [66]. At equilibrium, the ratio of the populations of two levels is then given by the Boltzmann distribution:

$$\frac{N_2}{N_1} = \exp(-\frac{\Delta E}{k_B T})$$

where N_1 and N_2 denote the number of spins in the lower and upper level, respectively. This implies that the sensitivity or net absorption ($\propto N_1$-N_2) can be enhanced with increasing the energy difference i.e. ΔE or in other words, the microwave frequency [67]. The sensitivity of a conventional 'X band' spectrometer, operating at a frequency ≈ 9 GHz, is approximately 8×10^9 spin/G√Hz [69] which has been found to be suitable for the investigation of many paramagnetic materials.

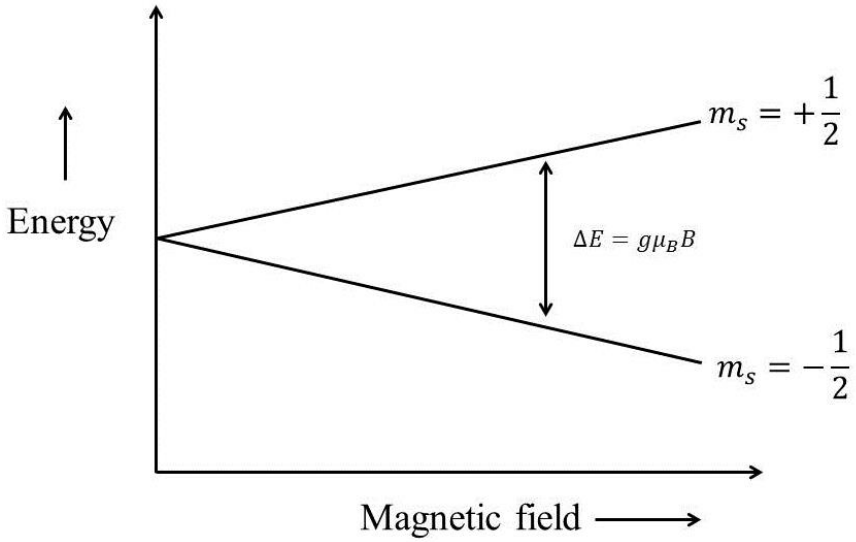

Fig. 2.5 A schematic representation of the Zeeman effect.

The ESR experiments reported in this thesis were carried out using the X-band spectrometer [70] (Bruker EMX) at the CAESR lab, Department of Chemistry, Oxford University. The spectrometer operates at frequency ≈10 GHz, and is facilitated with a continuous liquid helium flow cryostat (ESR 900). It can be cooled by a continuous flow of liquid helium to perform the temperature dependent measurements from room

temperature down to 5K. Liquid helium is supplied to the cryostat from a Dewar through an insulated transfer arm. The temperature is accurately monitored with the help of a thermocouple that is fixed very close to the sample. A temperature controller, Oxford instruments ITC temperature controller, is used to maintain good control of the temperature with high accuracy. Angular dependent measurements were performed with the help of a goniometer to rotate the sample relative to the magnetic field. Illumination effects of the specimens were studied by using a Xenon Arc lamp.

2.2.4 Cathodoluminescence spectroscopy (CL)

Cathodoluminescence (CL) is an electro-optical phenomenon commonly employed to study the luminescence properties of solid materials [71-73]. When the surface of a material is impinged with a stream of photons or high energy electrons, electrons are promoted from the valence band into the conduction band, leaving holes behind in the valence band. After a short time, the excited electrons recombine with holes in the conduction band which results in the emission of light. This phenomenon is called the *luminescence* [71]. CL arises due to a beam of electrons which is produced in the SEM. The energetic beam of electrons in the SEM, when interacting with the specimen surface, produces a variety of signals such as secondary electrons (SE), characteristic X-rays, back scattered electrons (BSE), Auger-process electrons (AES). Most of the energy is absorbed to produce the phonons that ultimately appear as heat. A little of the energy carried in the electron beam is used to excite electrons from the ground state to an excited state. When these promoted electrons lose energy and attempt to return to the ground state, they may be temporarily trapped within the band gap by extrinsic (impurity) or intrinsic (structural) defects. When electrons vacate traps, referred to as luminescence centres, and return to the ground state they lose energy in the form of photons.

The CL measurements, presented in this thesis, were carried out at room temperature with a JEOL JSM 6500F scanning electron microscope. The system is equipped with a CL detector that allows the emitted photons to be detected. The experiments were performed by mounting all the samples on a specimen holder to realize measurements under the same conditions. A 12.5 mm specimen holder was specially modified to mount all the samples.

2.2.5 Electrical transport measurements

Electrical resistivity measurements were carried out on the reduced single crystals by using physical property measurement system (PPMS), manufactured by Quantum design. PPMS is a variable temperature-field system that allows automated measurements for physical properties such as resistivity [74], I-V characteristics, Hall effect, magnetization, magnetoresistance (MR) [75], heat capacity [76] etc. The system is a cryogenic platform that allows well controlled measurements in the temperature range 4-375 K with high accuracy in variable field range (±9 Tesla).

For the electrical resistivity measurements reported in this thesis, the standard DC four-point-probe method was adopted in the temperature range 5–300 K. Four inline gold (Au)/titanium (Ti) contacts separated by 0.5 mm gap were evaporated on the sample surface. A 5 nm thick Ti layer was used for better adhesion of Au layer on sample surface. Thickness of Au layer was around 100 nm. For measurements, a constant current (I) was sourced through the outer two contacts while voltage drop (V) was measured in the inner two. The resistivity (ρ) is then computed using the expression:

$$\rho = C\frac{V}{I}$$

where C is a geometrical factor that is determined by the sample geometry and spacing between the electrodes [77]. A schematic representation of the four-point-probe method on a $SrTiO_3$ single crystal with dimensions 7 × 2 × 0.5 mm^3 is given in Fig. 2.6.

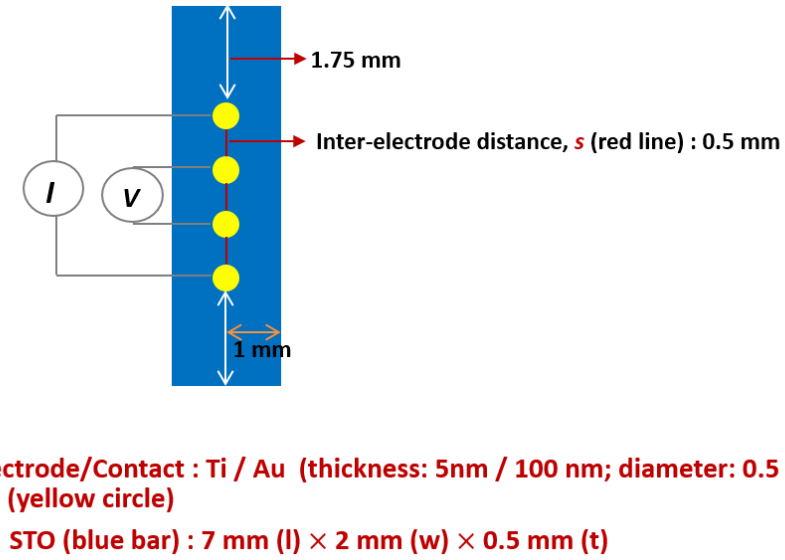

Fig. 2.6 Schematic of the contact geometry used for the electrical resistivity measurements of $SrTiO_3$ single crystals.

2.3 Methods and procedures

2.3.1 Sample treatment

The $SrTiO_3$ single crystals used for the experimental work were supplied by PI-KEM UK, with (111) and (001) surface orientation. The (111) oriented samples were doped with Nb (0.5 % weight) to facilitate the STM investigations. Dimensions of the specimens were 7×2×0.5 mm^3. These samples were carefully mounted on the sample holder, JEOL manufactured, using UHV tools (screwdrivers, tweezers etc.). UHV tools were cleaned with acetone and then methanol in an ultrasonic bath to avoid any chances of contamination. The specimen was placed on the molybdenum (Mo) posts of sample holder and then the tantalum (Ta) clips were tightened to keep it in place. The sample holder was then attached to the transfer arm of the load lock of the STM system. The load lock was then closed and the TMP was turned on to create a vacuum. The

specimen holder was then transferred into the treatment chamber by opening the valve between the load lock and the treatment chamber.

2.3.2 Annealing

Once the sample holder is introduced into the treatment chamber and UHV conditions are ensured, the sample can be heated to a desired temperature. However, it is important to degas the sample to remove any contamination present on the sample/ sample holder prior to high temperature annealing. This is accomplished by resistively passing a current through the sample. At the initial stages, pressure in the chamber rises due to outgassing of the sample and sample holder. Therefore, the voltage across the sample is gradually increased while pressure in the chamber is maintained below 5×10^{-7} Pa. The sample temperature (around 700 °C) is maintained for a few hours until pressure in the chamber eventually drops back to low 10^{-7} Pa. The sample is then slowly cooled down to room temperature or heated to a desired temperature by increasing the applied voltage across the sample. Once the desired temperature is reached, the sample can be left for the required period to anneal.

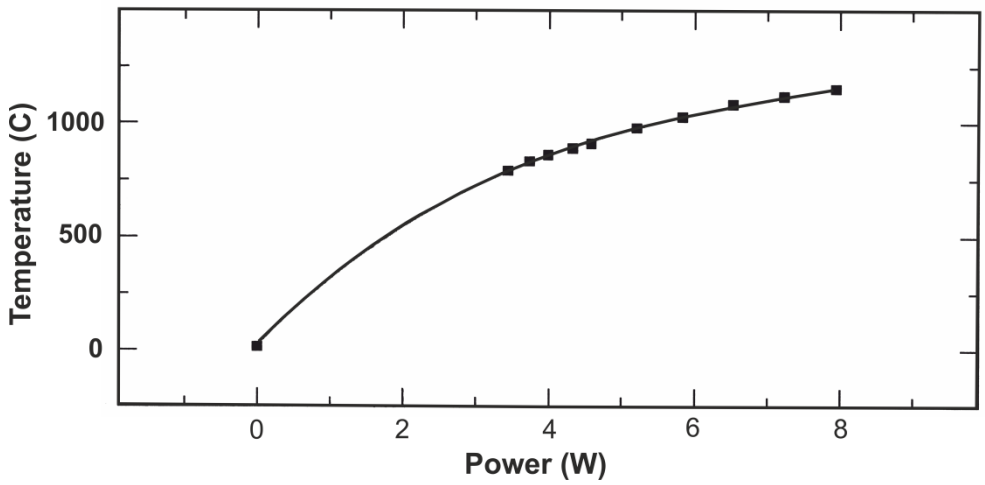

Fig. 2.7 Graph showing a calibration curve of sample temperature versus the power applied to the sample. The figure is adapted from reference [54].

Temperature of the sample is monitored with the help of Leeds and Nothrup disappearing filament optical pyrometer. However, the pyrometer is only capable to measure the temperature of a specimen that emits energy or radiations in the visible range of the optical spectrum. This corresponds to a minimum of around 750 °C. Therefore, to monitor the temperature below 750 °C a calibration curve has been plotted as shown in Fig. 2.7, where the sample temperature is plotted against the power output of the power supply [54]. The polynomial best fit equation $1.4739x^3 - 34.546x^2 + 325.3x + 15.58$ is used to estimate the sample temperatures below the pyrometer minimum [54].

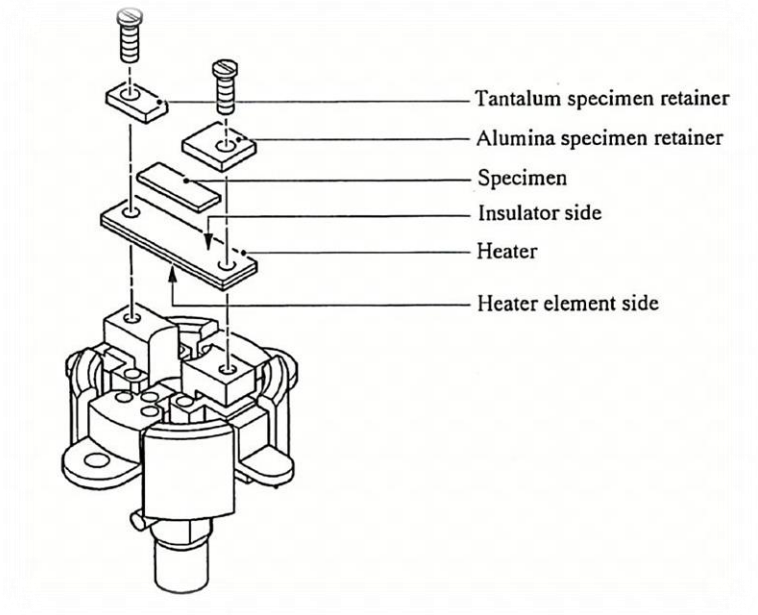

Fig. 2.8 JEOL designed indirect sample heating holder. The picture is adapted from the JEOL instruction manual [78]. The conductive side of the indirect heater is placed on the Mo posts that allow a direct current to pass through. The sample is tightened on the insulating side of the direct heater with the help of tantalum clips.

Annealing of the undoped samples was accomplished in the JSPM-4500S UHV system. Since the undoped samples are insulating and is not possible to heat them resistively by passing a current through them. Therefore, a resistive heating plate had to be used in direct contact with the sample. JEOL supplies the ceramic heaters that are designed to fit the STM sample holder [78]. Dimensions of the heater are $4\times14\times1$ mm^3.

It allows a current of up to 3A and a temperature around 1000 °C can be reached. A significant amount of gas is produced when a new heater is used for annealing. Therefore, the indirect heating holder is first introduced into the specimen chamber and outgassed for several hours. This is done without a specimen to avoid any contamination. The sample is then placed on the heater and the tantalum clips are tightened to hold both the sample and heater in place (Fig.2.8). Like other conductive samples, the sample is first degassed by passing a direct current through the heating plate and the voltage across the heater is further increased to anneal the sample.

2.3.3 Sputtering

Once a specimen is degassed, the sample surface can be sputtered off to introduce non-stoichiometry in the surface region. The sputtering process usually serves as a route for producing specific surface structures. In addition to this, sputtering can also be used to clean off the deposited materials from a sample surface and reuse the sample for further experiments. Sputtering can be achieved by the ion bombardment by noble gas ions, usually Argon (Ar). In order to produce an ion beam, Ar^+ gas is introduced in to the chamber through a leak valve and ionized by the filament of ion gun. Once plasma is created, a stream of ionized particles is then accelerated towards the sample surface by applying beam energy (typically, 0.5-5 keV). The sample is kept at ground potential to prevent charge built-up during ion impingement on the target surface. Sputtering of $SrTiO_3$ samples is performed with the aid of ISIS3000 ion source attached to the JEOL-4500XT. The ion gun operates at an Ar gas pressure of around 2×10^{-3} Pa [55]. During sputtering, pressure in the treatment chamber is controlled with the help of the TMP and the ion pump is switched off during this process to avoid saturation. After the sputtering, the specimens are annealed to remove the adsorbed contaminants, as well as restore the surface crystallography.

2.4 Summary

This chapter has introduced the experimental techniques and methods employed throughout this thesis. The techniques are used to probe the structural, optical and electronic properties of $SrTiO_3$ single crystals. The surface science techniques applicable to this thesis and UHV system in which they are housed are described in detail. The essential experimental procedures for the preparation or treatment of the sample are outlined and discussed. This involves degassing, sputtering and annealing. MVD is used to deposit different fullerene molecules to probe the reactivity of the reconstructed surfaces. ESR is used to investigate the paramagnetic species either introduced by UHV annealing or intrinsically present in the $SrTiO_3$ system. Four point probe method and CL are used as complementary techniques to probe the electrical and optical properties of the undoped and UHV annealed $SrTiO_3$ single crystals.

Chapter 3

Literature review

This chapter provides an overview of the previous research work carried out on the $SrTiO_3$ with emphasis on the link between non-stoichiometry/defects and various properties including surface structures, optical and electrical characteristics. Self-assembly of fullerene molecules is also reviewed on various semiconductor surfaces in the context of surface reactivity investigations. Based on this knowledge, a relationship between the structural and physical properties of $SrTiO_3$ is anticipated for future developments toward the engineering of potentially useful electronic devices.

3.1 The $SrTiO_3$(111) surface

3.1.1 Background

$SrTiO_3$ represents the simplest form of the perovskite structure and one of the most widely studied materials due to a variety of interesting bulk and surface properties. The (111) surface of $SrTiO_3$ is polar [79]. The crystal viewed in the [111] direction can be considered as a stack of alternating layers of Ti^{4+} and SrO_3^{4-}, both of which are not charge neutral. Here, the superscript defines the charge on each layer, while the subscript describes the number of atoms in a bulk unit cell. The Ti^{4+} and SrO_3^{4-} terminating planes are illustrated in Fig. 3.1. The separation between two

adjacent planes (Ti^{4+} and SrO_3^{4-}) has a magnitude of 0.113 nm. The bulk truncation of the structure with either a Ti^{4+} or a SrO_3^{4-} plane would lead to a large macroscopic dipole moment and hence an infinite surface energy. In order to render the $SrTiO_3(111)$ surface thermodynamically stable, the macroscopic dipole moment must be cancelled. This may occur via various routes such as changing the surface stoichiometry, modification of the surface electronic charge, adsorption of suitably charged adatoms from the residual atmosphere, or faceting [80]. The following section provides a review of the surface properties of $SrTiO_3(111)$ single crystals.

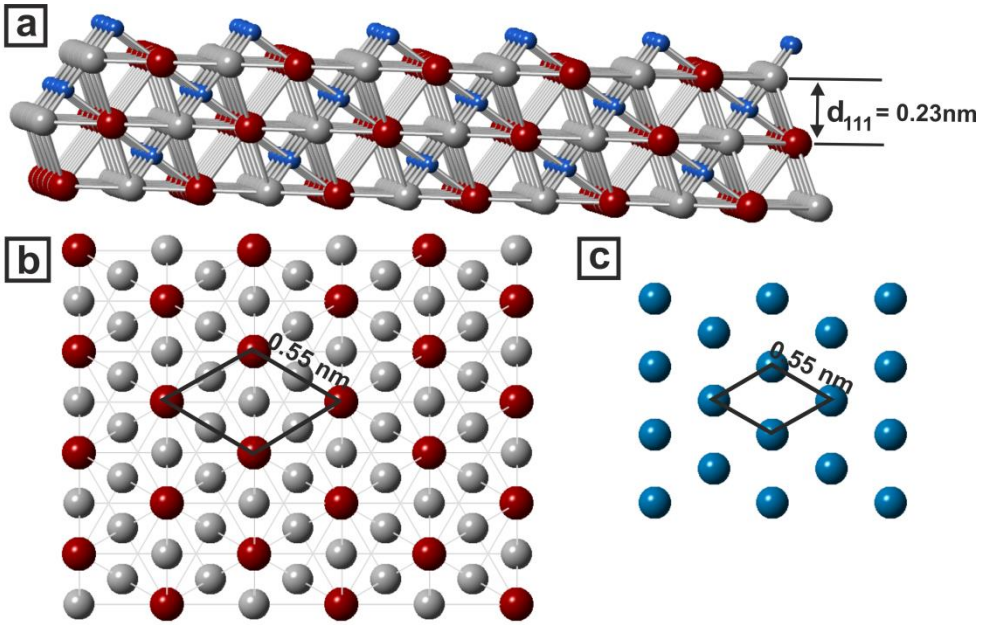

Fig. 3.1 (a) A representative model of the $SrTiO_3(111)$ surface showing a side view of the SrO_3^{4-} and Ti^{4+} alternating layers. The red, grey and blue spheres represent Sr, O and Ti ions, respectively. (b) Top view of SrO_3^{4-} and (c) top view of Ti^{4+} layers, with a unit cell indicated.

3.1.2 Early experiments on the $SrTiO_3(111)$ surface

The first investigations on the surface structure of $SrTiO_3(111)$ were carried out by Lo and Somorjai [81] in 1978. Using low energy electron diffraction (LEED), Auger electron spectroscopy (AES), electron energy loss spectroscopy (EELS) and ultraviolet photoelectron spectroscopy (UPS) they studied the effect of Ar^+ ion sputtering and annealing on $SrTiO_3(111)$. Ar^+ sputtering was performed both at room

and high temperature (600 °C). Following sputtering the sample at 600 °C, AES analysis suggested a stable Sr-rich phase on the surface and further annealing showed no effect on the surface composition. The generated LEED patterns from the sample had no clear spots that indicated faceting of the surface. Furthermore, the UPS and EELS data on the high temperature sputtered sample showed no evidence of Ti^{3+} species. However, the surfaces that were sputtered at room temperature showed a different behaviour from the high temperature sputtered samples. It was found that sputtering the sample at room temperature and then annealing at 600 °C produced a Sr-deficient surface. The AES measurements suggested that the chemical composition of the sample surface is sensitive to annealing temperature and can be varied reversibly. In addition, the UPS and EELS measurements indicated a temperature dependence of Ti^{3+} concentration. The concentration of Ti^{3+} species decreased with increasing the annealing temperature, and disappeared when the sample was heated above 600 °C. In contrast to the case of TiO_2 surfaces [82] where Ti^{3+} species were detected upon cooling the sample to room temperature, indicating an inverse relationship to the temperature.

Tanaka and Kawai [83] utilized reflection high energy electron diffraction (RHEED) and STM to investigate the surface structure after annealing $SrTiO_3(111)$ crystals at temperatures between 1180 and 1220 °C in UHV. Annealing the sample at 1180 °C for 1 min produced a surface with periodicity of $(\sqrt{6}/2)a$, where a = 0.39 nm is the lattice constant of $SrTiO_3$. When the annealing temperature was raised to 1200 °C, a new structure with periodicity of $(2/3)(\sqrt{6}/2)a$ coexisting with $(\sqrt{6}/2)a$ emerged. However, this structure disappeared when the temperature was further increased to 1220 °C, and only the $(\sqrt{6}/2)a$ structure was observed. Based on step height measurements, the surface annealed at 1220 °C was assigned to a Ti termination, whereas the 1180 °C annealed structure was assigned to SrO_{3-x} dominated surface. In a later study by Sigmund *et al.* [84], atomically flat terraces were observed for samples

annealed at 950 °C for 2 hours in UHV. Their AES analysis suggested that the surface is Ti terminated. Haruyama *et al.* [85] characterized the electronic and geometrical structure of the reduced $SrTiO_3$(111) surface. LEED patterns generated from a sample annealed at 800 °C for one hour in UHV showed a (1×1) periodicity, whereas annealing at 1200 °C for 5 min in UHV produced patterns of the 4×4 reconstruction. The surface covered with a 4×4 reconstruction exhibited weak metallic behaviour as compared to the (1×1) structure. This was attributed to the modification of the surface structure at higher annealing temperatures.

Sekiguchi *et al.* [86, 87] used AFM to investigate the effect of annealing environment on the surface morphology of $SrTiO_3$(111). Annealing the sample at 1000 °C for 10 hours in oxygen atmosphere (O_2) produced 'trench' structures, where triangular dents were initially formed after one hour of annealing and then aggregated until their sides aligned along a straight line. RHEED experiments suggested that the 'trench' structure exhibits a (1×1) periodicity. For samples annealed in the presence of Ar gas at 1000 °C for 10 hours, wide triangular terraces were observed with a (1×1) structure. However, these terraces appeared to be flatter than those observed for samples annealed in O_2. In the case of annealing in air (an intermediate oxygen partial pressure) at 1000 °C, AFM images revealed a complex morphology containing triangular facets with different sizes, resembling a fractal shape called Sierpinski's gasket. Based on the observed morphology, Sekiguchi *et al*. speculated that two kinds of nucleation occurred on the air annealed surface.

3.1.3 STM investigations of unsputtered $SrTiO_3$(111) surfaces

STM experiments by Russell and Castell [88] captured the first real space images of the (√7×√7)R19.1° and (√13×√13)R13.9° coexisting reconstructions (Fig. 3.2). The reconstructed surfaces were prepared by annealing a $SrTiO_3$(111) single crystal in UHV

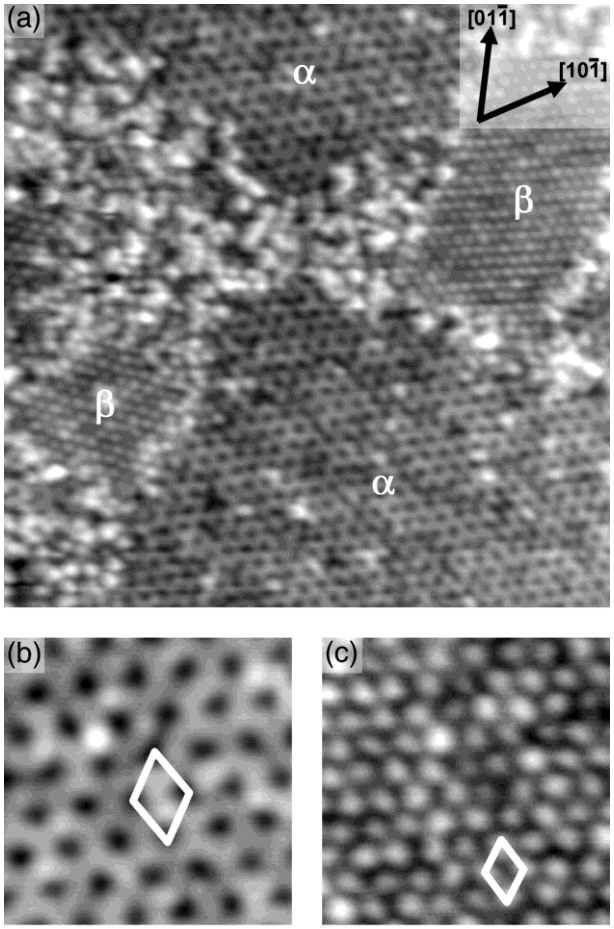

Fig. 3.2 (a) An STM image of the $SrTiO_3$(111) surface following annealing at 850 °C in UHV. The surface is made up of (√13×√13)R13.9° (labelled as 'α') and (√7×√7)R19.1° reconstruction (labelled as β) (image size = 65×65 nm^2, V_s = 2.9 V, I_t = 0.3 nA). The 'β' regions (the left and right of the image) are rotational domains of each other, whereas rotational domains of the 'α' regions were also observed. (b) A magnified STM image of the (√13×√13)R13.9° reconstruction (image size = 12×12 nm^2, V_s = 3.6 V, I_t = 0.12 nA). (c) An STM images of the (√7×√7)R19.1° reconstruction (image size = 12×12 nm^2, V_s = 2.14 V, I_t = 0.1 nA). The figure is adapted from reference [88].

at 850 °C for 30 minutes. The step heights had a measured value of 0.21 ± 0.02 nm, corresponding to the d_{111} lattice parameter. The boundaries between the ordered domains were covered with disordered regions. In Fig. 3.2a, two ordered domains are labelled as 'α' and 'β' that represent the (√13×√13)R13.9° and (√7×√7)R19.1° reconstruction, respectively. These co-existing reconstructions were further investigated through LEED experiments that showed the presence of both (√7×√7)R19.1° and (√13×√13)R13.9° surfaces. To determine the chemistry of these reconstructed surfaces, Russell and Castell performed AES measurements and compared the spectrum to that

of a cleaved $SrTiO_3$ crystal. By comparing the normalized peaks, the reconstructed surface showed an enhancement in the Ti and Sr concentration and appeared to be deficient in O.

3.1.4 STM investigations of sputtered $SrTiO_3$(111) surfaces

In the above study, the effect of UHV annealing on formation of surface reconstructions on the $SrTiO_3$(111) was investigated. Argon ion sputtering is also known to affect the surface stoichiometry. In another study, Russell and Castell [29] obtained a number of reconstructions constituting a family of (n×n) periodicity, where $(9/5) \leq n \leq 6$ by varying the sputtering conditions and annealing environment. For samples that were sputtered for 10 minutes and then annealed at 950 °C for 10 minutes in UHV produced two coexisting 4×4 (labelled as 'α') and 6×6 (labelled as 'β') reconstructions (Fig. 3.3a and 3.3b). The surface morphology exhibited large terraces separated by step edges with a measured step height corresponding to the d_{111} lattice parameter. Regions of the 4×4 ('α') reconstruction showed two chiral domains. However, the reconstructed surface covered a small area due the presence of disordered regions. The 6×6 reconstruction showed pattern of bright spots that were observed to be sensitive to applied bias ('β' region in Fig. 3.3b). Samples that were sputtered for 20 minutes and then annealed at 1050 °C produced a 5×5 reconstructed surface (Fig. 3.3c). The surface morphology showed atomically flat terraces separated by step edges with step heights corresponding to the d_{111} lattice parameter. Russell and Castell further extended their studies to investigate the effect of annealing environment on the formation of surface structures. A sample that was sputtered for 10 minutes and then annealed for 5 hours at 1150 °C in 4.0×10^{-4} Pa O_2 evolved a surface with 3×3 periodicity (Fig. 3.3d). Some regions showed the coexistence of 3×3 reconstruction with the 4×4 surface.

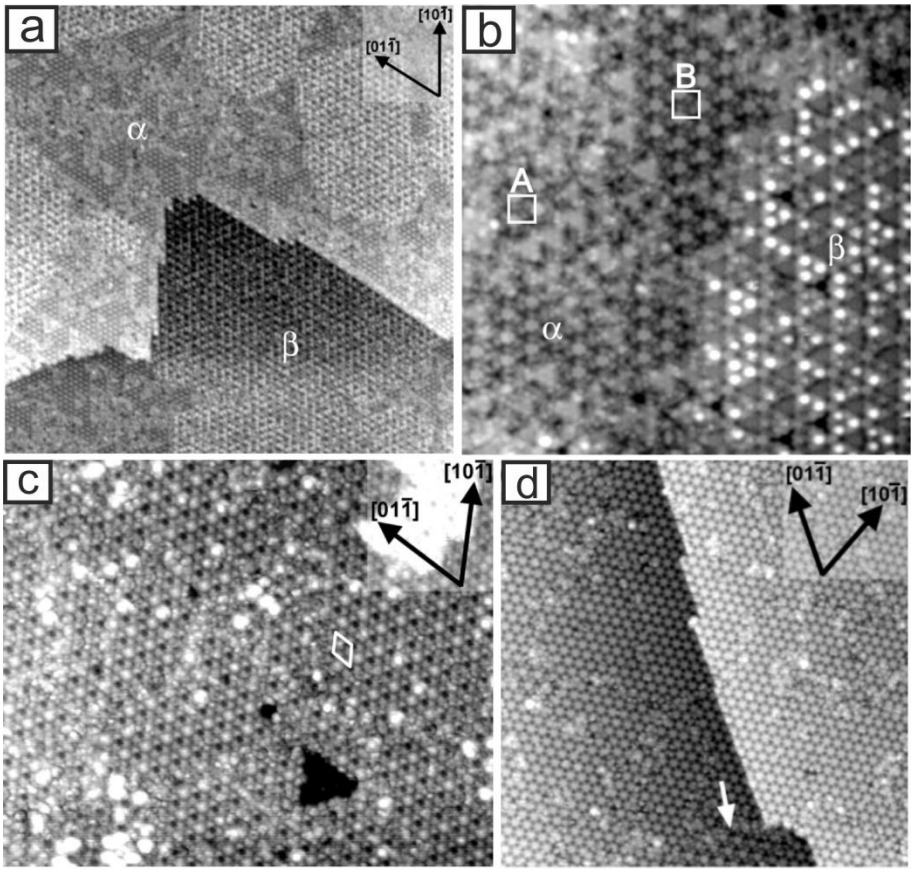

Fig. 3.3 (a) A large scale STM image showing the surface morphology of a sample sputtered for 10 minutes and then annealed at 950 °C for 30 min. The image shows large terraces composed of two ordered regions: one is 4×4 reconstruction (labelled as 'α') and the other is 6×6 reconstruction (labelled as 'β') (image size = 160×160 nm^2, V_s = 2.22 V, I_t = 0.12 nA). (b) An STM image of the 6×6 (β) and 4×4 reconstructions (α). Two domains are indicated as 'A' and 'B' in the region covered with the 4×4 (α) reconstruction, that form non-superimposable images of each other (image size = 38×38 nm^2, V_s = 2.0 V, I_t = 0.15 nA) (c) An STM image of the 5×5 reconstruction with a surface unit cell indicated. The surface was formed after sputtering the sample for 20 min. and then annealing at 1050 °C in UHV for 30 min (image size = 60×50 nm^2, V_s = 2.6 V, I_t = 0.2 nA). (d) STM image showing terraces covered with the 3×3 reconstruction, whereas a small region at the bottom (indicated by an arrow) shows a 4×4 domain (image size = 67×67 nm^2, V_s = 2.0 V, I_t = 0.4 nA). All the images are adapted from reference [29].

The above (3×3), (4×4), (5×5) and (6×6) reconstructions were obtained following Ar^+ sputtering of the samples and in-situ annealing. The effects of ex-situ annealing were also studied, where samples were first sputtered for 10 minutes and then annealed in a tube furnace at 1100 °C for 10 hours in the presence of pure air (80:20 N_2:O_2 mix). The samples were then introduced into the STM system and the surface structure was checked with STM. The images showed the formation of a (9/5×9/5) reconstruction

(Fig.3.4a). Since the periodicity of (9/5×9/5) surface is not an integer multiple of the bulk (1×1) structure, the surface formed an incommensurate phase with the underlying bulk structure. The influence of the underlying bulk layers was observed in the form of 'trenches' when the periodicity of (9/5×9/5) surface commensurate with the underlying bulk layers.

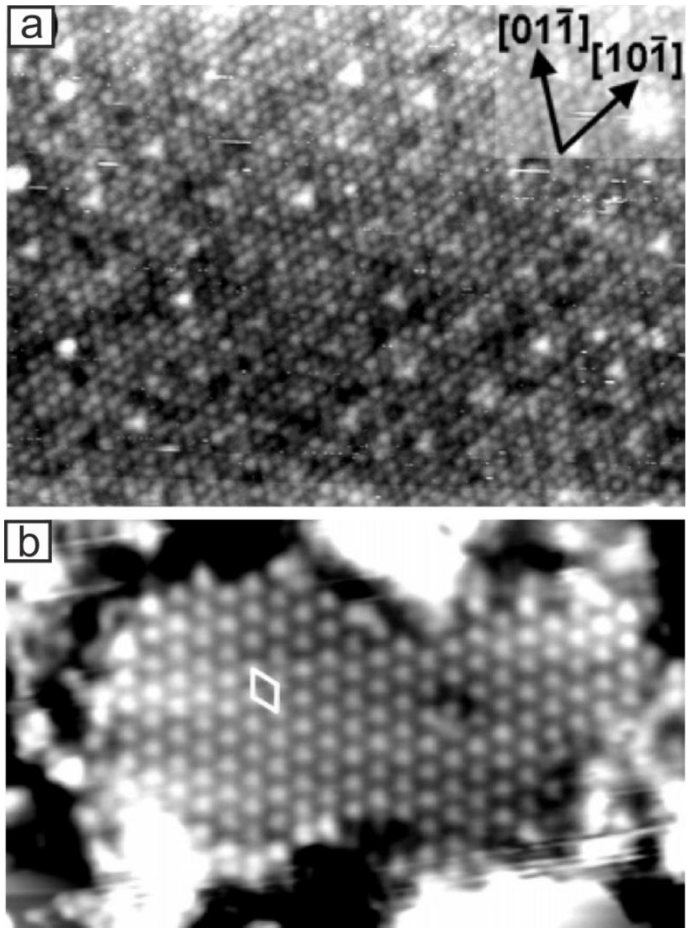

Fig. 3.4 (a) STM image showing a (9/5×9/5) domain following Ar^+ sputtering and annealing in air (80:20 N_2:O_2 mix) (image size = 42×32 nm^2, V_s = 2.0 V, I_t = 0.1 nA). (b) STM image of the TiO(111)- (2×2) nanophase. The surface was produced by heating a sputtered sample to 1400 °C in UHV (image size = 14×8.5 nm^2, V_s = -1.0 V, I_t = 0.5 nA). The images are adapted from reference [29].

When the samples were heated to temperatures above 1400 °C in UHV, the majority of the surface area was found to be very rough. However, small ordered regions with irregular shapes were found and imaged with STM (Fig.3.4b). The ordered surface was found to be conducting as it was possible to image the sample by applying negative or positive biases close to zero, which is contrary to the n-doped $SrTiO_3$ that

can only be imaged by applying a positive sample bias. Furthermore, the ordered regions exhibited a periodicity of 0.59 nm which corresponds to two times the (1×1) periodicity of the TiO(111) surface (0.30 nm). Based on the above investigations, the ordered regions were assigned as a TiO(111)- (2×2) nanophase and this was further verified by AES experiments that showed a largest Ti peak in the spectrum when compared with that of a UHV cleaved surface.

Argon ion sputtering is known to make the surface rough and introduce oxygen vacancies in the top few layers. This suggests that by increasing the sputtering time, the disorder will increase and make the surface more oxygen deficient. Based on the formation conditions, Russell and Castell ordered the family of (n×n) reconstructions from oxygen depleted to oxygen enriched as follow:

$$\text{O depleted } (5\times5) < (6\times6) < (4\times4) < (3\times3) \text{ O rich}$$

In order to further verify the relative oxygen depletion level, Russell and Castell performed AES measurements on the reconstructed surfaces and the normalized peak heights in the spectra were compared with that of a UHV cleaved surface. The concentrations of each species (Sr, O and Ti) calculated from the AES spectra are summarized in table 3.1. The TiO(111)-(2×2) was found to be the most Ti-enriched surface followed by (5×5), (6×6), (4×4) and (3×3), with the least Ti-enriched being the (9/5×9/5). Oxygen depletion level of reconstructed surfaces was determined from the O/Ti ratio. The TiO(111)-(2×2) structure appeared to be the highly reduced phase due to the lowest O/Ti ratio (0.90), whereas the most oxygen-enriched phase was represented by the (9/5×9/5) reconstruction that exhibited the highest O/Ti (2.18) among all the surfaces.

reconstruction	Ti	O	Sr	O/Ti	Ti/Sr
TiO(111)-(2 × 2)	3.23	2.91	0.15	0.90	N/A
(5 × 5)	1.98	2.78	0.88	1.40	2.26
(6 × 6)/(4 × 4)	1.74	2.73	0.72	1.56	2.43
(3 × 3)	1.63	2.74	1.05	1.68	1.56
(9/5 × 9/5)	1.26	2.74	1.02	2.18	1.24
cleaved	1.00	3.00	1.00	3.00	1.00

Table 3.1 The concentration of chemical species present on the reconstructed surfaces, measured from the AES spectra. The figure is adapted from [29].

The reconstructions on the $SrTiO_3$(111) surface observed by Russell and Castell [29] were also investigated by Chiaramonti *et al.* [89] using transmission electron microscopy (TEM). They systematically investigated the formation of surface reconstructions on $SrTiO_3$(111) as a function of annealing time ($0.5 \leq t \leq 10$ h), temperature ($850 \leq T \leq 1100$ °C), and oxygen partial pressure ($0.2 \leq pO_2 \leq 1.0$ mbar). They found surface structures with (n×n) periodicity, where n = 3, 6, and 9, that showed dependence on the combination of annealing temperature, time and annealing environment. Interestingly, they observed the reconstruction with 6×6 periodicity on a sputtered surface that was annealed in an oxygen rich environment while this periodicity was previously observed by Russell and Castell on sputtered surface after UHV annealing. However, the type of samples used in both studies could not be ignored, where 25-100 nm thick specimens were especially prepared for TEM measurements in contrast to Nb doped single crystals used by Russell and Castell. Chiaramonti *et al.* suggested that the formation of 6×6 reconstruction requires the re-oxidation of the sputtered surface which is done by annealing the sample in an oxygen rich environment. In case of UHV annealing of the few mm thick sputtered sample, the process of re-oxidation can be done by the action of self-diffusion exchange with the bulk as suggested by Chiaramonti *et al.* The driving force for this process is the concentration gradient of oxygen between the sputtered surface and the bulk of the crystal.

Several reconstructions were found to coexist under certain conditions, but the (3×3) and (9×9) reconstructions were always found to coexist with each other. Phase maps are shown in Fig. 3.5, where each annealing time (0.5 h, 5 h and 10 h) is plotted against the annealing temperature and oxygen partial pressure. A sample that was annealed for a short time (0.5 h), the surface periodicity exhibited a dependence on the oxygen partial pressure. For samples that were annealed for longer time (10 h), the periodicity of the reconstructions varied with annealing temperature. Following annealing for 5 h, the periodicity of the reconstructions was observed to be a function of both annealing temperature and atmosphere.

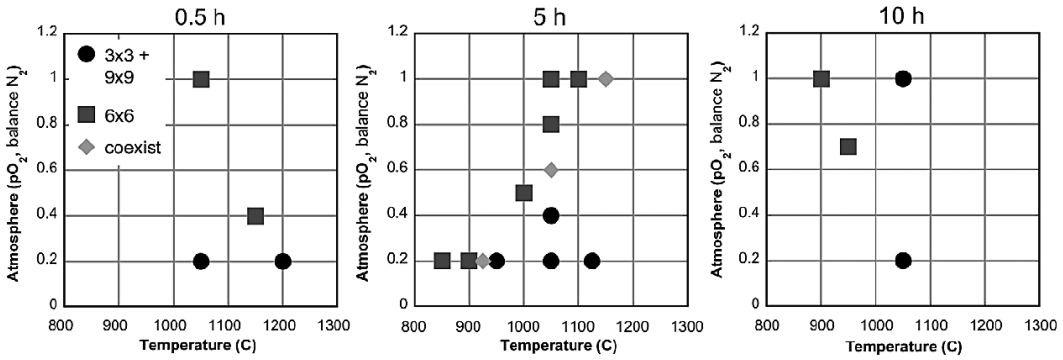

Fig. 3.5 Phase diagrams showing the formation of reconstructions on the $SrTiO_3$(111) surface as function of annealing temperature and oxygen partial pressure. The figure is adapted from reference [89].

The challenge to obtain $SrTiO_3$(111) surfaces with a certain reconstruction was further addressed by Feng *et al*. very recently [90]. The authors reported that the evolution between the 4×4, 5×5 and 6×6 reconstructions can be controlled by the deposition of Sr or Ti followed by annealing in oxygen environment (5.5×10^{-6} mbar). The surface structures were investigated with STM, LEED and RHEED. It was found that by increasing the deposition of Ti to more than 0.38ML, the 4×4 reconstruction evolves into the 6×6 surface. A monophased 6×6 domain was achieved when the Ti deposition reached 1.13 ML. Upon further increasing the Ti deposition, the surface then evolved into the 5×5 reconstruction. In contrast to the large flat terraces of 5×5 reconstruction observed by Russell and Castell, the 5×5 domain developed in the three

dimensional mode. A reverse evolution from the 5×5 to 6×6 and then to 4×4 reconstruction was observed by the deposition of Sr. Moreover, the STM measurements of the height difference between the 4×4 and 6×6 domains had a value close to 0.113 nm, whereas the 5×5 to 6×6 were measured to be of equal height. The authors claimed that the 4×4 reconstruction is based on the SrO_3 termination which is contrary to what Russell and Castell found from AES data [29], whereas the 5×5 and 6×6 reconstructions are based on Ti termination.

Although the surface chemistry and surface structures are characterized experimentally, theoretical studies on the (111) surface of $SrTiO_3$ are mainly confined to the (1×1) unit cell [91]. Pojani *et al.* [79, 92] reported the stability of the stoichiometric $SrTiO_3$(111)- (1×1) surface. They found that the (1×1) unit cell is stable under significant electronic distribution but retain its insulating nature.

3.1.5 Summary and outlook

A series of investigations that have been made to explore the structure of the $SrTiO_3$(111) surface are outlined and discussed. $SrTiO_3$(111), like other low index surfaces of $SrTiO_3$, is shown to exhibit a variety of reconstructions upon simple treatments such as Ar^+ ion sputtering and/or annealing the sample. However, the study of this surface is complicated by its polar nature and any reconstruction formed must compensate the surface charge in order to be thermodynamically stable. Moreover, many of the observed surface reconstructions have been found to coexist on a single sample under a wide range of surface treatments which make it difficult to control the evolution between them. The realization of these surfaces for potential applications requires the ability to construct a certain surface with good control. Recently, the evolution between various reconstructed surfaces has been investigated through the deposition of Ti or Sr [90]. However, achieving a monophased reconstructed surface is still a challenge. Moreover, understanding the formation mechanism of surface

reconstructions and their chemical identities is of vital importance not only to address the fundamental surface science questions but also for the development of applications in future technology. With the growing experimental research on $SrTiO_3$(111) through techniques such as STM, AES, LEED and TEM, theoretical models are required to build up a comprehensive knowledge of $SrTiO_3$ surfaces. Hence, the use of high resolution STM images in conjunction with theoretical calculations will allow the solution of the chemical identities and formation mechanisms of $SrTiO_3$ surfaces to be tackled successfully.

3.2 The interaction of fullerenes with solid surfaces

3.2.1 Background

Fullerene molecules, discovered by Kroto *et al.* in 1985 [93], are made of carbon atoms that are arranged in a closed cage configuration. The most common fullerene is the C_{60} molecule, also known as Buckminster or Bucky ball, which exhibits a shape similar to a soccer ball (as shown in Fig. 3.6a). The average cage diameter of the molecule is 0.7 nm and consists of 12 pentagonal rings and 20 hexagonal rings [93]. In the bulk phase they adopt an FCC structure with lattice parameter of 1.44 nm and intermolecular distance of 1 nm [94, 95]. At room temperature they rotate freely around their centre of mass [96]. Another common fullerene is the C_{70} molecule which resembles a rugby ball. It is structurally similar to C_{60} except that it contains additional 10 carbon atoms which elongate the molecule through the formation of 5 additional hexagons, (Fig. 3.6b). The diameter of C_{70} along the short and long side is 0.7 nm and 0.78 nm, respectively [97]. C_{70} has been found to adopt both FCC and HCP configurations, with the FCC being more stable at lower temperature and HCP at higher temperatures.

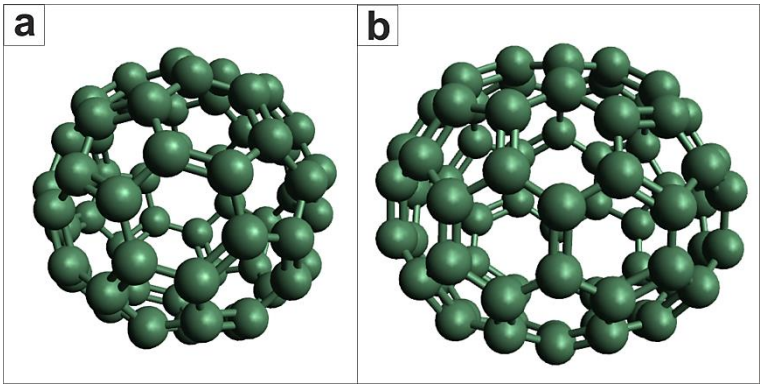

Fig. 3.6 Schematic representation of fullerenes. (a) and (b) are the ball and stick models of buckiminster C_{60} and spheroid shaped C_{70} molecule, respectively.

Fullerenes have attracted considerable interest due to their unique structure and electronic properties that make them promising materials for potential applications in various fields [98-100]. In order to further exploit their properties there is a need to arrange these molecules into particular ordered patterns, ideally supported on suitable substrates. For example, metal surfaces such as Au(111) [101-105], Au(110) [106, 107], Cu(111) [108-110], Ag(100) [111, 112], Pt(111) [113, 114], Pt(110) [115, 116] have been widely used to elucidate the self-assembly of fullerenes. On the majority of solid surfaces fullerene molecules produce a close-packed arrangement with a nearest neighbour distance close to the 1.0 nm van der Waals diameter found in bulk FCC. A few review papers have summarized the interaction of fullerenes with solid surfaces [117-120]. Due to the diversity of the subject the following section is focused only on the interaction of fullerenes with semiconductor surfaces with particular focus on the $SrTiO_3$ surfaces.

3.2.2 Fullerenes on semiconductor surfaces

3.2.2.1 The interaction of fullerenes with silicon surfaces

Silicon surfaces have been widely used to elucidate the self-assembly of C_{60} fullerenes. Early reports looked at the interaction of C_{60} with the Si(111)-7×7 reconstruction [121-123]. It was found that C_{60} randomly adsorbed on the surface with

no tendency to form close-packed islands or nucleate along the step edges (Fig. 3.7a). This behaviour of C_{60} is distinctly different from that observed on other solid surfaces where they produce close-packed structures. Li *et al.* [121] and Sakurai *et al.* [122, 123] attributed this behaviour to a strong interaction between molecules and the template that freezes the migration of molecules on the surface. Due to strong interactions between molecules and Si(111)-7×7, the free rotation of molecules is expected to be hindered due to which the intermolecular structures of fullerenes can be observed in the STM images [124-126]. Statistical analysis of STM data suggested four specific adsorption sites for C_{60} on the Si(111)-7×7 reconstruction [122, 127]. These sites are labelled as A, A', B and C in Fig. 3.7b, where A and A' are located in the middle of faulted and unfaulted halves respectively, and B, C are the corner hole and on the edges of 7×7 unit cell respectively. The faulted half (site A) appeared to be highly preferential for C_{60} adsorption. However, the precise determination of adsorption sites is complicated probably due to the large size of the molecules [125, 128, 129]. Chen *et al.* [128] proposed that the preferred adsorption sites are the adatom bridge positions within a triangular half. In a later study, they found that the preferred sites are close to three midadtoms in either triangular halves of the unit cell [129]. Moreover, the preferred sites were observed to change with increasing C_{60} coverage to ~1ML. Similarly, C_{70} molecules showed additional adsorption sites that were slightly displaced from the middle of triangular halves [130]. Huang *et al.* [124] measured the apparent height of individual molecules, adsorbed at the faulted and unfaulted halves, and claimed that molecules are "embedded" in the template surface. In another study [125, 131], the internal structure of C_{60} appeared to have distinctly different orientations on each adsorption site and altered through the attachment of Ag atoms to the adsorbed molecules. The original orientations observed for a naked surface were restored after removing the Ag atoms.

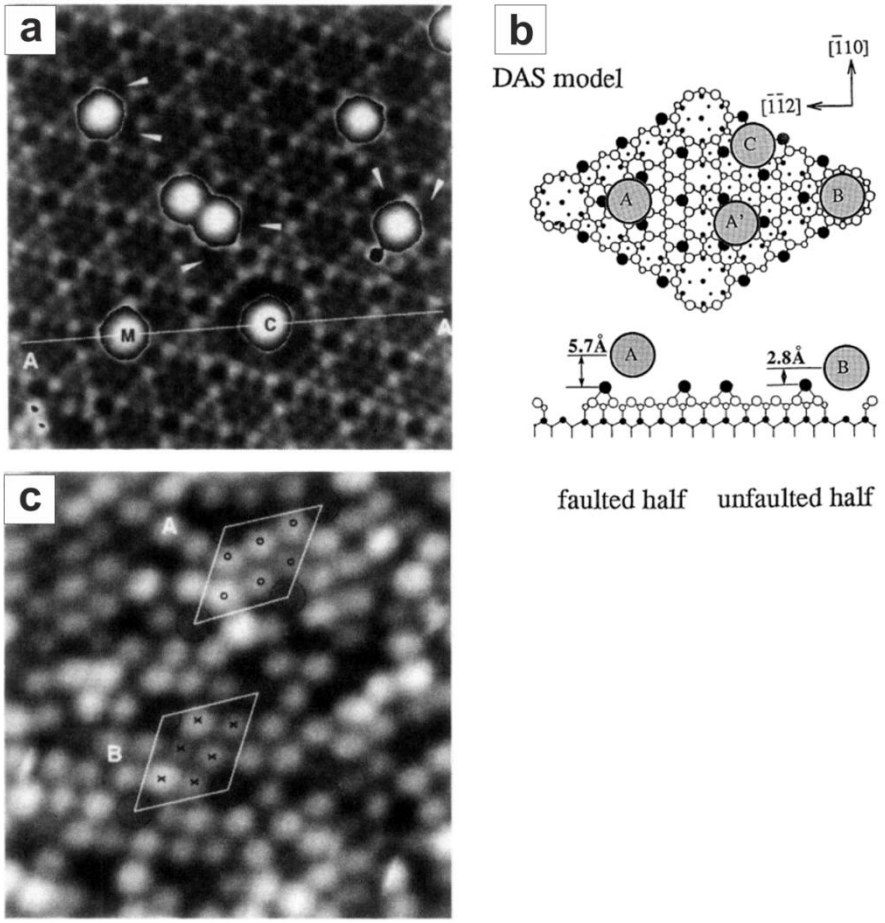

Fig. 3.7 (a) An STM image showing the adsorption of individual C_{60} on the Si(111)-7×7 reconstructed surface. (b) A schematic showing the adsorption sites of individual C_{60} on the surface. (c) STM image of the ordered phases formed at ~1ML coverage of C_{60}. The figures are adapted from [122, 129].

Chen *et al.* [129] pointed out in their study that the nature of molecules-substrate interactions changes with increasing deposition. After deposition of 1ML coverage at room temperature, an ordered arrangement of C_{60} overlayer was formed due to pinning of molecules at the corner hole 7×7 unit cell (Fig. 3.7c). These findings are in contrast with an earlier report where a transition from disordered to ordered phases has been reported to occur due to interlayer interactions in multilayer films [132]. A disordered arrangement of C_{60} has been observed in the first and second layer while the formation of ordered structures occurred after the third layer [132, 133]. Chen *et al.* [128] also studied the effects of annealing temperature on the adsorption of C_{60} molecules. They deposited C_{60} molecules at room temperature and then heated the surface to elevated

temperatures. The individual fullerenes, instead of being desorbed from the surface, remained intact up to 600 °C and decomposed at 850 °C.

The Si(100) surface has also been used to investigate the interaction of fullerenes. Early work by Sakurai's group [122, 134, 135] investigated the interaction of C_{60} on the Si(001)-2×1 reconstruction [136] at room temperature. Like on the Si(111)-7×7 reconstruction, C_{60} randomly adsorbed on the surface without producing large islands. At submonolayer coverage, the preferential bonding sites of C_{60} were identified as the middle of four neighbouring dimers (position A in Fig. 3.8b). Similar adsorption behaviour has also been observed for C_{70} molecules when a low coverage is produced on the surface [137, 138]. With further increasing the C_{60} coverage two short range ordered phases with square (top region in Fig. 3.8a) and hexagonal arrangement (lower right region in Fig. 3.8a) were observed [122, 135, 139]. In this case additional C_{60} molecules occupied the position B (Fig. 3.8b) to adopt a square configuration whereas the occupation of site B' produced the hexagonal arrangement. Both the square and hexagonal regions represented a c(4×4) and c(4×3) periodicity, respectively. The distance between neighbouring A and B sites had a measured value of 1.09 nm in regions covered with c(4×4) arrangement. Similarly, the separation between molecules at A sites had a value of 1.15nm, whereas A and B' were 0.96 nm apart in regions with c(4×3) structure. In addition, due to strong interaction between the molecules and Si(001)-2×1, the intermolecular structures of fullerenes were observed indicating the free self-rotation of C_{60} is hindered by the template surface [134, 135]. At higher coverage C_{60} produced multilayer structures with the first and second layers being disordered due to influence of the underlying substrate and adopted the FCC(111) configuration after the third layer [122, 134, 135].

Chen *et al.* proposed that the bonding character between C_{60} and Si(001)-2×1 surface changes from physisorption to chemisorption after heating the substrate to

elevated temperatures [140]. However, when a 0.04ML of C_{60} was deposited at 650 °C the underlying 2×1 reconstruction modified to form a surface phase with c(4×4) periodicity and encouraged the molecules to adsorb preferentially at the step edges and defects [141]. This indicated that the bonding configuration of molecules deposited at room temperature is different from that at higher temperatures. When the deposition temperature was further increased to 750 °C, C_{60} molecules decomposed to form islands of SiC. Similarly, C_{70} produced disordered islands at room temperature and showed well-ordered hexagonal arrangement when deposited at 250 °C [138]. At temperature above 1000 °C the reaction of C_{70} and Si surface encouraged the formation of β-SiC(100)-2×3 islands with well-ordered arrangement [137, 138].

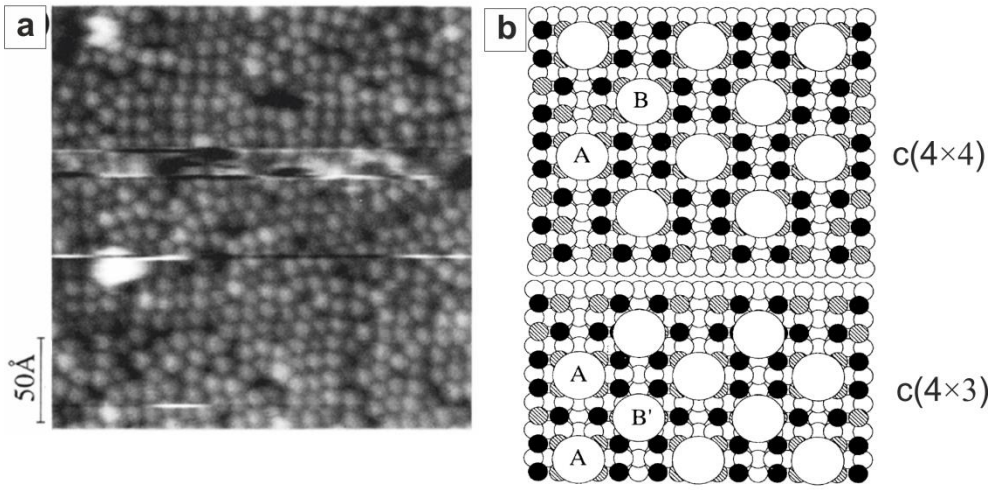

Fig. 3.8 (a) STM image of C_{60} monolayer deposited on the Si(001)-2x1 reconstruction. (b) A schematic representation showing the square configuration c(4×4) and the hexagonal arrangement c(4×3) of C_{60} fullerenes. The figures are adapted from [122, 135].

Due to strong interaction between fullerenes and clean silicon surfaces, monolayers with well-ordered arrangements were not observed. Instead the monolayers formed appeared to be disordered and only small regions of the order of a few nanometres exhibited an ordered arrangement of fullerenes. Metal-terminated silicon surfaces, however, encourage the formation of well-ordered arrangement of fullerene molecules [142, 143]. One example is the Ag-terminated Si(111)-√3×√3 surface. At submonolayer coverage (0.8ML), deposited at 200 °C, both 3√3×3√3 and √21×√21

arrangements of C_{60} were observed at room temperature [144, 145]. STM images revealed the intermolecular features of C_{60} adsorbed at the step edges, suggesting rotation is not possible at the step edges. The close-packed separation of $3\sqrt{3}\times3\sqrt{3}$ and $\sqrt{21}\times\sqrt{21}$ molecular arrays had a measured value of 0.998 nm and 1.016 nm, respectively. The variation in intermolecular separation produced dark features interpreted as "missing-molecule defects" [146]. However, a recent work reported that these dark features in the monolayer are "dim" molecules that are situated ~1.6 Å lower than the other C_{60} [147].

The template-assisted self-assembly of molecules, discussed above, involves the use of surfaces with large superstructures that have adsorption sites. The molecules aggregate through these adsorption sites into continuous islands and very rarely size-specific structures are also obtained. Very recently, Gruznev *et al.* [143] presented a new approach to self-assemble C_{60} molecules into clusters of specific sizes with unusual shapes on a gold-indium-covered Si(111) surface. Interestingly, they found the self-assembly of C_{60} molecules to be stepwise which was mediated by the moire´ interference between an island with its underlying lattice. The stepwise growth of islands is depicted in Fig. 3.9 which shows dramatic reduction in the growth rate whenever the self-assembled structure reaches a certain shape and size. Among all size-specific clusters, the hexagonal one with 37 C_{60} molecules (37-mer) exhibited enhanced stability and abundance which indicated the preference in cluster's sizes and shapes. When C_{60} molecules were deposited at 110 K on the Si(111)-$\sqrt{3}\times\sqrt{3}$ (Au, In) surface and afterwards annealed at room temperature for more than 48 hours, the majority of the clusters produced were 37-mer. Hence, this concept provides a new tactic to grow larger monodispersed mesoscopic structures with atomic precision [143].

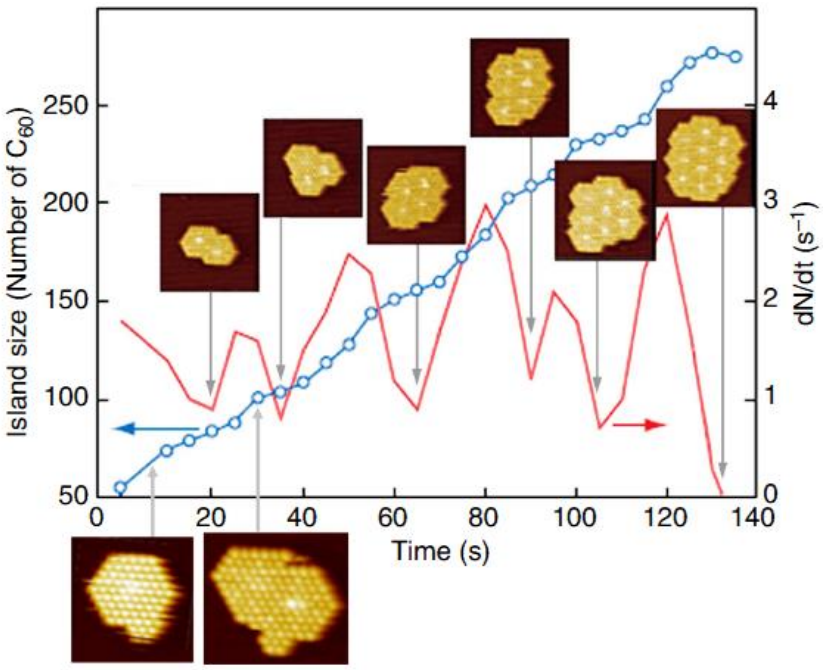

Fig. 3.9 Plot showing the stepwise growth of fullerene island as a function of deposition time (blue curve). Molecules were deposited at room temperature. The red curve is the derivative of the blue curve and corresponds to the growth rate. Adapted from reference [143].

3.2.2.2 Fullerene adsorption on germanium surfaces

The nature of interaction between fullerenes and Ge(111) surfaces is significantly different from that of Si surfaces. When 1ML of C_{60} is deposited on the Ge(111)-2×8 reconstruction at room temperature, fullerenes randomly adsorbed on the surface with only few producing close-packed structures [148]. Annealing treatment of the surface covered with a C_{60} monolayer at 250-500 °C resulted in the formation of $(3\sqrt{3}\times3\sqrt{3})R30°$ LEED patterns, and STM images revealed the formation of close-packed islands with C_{60}-C_{60} separation of 1.0 nm [148, 149]. Annealing the surface covered with $(3\sqrt{3}\times3\sqrt{3})R30°$ overlayer at a temperature above 500 °C produced a structure with $(\sqrt{13}\times\sqrt{13})R14°$ periodicity which consisted of two rotational domains. The $(\sqrt{13}\times\sqrt{13})R14°$ overlayer had a close-packed separation of 1.44 nm and remained intact up to 700 °C. When the sample temperature was further raised, fullerenes desorbed from the surface and the original 2×8 reconstruction was restored. Annealing a sample with a $(3\sqrt{3}\times3\sqrt{3})R30°$ overlayer at 500 °C for short time resulted in the

formation of 5×5 phase with hexagonal array of vacancies [148]. The 5×5 phase formed ordered arrangements in small regions that coexisted with the $(3\sqrt{3}\times3\sqrt{3})R30°$ phase. All the observed ordered phases of C_{60} appeared to have no correlation with the Ge(111)-2×8 reconstruction as the periodicities of these ordered structures are different from that of the Ge(111)-2×8 surfaces. This suggested that the surface is highly disrupted after deposition of C_{60} and the underlying Ge(111) surface is greatly modified to accommodate the C_{60} ordered structures [148].

Fullerenes have also been ordered on the Ge(001) surface [150-153]. C_{60} molecules deposited on the Ge(001)-2×1 reconstruction, with the substrate initially heated at temperature around 100 °C and then gradually reduced to 40-50 °C, produced well-ordered monolayers [151]. C_{60} adopted a c(3×4) arrangement on the template surface, similar to that observed on the Si(100)-2×1 reconstruction. With increasing C_{60} coverage, layer by layer growth is observed where the top layers are corrugated [152].

3.2.2.3 Adsorption of fullerenes on GaAs surfaces

The early studies by Li *et al.* [154, 155] reported the effect of GaAs(110)-(1×1) surfaces on the growth of fullerenes. When a submonolayer coverage (0.5 ML) of C_{60} was deposited on the surface at room temperature, highly ordered islands were observed in STM images [154] (Fig. 3.10a). The formation of a fullerene layer indicated that molecules are mobile on the surface. Li *et al.* attributed this behaviour to weak van der Waals forces. Furthermore, the intermolecular structure of fullerenes was not observed in the STM images due to self-rotation of molecules at room temperature. The C_{60} molecules appeared to occupy two different adsorption sites on the template surface. These sites are labelled as ‘A’ and ‘B’, where site ‘A’ appeared 0.08 nm lower than side ‘B’ as shown in Fig. 3.10b. The variation in apparent height difference occurred due to substrate corrugation. The C_{60} array at site ‘A’ adopted a c(4×2) arrangement relative to its underlying surface. The close-packed separation along the

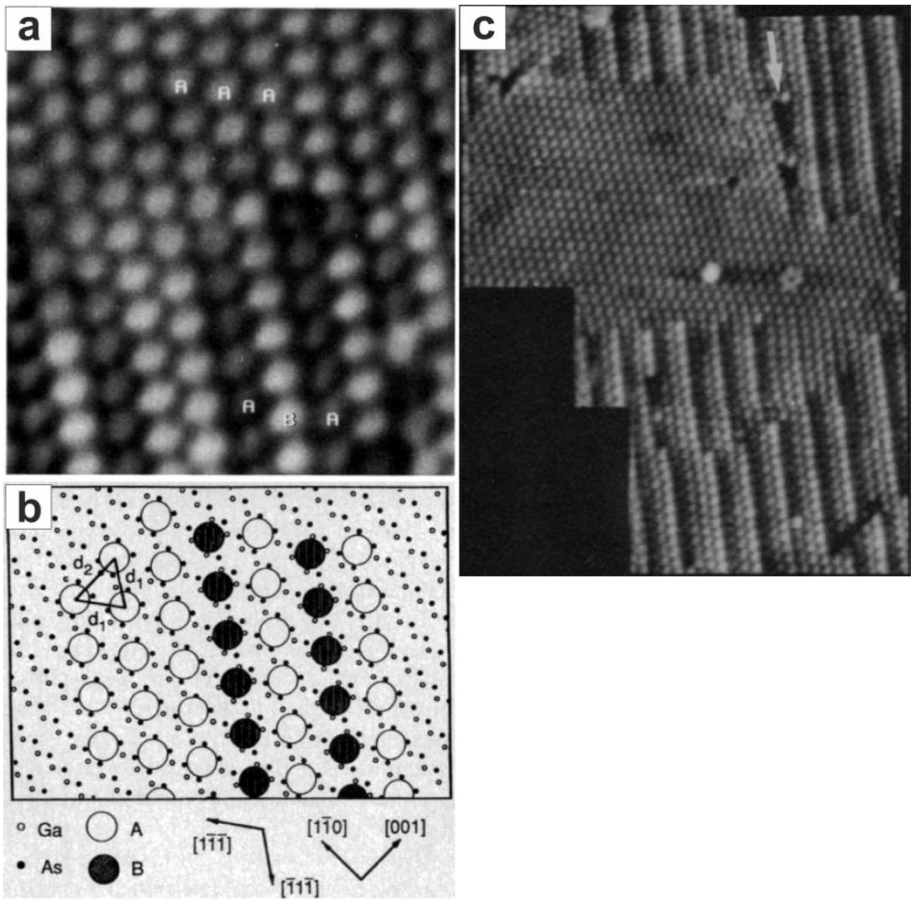

Fig. 3.10 (a) STM image of C_{60} molecules deposited on the GaAs(110) surface. The adsorption sites are marked as "A" and "B" in the figure. (b) A geometrical model, indicating the adsorption sites of C_{60} fullerenes (c) An STM image of multilayer growth of C_{60} deposited at 450 K. The figures are adapted from [154, 155].

$\langle\bar{1}1\bar{1}\rangle$ direction had a measured value of 0.98 nm, whereas the separation along the $\langle 001\rangle$ direction was measured to be 1.13 nm. Upon further increasing the coverage to 3ML at room temperature, C_{60} layers became more complicated and exhibited coexisting flat and corrugated regions [155] (Fig. 3.10c). The flat regions appeared to have a distorted close-packed structure whereas the corrugated part exhibited a combination of structures that resembled the (221) and (533) configuration of the C_{60} FCC bulk structure. Li *et al.* suggested that the formation of these structures is likely due to strain induced by the layers between the lower and upper fullerene layers. They also performed deposition with the substrate held at a temperature of 450 K and 470 K to investigate the growth behaviour of C_{60} films. The corrugated regions were stable up

to 450 K, whereas the flat regions adopted a well-ordered close-packed arrangement for temperatures above 450 K. C_{70} fullerenes have also been ordered on the GaAs(110) surface [156]. Upon deposition of submonolayer coverage at 460 K, C_{70} produced two dimensional islands that exhibited close-packed arrangement with a nearest neighbour distance of 1.01 nm.

The adsorption of C_{60} on the GaAs(100) surface has also been studied. The GaAs(001)-2×6 reconstruction contains channels separated by 2.4 nm that corresponds to the 6× periodicity [157]. Upon an initial deposition (0.01 ML), Xue *et al.* found that C_{60} molecules adsorbed individually and produced clusters on the As-rich GaAs(001)-2×6 surface [158]. Increasing the coverage to ~1ML, C_{60} produced molecular chains that exhibited short range ordering along the $\langle\bar{1}10\rangle$ direction with a close-packed separation varied between 0.95 and 1.35 nm. Molecules adopted a commensurate growth with the substrate along the $\langle 110\rangle$ direction with a close-packed separation of 2.4 nm. The C_{60} appeared to have distinctly different behaviour on As-rich GaAs(001)-2×4 reconstruction [159, 160] as they produced pairs with a separation of 1.18 nm at low coverage (~0.02ML) [117, 161]. Upon further increasing the coverage to 1ML, the pairs became more pronounced and evolved into long parallel chains separated by 1.16 nm. The close-packed separation along the chains had a measured value of 1.13 nm. At higher coverage of C_{60}, crystalline thin films with FCC(110) configuration were obtained where the layers exhibited the same arrangement of linear chains [117, 161]. The formation of FCC(110) oriented films is quite unusual as the FCC(111) configuration has been found to be more favourable on other semiconductor surfaces. This indicates the influence of template surface in dictating the first layer of C_{60} that serves as an efficient template for the growth of further layers. On the As-rich GaAs(001)-c(4×4) reconstruction[157], C_{60} produced two dimensional islands with a close-packed separation of 1.05 nm [117]. At 0.7ML coverage three dimensional islands with FCC(111) orientation were formed without completing the first monolayer.

This is contrary to the behaviour of C_{60} on Ga-rich GaAs(001)-4×4 reconstruction [162] where the growth of a top layer started only after completion of lower fullerene layer [117].

3.2.2.4 Adsorption of fullerenes on TiO_2 surfaces

The adsorption behaviour of fullerenes C_{60} has also been demonstrated on the TiO_2(110) surface [163-165]. The TiO_2(110)-1×2 surface is comprised of a network of parallel one dimensional troughs aligned along the [001] crystallographic direction (Fig. 3.11a and 3.11b) [166]. The troughs are separated by 1.3 nm and connected through perpendicular cross shaped structures. Sequential deposition at room temperature revealed the preferential adsorption of isolated molecules in the troughs of its underlying 1×2 structure [167, 168]. Upon an initial deposition, C_{60} molecules adsorbed at the neighbouring site to the cross link structure and served as nucleation site for molecules on further increasing the deposition [168] (Fig. 3.11c and 3.11d)). With increasing the C_{60} coverage to 1ML, molecules filled up the troughs to form linear chains that appeared to be paired, whereas the separation between two chains in a pair was measured to be 1.1 nm (Fig. 3.11e and 3.11f). At higher coverage of C_{60} (2 ML), multilayers structures were formed on the surface with close-packed arrangement. The second layer exhibited corrugated regions due the influence of the underlying paired chain structures [167].

3.2.3 Fullerenes on $SrTiO_3$ surfaces

3.2.3.1 Fullerenes on nanostructured $SrTiO_3$(001) surfaces

The $SrTiO_3$(001) surface has been shown to host a series of nanostructured surfaces [27, 28]. Deak *et al.* [30, 169, 170] were the first to investigate the self-assembly of fullerenes on the nanostructured $SrTiO_3$(001) surfaces. They used

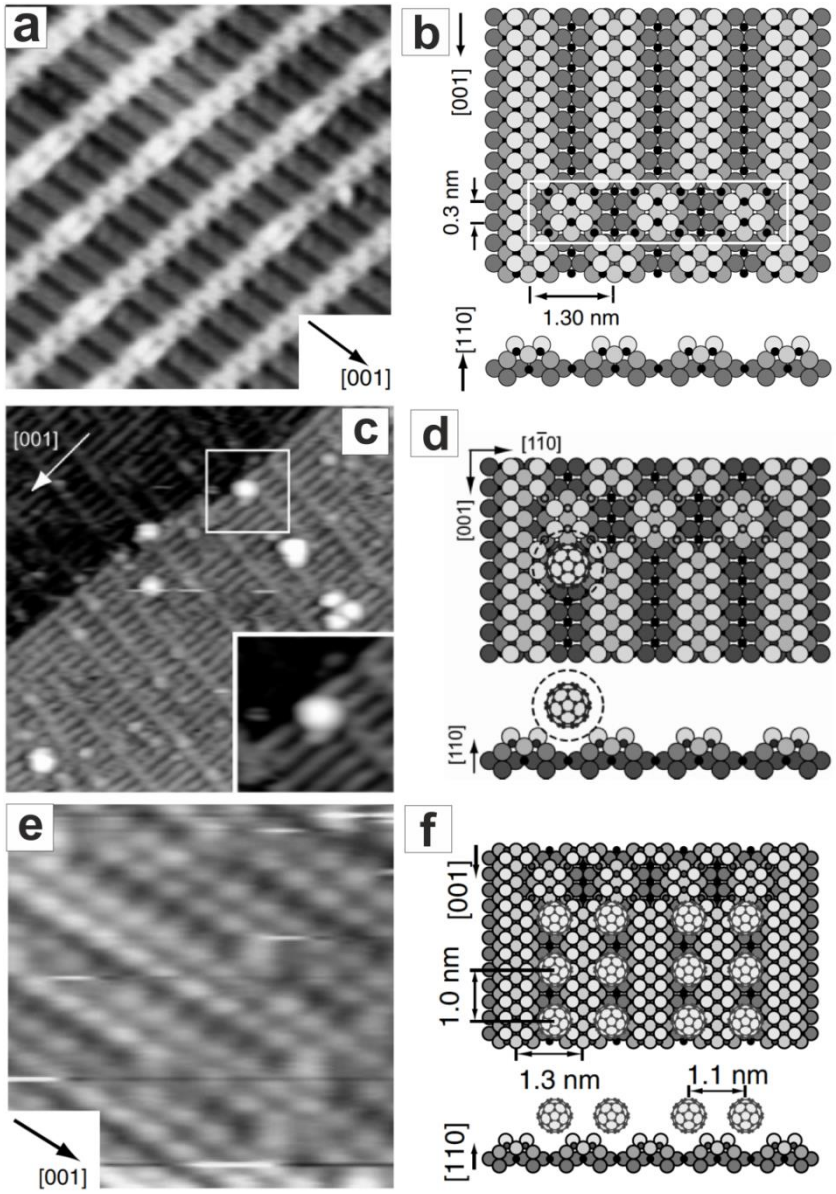

Fig. 3.11 Images showing the interaction of fullerenes C_{60} with the TiO_2 surface. (a) STM image showing the bare surface of TiO_2(110)-1×2 cross link structure. (b) A representative model of TiO_2(110)-1×2 surface. (c) The behaviour of C_{60} at low coverage, where the isolated molecules are adsorbed at sites next to the cross link structures. (d) Proposed model of the adsorption of C_{60} at low coverage. (e) STM image showing C_{60} formed paired chains on the surface. (f) A proposed model showing the arrangement of C_{60} at higher coverage (1 ML). The figures are taken from [167, 168].

$Er_3N@C_{80}$ and C_{70} in their experiments. $Er_3N@C_{80}$ on a mixed surface of c(4×2) and dilines [28] produced close-packed islands on the c(4×2) reconstruction and were rarely observed on the dilines structures [30]. The intermolecular structures of fullerenes were observed indicating that the free rotation of fullerenes is hindered by the c(4×2)

reconstruction. However, island growth was not influenced by the substrate suggesting the fullerene layer is not in registry with the underlying substrate. On the trilines [27], $Er_3N@C_{80}$ showed a different behaviour due to the influence of the substrate surface (Fig.3.12a). Molecules adopted a square packed and hexagonally packed arrangement at the boundary between adjacent trilines and within the triline domain, respectively (Fig. 3.12b). The square packed molecules appeared as domain boundaries between the close-packed structures and run along the island as indicated by arrows in Fig. 3.12c. Another distinct arrangement of $Er_3N@C_{80}$ is observed on a template based on trench structures as shown in Fig. 3.12d. Molecules filled up the trenches to produce linear chains aligned along the [100] direction and comprised of $Er_3N@C_{80}$ pairs. The intermolecular distance within the $Er_3N@C_{80}$ pair had a measured value of 1.2 nm whereas the two nearest pairs had a separation of 1.9 nm. This formed a periodicity of 3.1 nm (8 times that of the bulk unit cell). The final surface used to order $Er_3N@C_{80}$ was based on a waffle structure which is made up of a rectangular grid of trenches with crosslike structures along them [30, 169] (Fig.3.12e). When deposited on this template, $Er_3N@C_{80}$ filled up the waffle structure in pairs and occasionally in triplets. In this way $Er_3N@C_{80}$ pairs formed the basic building block to produce a unique arrangement of 2D open grid array as shown in Fig. 3.12f.

The growth of C_{70} fullerenes has also been investigated on the c(4×2) and crossdot (7×4) nanostructured $SrTiO_3$(001) surface [27]. C_{70} produced small disordered islands on the c(4×2) reconstruction. However, the nanostructured cross dot (7×4) template strongly influenced the ordering of fullerenes [170]. At the initial stage of deposition (0.05 ML), C_{70} produced linear chains along the [100] 4 × direction of the surface and few formed two molecule wide clusters. With further increase of the C_{70} coverage, the clusters and chains served as a nucleation site for other molecules and formed islands, with the largest island being five molecules across (Fig. 3.12g).

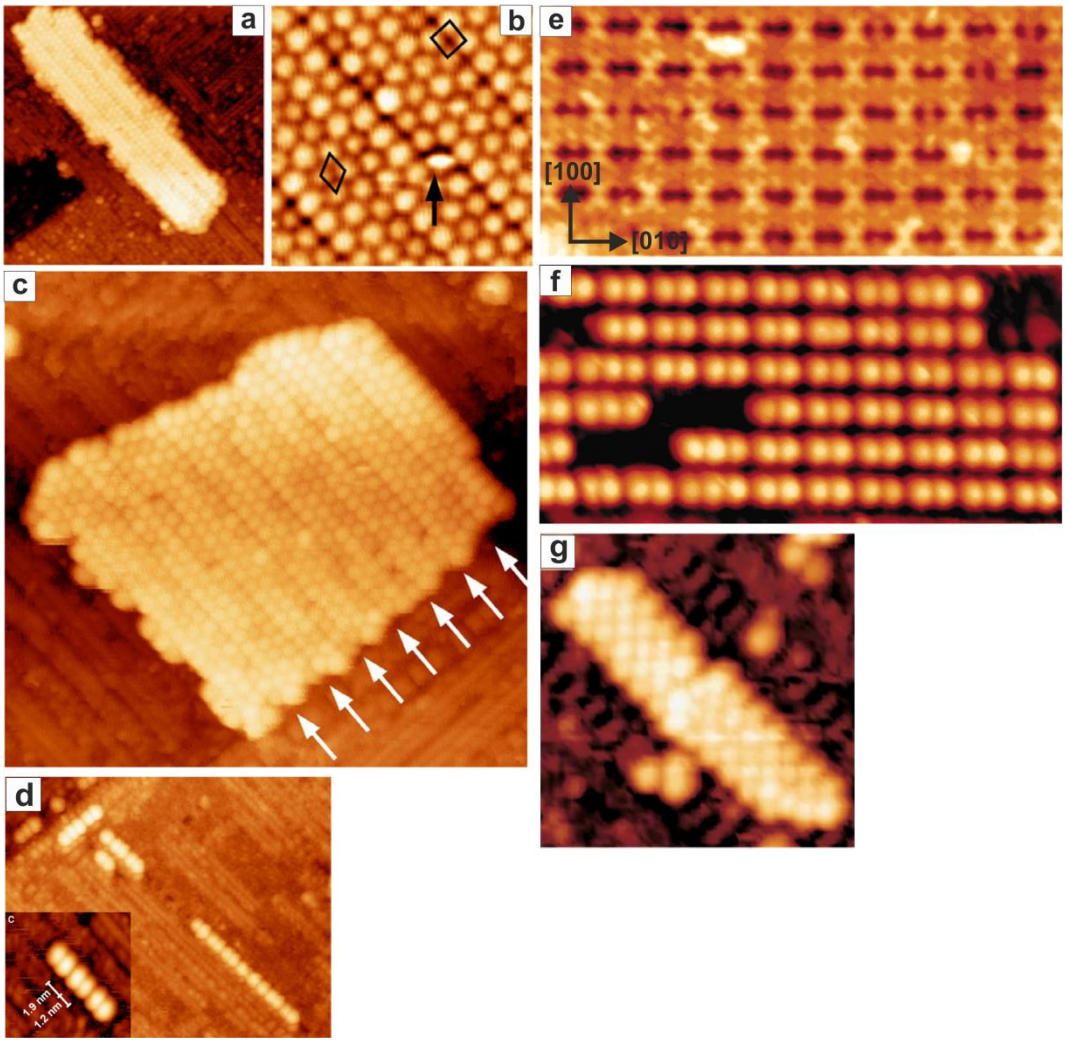

Fig. 3.12 STM images illustrating the growth of fullerenes on nanostructured $SrTiO_3$(001) templates. The images show: (a) an island of $Er_3N@C_{80}$ molecules on the triline (9×2) surface. (b) a magnified STM image showing hexagonal and square packing of molecules on the triline surface. (c) an island of $Er_3N@C_{80}$ molecules on the triline surface. The white arrows indicate the dislocations within the island. (d) linear chains of molecules on the nanostructured (7×4) template. (e) a template based on the nanostructured (6×8) waffle surface. (f) $Er_3N@C_{80}$ molecules anchored into the trenches of waffle structure. (g) An island of C_{70} on the 7×4 surface with square packed arrangement. The images are adapted from references [30, 169, 170].

Recently the growth of C_{60} fullerenes on the nanostructured $SrTiO_3$ (001) surfaces has been reported [171]. Similar to other fullerenes, C_{60} formed disordered islands on the c(4×2) reconstruction. C_{60} appeared to avoid sitting atop the dilines, instead they anchored into the spaces between two neighbouring diline structures. Upon further increasing the C_{60} deposition, molecules formed quasi linear chains aligned along the direction of dilines. Fullerenes produced double chain structures on top of the trilines

with a C_{60}-C_{60} separation of 1nm. Unlike $Er_3N@C_{80}$, the C_{60} molecules avoided to form epitaxial close-packed islands on the trilines due to lattice mismatch. However, tetralines encouraged the formation of close-packed ordering. When deposited on the waffle structure, molecules preferentially filled up the template surface to produce a highly ordered 2D array of molecules similar to that observed by Deak *et al.* for $Er_3N@C_{80}$.

3.2.3.2 Fullerenes on $SrTiO_3$(111) surfaces

Fullerenes C_{60} and C_{70} have also been ordered on the $SrTiO_3$(111)-5×5 reconstruction [55]. C_{60} molecules were deposited on the 5×5 reconstructed surface with the surface heated to 150-180 °C for 30 minutes. After deposition the sample was kept at the same temperature for 6 hours. C_{60} produced close-packed islands with a C_{60}-C_{60} separation of 1.01 nm (Fig. 3.13a). The fullerene layer exhibited depressions of single and three molecules that occurred at a periodicity equivalent to the 5×5 reconstructed surface. This indicated an epitaxial relationship between the overlayer and underlying 5×5 surface. However, the depression of single or three molecules were not periodic over a large area and formed an irregular arrangement. No other ordered phase was observed for C_{60} on the surface.

C_{70} was also deposited on the 5×5 reconstructed surface with the template heated to 170-200 °C. The sample was then kept at 170-200 °C for 8 hours to allow formation of ordered structures. Molecules produced large close-packed islands on the surface, indicating that fullerenes were mobile at the annealing temperature [55]. The overlayer exhibited hexagonally arranged ordered vacancies with a spacing equivalent to the unit cell of the 5×5 reconstruction (Fig.3.13b). However, the fullerene layer appeared not to follow the crystallographic direction of the substrate surface. Instead, the overlayer was rotated by 19.1° with respect to the lattice direction of the underlying 5×5 surface. A schematic representation demonstrating the overlap of fullerene layer with the template

surface is given in Fig. 3.13c. The separation between the two vacancies along the fullerene lattice is 7.31 nm which is equivalent to √7 times the 5×5 unit cell [55]. This formed a √7×√7 arrangement of the fullerene layer. Due to reduced symmetry the C_{70} molecules can adopt two orientations on the surface, i-e. "standing" or "lying down" [172]. In the standing orientation the fullerene layer would adopt a structure similar to C_{60} which was not observed by Russell [55]. Therefore the observed arrangement of C_{70} was attributed to a "lying down" orientation.

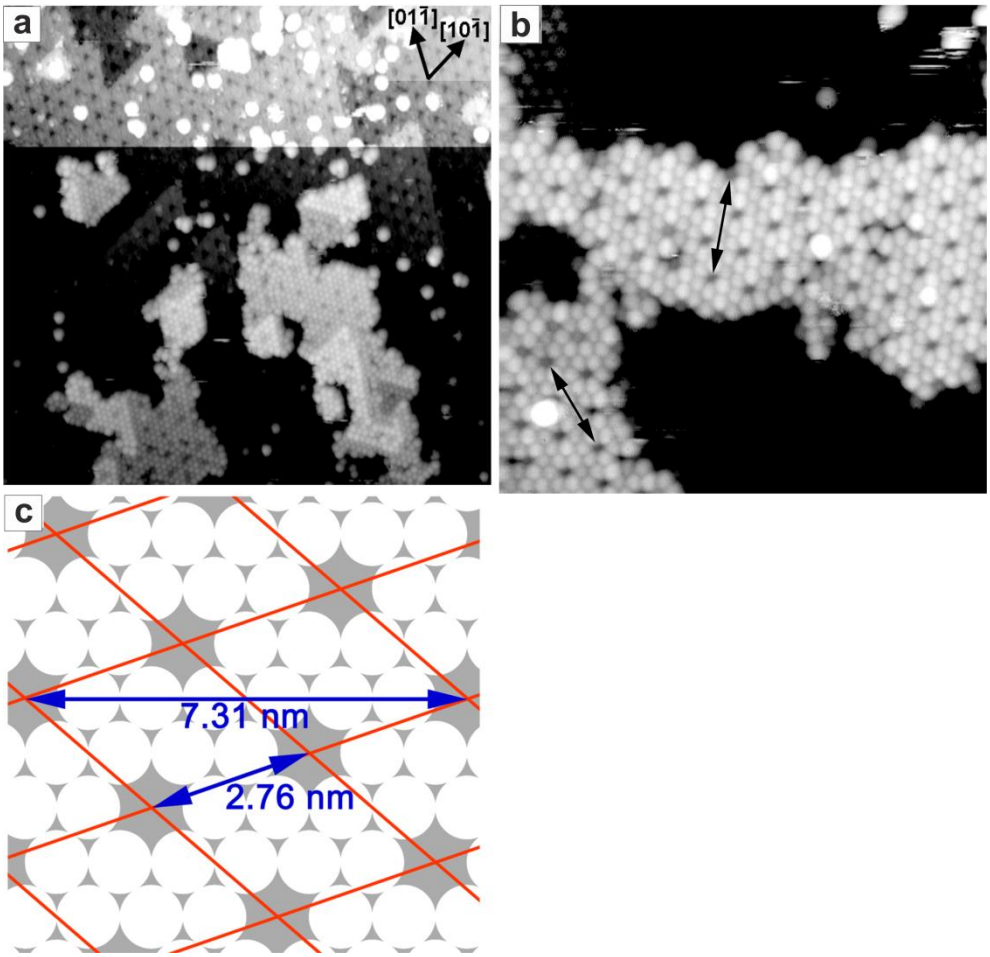

Fig.3.13 (a) STM image showing the formation C_{60} epitaxial close-packed islands on the 5×5 reconstructed surface. (b) STM image of C_{70} islands on 5×5 the reconstruction. The overlayer exhibit hexagonally arranged vacancies. (c) A schematic showing the arrangement of C_{70} molecules in a "lying down" orientation. The separation between two neighbour vacancies corresponds to the 5×5 unit cell, whereas that along the layer is 7.31 nm. The images are adapted from reference [55].

3.2.4 Summary and outlook

There exists a large body of literature on the growth of fullerene molecules on a wide range of solid surfaces. This review section has briefly summarized the research work that has been carried out on the interaction of fullerenes with semiconductors and strontium titanate surfaces. The Si(100) and Si(111) surfaces interact strongly with fullerenes and causes them to adsorb individually without forming close-packed islands. Due to strong molecule-substrate interactions the formation of long range ordered domains is inhibited and only local ordering can be formed. However, close-packed structures of fullerenes can be formed on metal terminated silicon surfaces. On the other hand, fullerenes heavily disrupt the Ge(111) reconstructed surface and induce structural changes upon deposition. GaAs surfaces interact weakly with fullerenes and allow formation of well-ordered close-packed islands. On the non-stoichiometric nanostructured $SrTiO_3$(001) surfaces, the growth of fullerenes is largely driven by the template surface that arrange fullerenes into unique configurations. The surface topography of these distinct surfaces appears to have a dominant role in dictating the self-assembly process. Fullerenes form close-packed epitaxial islands on the $SrTiO_3$(111)-5×5 reconstruction after prolonged annealing of the sample covered with molecules.

Although the growth of fullerenes on the $SrTiO_3$(111)-5×5 reconstructed surface has been studied by Russell [55], a wider investigation is required on the n×n family of reconstructions. This will improve the knowledge in understanding the influence of these non-stoichiometric reconstructed surfaces on the growth of fullerenes and other functional materials. In addition, fullerenes are particularly intriguing from the technological point of view and arranging them into a unique configuration could be useful for their utilization in molecular-based devices.

3.3 Electrical and optical properties of $SrTiO_3$

3.3.1 Paramagnetic centres in $SrTiO_3$

Point defects such as oxygen vacancies or transition metal dopants play an important role in various electrical, magnetic and optical properties of the perovskite oxides [35]. Understanding and controlling the nature of these defects is vitally important, not only from a fundamental point of view, but also for technological developments. In this regard, electron spin resonance spectroscopy (ESR) has been widely used to investigate the paramagnetic centres and their local environment in $SrTiO_3$ [173-186], pioneered by the 1987 Nobel Laureate K. Alex Müller [187, 188]. Transition metal ions, which may be present as impurities or introduced through deliberate doping into $SrTiO_3$, typically substitute for Ti^{4+} ions at the centre of oxygen octahedra in the host lattice. If the valency of the substitutional impurity ion is lower than that of Ti^{4+}, then a charge imbalance occurs with respect to the lattice. In order to maintain the charge neutrality, charge compensation occurs in the form of oxygen vacancies if the compensating impurities are insufficient [189]. The spin Hamiltonians generally used to describe the ESR spectra of point defects is given by Abragam and Bleaney [190].

$$H = \beta \mathbf{BgS} + \mathbf{IA}S + D\left[S_z^2 - \frac{1}{3}S(S+1)\right] + \frac{a}{6}\left[S_x^2 + S_y^2 + S_z^2 - \frac{1}{5}S(S+1)(3S^2+3S-1)\right] + E(S_x^2 - S_y^2)$$

where β is the Bohr magneton, **B** is the magnetic field strength, **g** is a tensor, **S** is the spin operator, **I** is the nuclear spin operator, **A** is the hyperfine coupling tensor. x, y, z denote the [100], [010] and [001] crystallographic directions; *a* is the cubic splitting parameter, D and E are the axial and rhombic zero-field splitting parameters, respectively. In the above equation, the first term describes the Zeeman interactions, the

second term represents the hyperfine interactions between the electron and nuclear spin, the third and fourth terms correspond to the axial and cubic crystal field and the final term indicates the orthorhombic interactions. A brief review of the paramagnetic centres in $SrTiO_3$ is given in the following sections.

3.3.1.1 Iron-based defect centres

Among the transition metals defects, iron (Fe) has been the most widely investigated paramagnetic centre in $SrTiO_3$ [191-197]. This is due to the fact that iron is frequently found even in nominally pure samples and has been shown to take on various charge states in $SrTiO_3$. These point defects provide a probe of the structural phase transition of $SrTiO_3$ [198-200]. For instance, the ESR spectrum of Fe-doped $SrTiO_3$ sample has been shown to exhibit five resonance lines at room temperature that originate from the Fe^{3+} ions ($3d^5$, S = 5/2) located at the Ti site octahedrally coordinated with six oxygen atoms [188, 201]. The spectrum of the Fe^{3+} centre at the cubic site is characterized by the parameters g = 2. 004 and a = 2.00 $\times 10^{-2}$ cm^{-1} [188]. Upon cooling the sample to 80 K, the ESR spectrum responds to the structural phase transition, developing, with resonances splitting into doublets when the magnetic field is parallel to the [100] direction. This behaviour has been attributed to the formation of tetragonal domains whose symmetry axes are aligned with the cubic directions found in the high temperature phase [188]. The spectrum in the tetragonal phase was characterized by adding a small value of zero-field splitting D = (7.7 ± 0.3) × 10^{-4} cm^{-1} to the spin Hamiltonian. In a later study, the Fe^{3+} centre was further analysed by measuring the angular dependence of the ESR spectra at 77 K, where a fine splitting of resonance lines was attributed to the rotation of oxygen octahedra by 1.4° in the (001) plane [200]. This is due to the fact that a structural transition from the cubic to tetragonal phase occurs at 105 K from a rigid rotation of oxygen octahedron about the

[100] direction. The angle of rotation was found to be temperature dependent and determined as 2.1° at 4.2 K [200].

Apart from the cubic Fe^{3+} centre, strong axial field lines in the ESR spectrum have also been reported in the Fe-doped samples [202]. At room temperature, in the cubic phase, Kirkpatrick *et al.* [202] observed that the ESR spectrum exhibited three axially symmetric resonance lines which had symmetry axes along the [100], [010] and [001] crystallographic directions (Fig. 3.14a). The corresponding g values were measured between 2 and 6, whilst hyperfine splittings of the resonance lines were not observed. The spectrum was analysed by assigning S = 5/2 to a system with a giant zero field splitting, D ≈ 1.42 cm^{-1}, and identified as charge-compensated Fe^{3+} ions paired with oxygen vacancies (V_O) [202]. The formation of an oxygen vacancy in the first coordination sphere breaks the octahedral symmetry of the Fe^{3+} ion, and results in a strong crystal field. The results were re-examined by Baer *et al.* [203] and Pontin *et al.* [204], who performed measurements at higher frequencies and refined the spin Hamiltonian by considering higher order terms. The properties of Fe^{3+}-V_O complex in $SrTiO_3$ were further studied at low temperatures [198, 200]. Similar to the behaviour of Fe^{3+} (cubic) centre in the tetragonal phase, the spectrum due to Fe^{3+}-V_O also exhibited further splitting of the resonance lines. However, the rotation angle of the oxygen octahedral containing the Fe^{3+}-V_O centre was measured to be smaller than that of Fe^{3+} (cubic) centre [200]. Due to large splitting of the resonance lines and small line width, the rotation angle of the Fe^{3+}-V_O complex was determined with high accuracy. The rotational dependence of the splitting of Fe^{3+}-V_O centre was found to be temperature dependent, hence provided a useful probe to investigate the behaviour of $SrTiO_3$ both in the cubic and tetragonal phases [198]. A weak orthorhombic term $E(S_x^2 - S_y^2)$ due to the phase transitions was added to the spin Hamiltonian to fit the experimental data. The orthorhombic term was found to be temperature dependent and proportional to the square of rotational angle φ. In the tetragonal phase (78K), the value of E was

determined to be around 1.82 cm^{-1} [198]. Upon cooling the sample to 25K and subjecting it to optical illumination of wavelength 396 nm, the ESR spectrum revealed a hole centre belonging to Fe^{2+}-O^- [205]. The spectrum due to Fe^{2+}-O^- centre was observed to be stable in the temperature range 1.8-35 K, above which the holes were freed and another unidentified centre called $\boldsymbol{I_1}$ appeared [206].

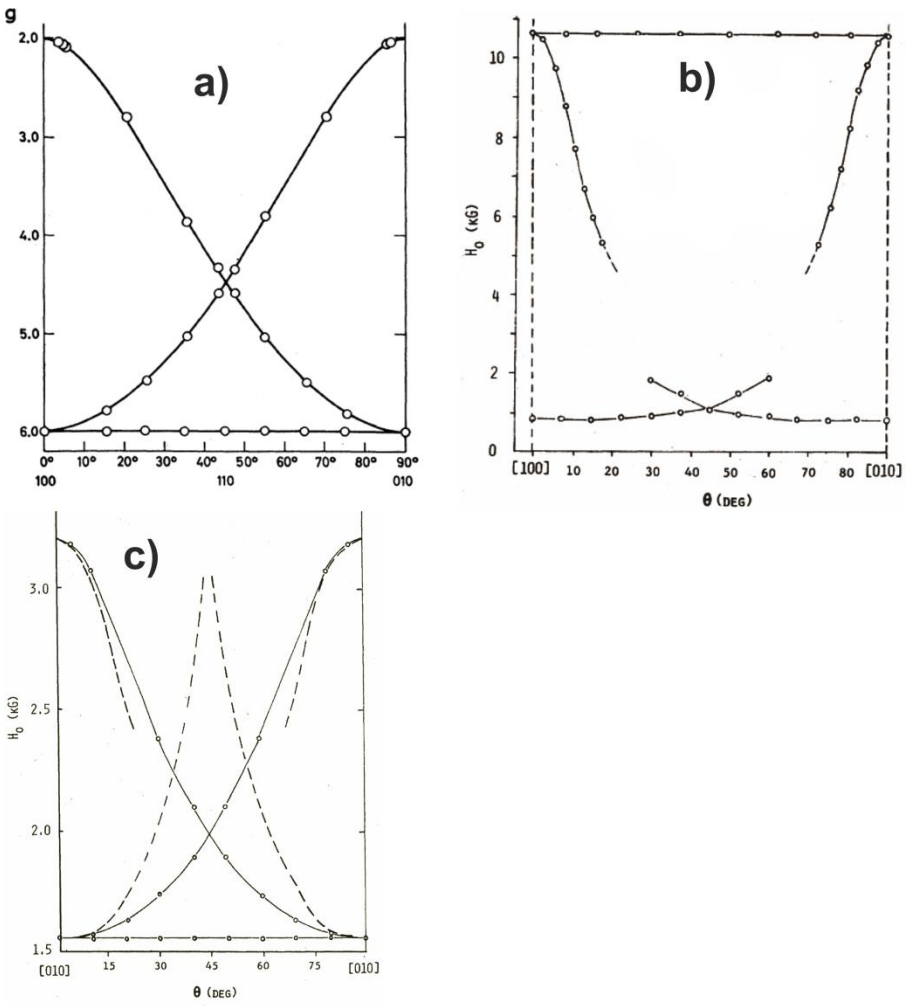

Fig. 3.14 (a) The angular dependence of the Fe^{3+}-V_O centre resonance in the cubic phase of $SrTiO_3$. The points are the measured data and the solid lines are theoretically calculated curves. (b) The rotational behaviour of the ESR spectrum of Fe^{2+}-V_O complex. (c) The angular dependence of the Fe^{1+}-V_O complex with magnetic field rotated in the (001) plane. The points represent the measured data and the solid line correspond to the calculated resonance field for the S = 3/2. The dashed lines represent an alternative model for S = 5/2, which is deviated from the actual experimental data. The figures are adapted from references [191, 202].

In addition to the Fe^{3+} and Fe^{3+}-V_O complex, a partially characterized centre belonging to the Fe^{3+}-*I* (charge compensated interstitial impurity) has also been

observed in the as-received samples by Berney *et al.* [191, 192]. Heating Fe-doped $SrTiO_3$ single crystal at 1100 K in the presence of hydrogen gas resulted in the reduction of Fe^{3+}-V_O centre and produced another centre ascribed to a Fe^{2+}-V_O complex (S=2). The resonance lines due to this centre were observed at the high magnetic field 10.5 kG, and at the low magnetic fields around 0.8 kG as shown in Fig. 3.14b. During the reduction process, the Fermi level is expected to rise due to the formation of oxygen vacancies, which change the charge state of the iron vacancies, converting Fe^{3+}-V_O centres into Fe^{2+}-V_O by the addition of electrons [191]. Moreover, the Fe^{3+}-*I* accept an electron during reduction to become ESR silent. When the reduced samples were subjected to subband-gap light, the signals due to the Fe^{3+}-*I* centre reappeared along with a new axial centre that has been assigned to Fe^{1+} -V_O. Upon illumination, charge transfer of an electron took place from the valence band to the Fe^{2+} -V_O complex, resulted in the formation of Fe^{1+} -V_O [191]. The hole was subsequently captured by the Fe^{2+}-*I* or (Fe^{3+}-*I* + *e*) centre to produce Fe^{3+}-*I*. The Fe^{1+} -V_O charge state appeared to be stable below 200 K. The ESR spectrum of the Fe^{1+}-V_O centre had *g*-values given by: $g_{\parallel} = 1.999$ and $g_{\perp} = 4.116$ (Fig. 3.14c). In the tetragonal phase, Berney *et al.* [191, 192] analysed the spectrum due to Fe^{1+} -V_O centre by adding a small value of D = 0.12 cm^{-1} to the spin Hamiltonian.

Further iron-based defect centres have been observed upon heating the sample in an oxidizing environment, which produced the Fe^{4+}-V_O and Fe^{5+} defect centres [207], with the ESR spectrum of the Fe^{4+} -V_O complex characterized by a cubic splitting *a* = (0.1504 ± 0.0008) cm^{-1} and $g_{\parallel} = 2.007 \pm 0.001$. At 4.2 K, both Fe^{4+} -V_O and Fe^{3+}-V_O centres co-exist in the ESR spectrum, whilst inter-conversion from Fe^{4+}-V_O to Fe^{3+}-V_O complexes took place via charge transfer when the sample was illuminated with 1.8-3.1eV photons – under illumination, the intensity of Fe^{4+}-V_O complex decreased, whilst concurrently the Fe^{3+}-V_O increased, suggested that during illumination electrons are excited from the valence band and are trapped by the impurity level, resulting in the

increase of Fe^{3+}-V_O concentration [207]. The holes created during the excitation process were subsequently captured by the Fe^{3+}centres to produce Fe^{4+} [208, 209]. From wavelength dependent data, the position of $Fe^{3+/4+}$-V_O defect level was determined to be 2.3eV which is contrary to that reported in earlier studies, where the defect level was estimated as 1.35eV above the valence band [210]. This discrepancy is most likely arises due to limited wavelength range of photons used by Schirmer *et al.* [207]. In a recent study, a similar approach has been used to study the electron transfer mechanisms between $Fe^{4+/5+}$ and $Fe^{3+/4+}$-V_O defect centres and identified the position of defect levels within the band gap by using photons of energies between ~ 0.8–3.0 eV [194]. The $Fe^{3+/4+}$-V_O complex appeared to be optically active and its intensity varied with illumination even at low energies. In this study, the energy level of $Fe^{3+/4+}$-V_O centre was determined to be 1.2 eV above the valence band edge. On the other hand, the intensity of Fe^{5+} centre was enhanced by 2.8 eV light, and the location of Fe^{5+} was suggested to be 0.77 eV above the conduction band edge, consistent with the earlier reports [210]. The ESR spectrum of Fe^{5+} centre appeared to be isotropic and characterized by the parameters: g = 2.0131 ± 0.0008 and A(^{57}Fe) = 8.6 ± 0.1 × 10^{-4} cm-^{1} [211]. Another defect centre due to Fe^{5+} at the non-cubic cite has also been identified [212]. The behaviour of this centre was found to be similar to that of Fe^{3+}-V_O complex. The ESR spectrum at 115 K appeared to be anisotropic and analysed by the following the parameters: $g_{\parallel} = 2.0132 \pm 0.0010$, $g_{\perp} = 2.0116 \pm 0.0010$ and |2D| = 0.541 cm^{-1} [212]. Below the structural phase transition (at 77 K), the resonance lines exhibited additional splittings and a weak orthorhombic term was added to the spin Hamiltonian [213]. The value of |2D| and |E| in the orthorhombic phase were estimated as 0.551 cm^{-1} and 0.529 ×10^{-3} cm^{-1}, respectively. The orthorhombic term was observed to be temperature dependent and proportional to the square of intrinsic rotation angle i.e., φ^2. The rotation angle of the non-cubic Fe^{5+} centre was found to be greater than the

intrinsic angle owing to the expansion of its adjacent octahedron. It is suggested that this could arise due to the neighbouring Ti vacancy [199].

3.3.1.2 Defects containing Cr

Chromium centres have also been widely investigated in $SrTiO_3$ [214-219]. In the case of perfectly oxygen stoichiometric samples, the Cr^{4+} ions substitute for Ti^{4+} [220]. Although the tetravalent Cr has a paramagnetic state with spin S = 1, it has not been observed at X-band frequency due to a strong crystal field splitting, e.g. $|D| >> g\mu_B B$ [220]. The tetravalent charged state can be converted to Cr^{3+} by optical illumination with photons of energy greater than 1.5 eV or through electron doping [220, 221]. The photoinduced Cr^{3+} centre has been observed to be a metastable state, which relaxes back to tetravalent state after switching off the light [220-222]. However, stable Cr^{3+} centres can be obtained in the ESR spectrum if the crystal contains defects i.e., is non-stoichiometry [188, 223, 224]. For instance, Meierling [224] observed two types of Cr^{3+} centres in $SrTiO_3$ samples annealed in an oxidizing environment. The room temperature ESR spectrum exhibited an isotropic resonance line with large intensity, originating from cubic Cr^{3+} ions, and a 4000 times weaker signal assigned to Cr^{3+} ions with orthorhombic symmetry which involved the oxygen vacancies (V_O) for charge compensation. The ESR spectrum of the cubic Cr^{3+} centre exhibited a central line at g = 1.978, and a set of four hyperfine satellites due to the ^{53}Cr isotope (I_n = 3/2). The Cr^{3+}-V_O (ortho) complex was characterized by the parameters $g_x = g_y = 1.9761 \pm 0.0005$, $g_z = 1.9783 \pm 0.0005$, $D = 0.466 \pm 0.002$ cm^{-1}, $E = 0.273 \pm 0.005$ cm^{-1} and $A = 16.2 \pm 0.3 \times 10^{-4}$ cm^{-1} [224]. The symmetry of Cr^{3+} ions can be controlled by annealing the sample in a reducing atmosphere or through chemical doping of the sample with electron donors as reported by Mattina *et al.* [220]. Doping with Nb, which acts as electron donor, changed the oxidation state of Cr from +4 to +3 charge state and the ESR spectrum appeared to be isotropic. This indicated that the symmetry of Cr^{3+} centre

remained unchanged with chemical doping and that $Cr^{4+/3+}$ ions occupied the cubic octahedral site. However, the symmetry was observed to change from cubic to axial upon reducing the sample, which could be understood as the effect of incorporating oxygen vacancies. There appeared to be a strong correlation between Cr^{3+} ions and oxygen vacancies (V_O) which lowered the symmetry of Cr^{3+} ions from cubic to axial [220]. This is due to the fact that a small crystal field was produced on the Cr ions by the presence of oxygen vacancies. The magnitude of the crystal field parameter was determined to be 8.3 MHz which indicated that the oxygen vacancies were located in the third coordination sphere. At temperatures below the structural phase transition, Cr^{3+}-V_O complex has been found to become slightly tetragonal [225, 226]. In addition to the Cr^{3+}-V_O complex, Cr^{5+} and Cr^{3+} centres with axial and rhombic symmetry were observed in crystals with Sr-deficient $SrTiO_3$ single crystals [225].

3.3.1.3 Defects containing Mn

The substitutional character of Mn ions in $SrTiO_3$ has also been investigated [227-232]. As-received Mn-doped $SrTiO_3$ revealed six isotopic hyperfine lines in the ESR spectrum as reported by Muller [233]. The lines were characterised by the following g-value and hyperfine constant: $g = 1.994 \pm 0.001$ and $A = 75 \pm 1$ G or 69.4×10^{-4} cm^{-1}. These six main hyperfine lines were attributed to the Mn^{4+} ($3d^3$, $S = 3/2$) at a Ti^{4+} position. When the sample was annealed in a reducing atmosphere, the ESR spectrum due to Mn^{4+} disappeared and three new centres associated with lower charge states of Mn were detected [227, 234]. The first centre is based on the Mn^{2+} ($3d^5$, $S = 5/2$) which appeared with a strong intensity in the ESR spectrum and exhibited an isotropic set of six lines at $g = 2$. The hyperfine structure of this centre was found to be 82.6 ± 0.1 G or 69.4×10^{-4} cm^{-1}. The second centre is based on the Mn^{2+} ion associated with an oxygen vacancy i.e., Mn^{2+}-V_O complex ($S = 5/2$). The ESR spectrum of this centre was highly anisotropic with effective g-values of $g_{\parallel} \cong 2$ and $g_{\perp} = 5.9$ similar to

those observed for the Fe^{3+}-V_O [202]. The resonance lines of the third centre also appeared to be anisotropic due to a strong axial field produced by the nearest neighbour oxygen vacancy and characterized by the parameters $g_{\|} \cong 8$, $g_{\perp} < 0.4$ and $a = 0.054 \pm 0.001$ cm^{-1} [234]. The spectrum was attributed to the Mn^{3+}-V_O complex ($3d^4$, S = 2). However, recently the Mn^{3+} centres have been re-examined in more detail and three distinct type of centres belonging to Mn^{3+} complex with axial symmetry have been resolved [235, 236]. The ESR spectra of these centres were characterized by $g_{\|} < g_{\perp} < 2$ and assigned as Mn^{3+}-V_O (I), Mn^{3+}-V_O (II) and Mn^{3+}- X. The Mn^{3+}-V_O (I) centre is found to be similar to that reported by Serway *et al.* [234], where the charge compensation involved an oxygen vacancy in the first coordination sphere. The oxygen vacancy in the Mn^{3+}-V_O (II) centre was proposed to be in the third coordination sphere similar to that observed in the case of Cr^{3+}-V_O complex [220]. The Mn^{3+}-X complex involved transition metal (Nb^{5+}) substituting for nearest neighbour Ti ions to provide the charge compensation [235].

3.3.1.4 The Ti^{3+} centres

Irradiating the undoped $SrTiO_3$ single crystals with fast neutrons or thermal reduction also produced paramagnetic defects [237, 238]. The defect centres have been identified to arise from the Ti^{3+} ions situated on the Sr^{2+} site. It was suggested that Ti ions are knocked out of the lattice and migrate to the Sr site during irradiation. The behaviour of ESR spectra due to the Ti^{3+} was investigated in measurements both below and above the structural phase of $SrTiO_3$ [237]. The Ti^{3+} centre exhibited orthorhombic symmetry at 77K due to distortion in the tetragonal phase. The anisotropic g values and hyperfine structure, measured from the ESR spectrum, for the orthorhombic symmetry were: $g_x = 1.9228$, $g_y = 1.8530$, $g_z = 1.9945$ and $A_x = 13.5\times10^{-4}$ cm^{-1}, $A_y = 16.4\times10^{-4}$ cm^{-1}, $A_z = 2.7 \times10^{-4}$ cm^{-1}. At temperature around 113 K, the orthorhombic centre disappeared and a new axial spectrum with tetragonal symmetry was observed. The

measured g-values for the tetragonal symmetry Ti^{3+} were: $g_{\parallel} = 1.9940,\ g_{\perp} = 1.8905$. It was suggested that the low symmetry is due to an off centre position of Ti^{3+}, i.e., Ti ions are not ideally located at the Sr site [237]. This is due to the fact that the ionic radii of Ti is smaller than that of Sr, and so the titanium atom prefers to move off centre towards one of the twelve nearby oxygen ions [239]. The same Ti^{3+} centres have also been observed in crystals grown by different methods, when Sr vacancies were formed during the growth process and the Ti ions then displaced during the reduction process [240]. Apart from thermal reduction or irradiation, Ti^{3+} centres have also been observed when the samples were illuminated with photon of energy close or greater than the band gap of $SrTiO_3$ [241]. In contrast to the case for irradiated samples, the Ti^{3+} centres in illuminated samples have been suggested to originate from the in-site position Ti ions which are slightly perturbed by an unknown impurity which occupy the Ti^{4+} site in the immediate neighbourhood due to which the Ti^{3+} centres exhibit orthorhombic symmetry in the cubic phase [241].

3.3.2 Electrical transport properties

The electrical properties of $SrTiO_3$ can be significantly altered by varying the oxygen content in the lattice [39, 242-246]. One of the simplest routes to control the electrical transport in $SrTiO_3$ is high temperature treatment in an environment where the oxygen partial pressure can be varied. The oxygen vacancies can lead to n-type doping of material [244, 246]. Increase in the oxygen partial pressure reduces the carrier concentration and hence electrical conductivity. However, understanding the nature of the oxygen vacancy is essential for elucidating the electrical activity of pure $SrTiO_3$.

Yamada and Miller [247] heated the $SrTiO_3$ single crystals in a reducing atmosphere at temperatures between 1200-1400 °C in order to classify the situation regarding point defects. The dominant defects in reduced crystals at room temperature,

based on the optical and electrical measurements, were found to be doubly ionized oxygen vacancies ($V_O^{\bullet\bullet}$). Ab initio study of a single oxygen vacancy in $SrTiO_3$ by Astala and Bristowe [248] also revealed that the doubly positively charged state of the oxygen vacancy was energetically most stable. The interaction between oxygen vacancies was also addressed by Cuong *et al.* [249]. Their computational results suggested that oxygen vacancies prefer to produce clusters in a linear configuration. An apical divacancy oriented along the *z*-direction was found to be the lowest energy configuration and generate a localized state in the bandgap. These observations are, however, in contrast with the picture of vacancy interaction reported by Hou and Terakura [250]. Using the first-principles calculations with the correction of on-site Coulomb interaction, they showed that single oxygen vacancy energetically preferred the singly-ionized state. Furthermore, the most stable configuration for oxygen divacancy was found to be shoulder-to-shoulder in the *xy* plane, rather than head-to-head along the *z*-direction as was predicted by Cuong *et al.* [249].

Defects other than oxygen vacancies such as dislocations in single crystalline material are also important in the context of defect driven physical properties [251]. $SrTiO_3$ has been shown to have an increased density of dislocations in the 'skin' region with respect to the bulk [252]. Dislocations are often accompanied by a distorted lattice in the skin region and provide easy diffusion paths [253] to oxygen under reducing conditions. The inhomogeneity of the thermal reduction process in $SrTiO_3$ single crystal is evidenced in the report of Szot *et al.* [254]. They observed a metallic behaviour in the reduced crystals which was attributed to a high density of vacancies formed along a network of extended defects within the 'skin' region. Prolonged annealing of the sample in low oxygen environment led to breakdown of metallic state as a result of a self-healing phenomenon as shown in Fig. 3.15. The electrical resistivity initially decreased substantially with time, and went through a minimum (stage II).

Annealing the sample for longer time resulted in an increase of the electrical resistivity which saturated at last at point B.

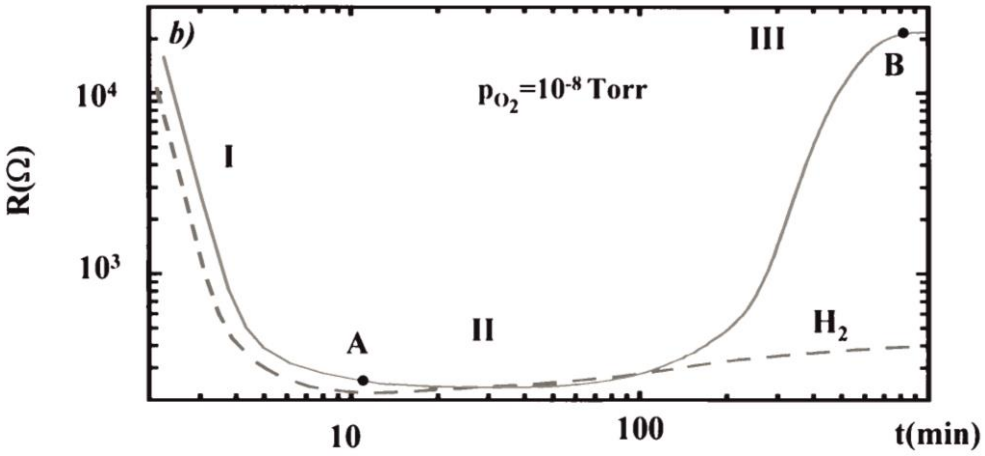

Fig. 3.15 Annealing time dependence of the electrical resistivity of $SrTiO_3$ single crystal in H_2-enriched (dashed line) and oxygen deficient environment (solid line). The annealing temperature is 800 °C. The figure is taken from [254].

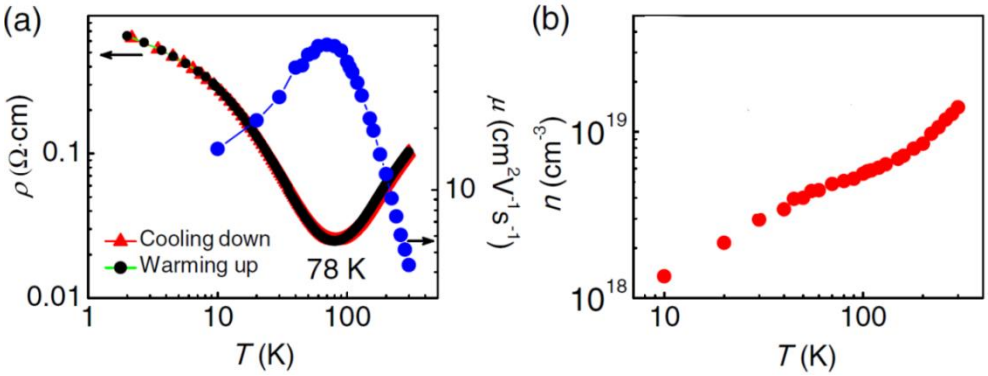

Fig. 3.16 (a) Resistivity (ρ) as a function of temperature (*T*) measured while cooling down and warming up the sample, and temperature dependence of the carrier mobility, μ. (b) Temperature dependence of carrier density, *n* (data taken from reference [255]).

Liu *et al.* [255] reported the electrical transport properties of the reduced $SrTiO_3$ thin films in which oxygen vacancies were expected to be uniformly distributed. These films displayed a metal-insulator transition (MIT) at around 78 K (shown in Fig. 3.16a). The MIT behaviour in these films is attributed to the carrier-freeze-out effect (Fig. 3.16b) where carrier density is found to decreases with decreasing temperature. Liu *et al.* also compared the electrical properties of these films with those of reduced bulk

$SrTiO_3$ single crystal and found a gradient in the density of oxygen vacancies from surface to interior of the crystal.

Reduction processes other than thermal annealing of the sample in UHV/H_2 environment, such as hydrogen plasma cleaning method and Ar^+-ion bombardment, were also used to electron-dope the crystals [256-259]. Takahashi *et al.* [256] applied hydrogen plasma to the $SrTiO_3$ single crystal and termed the resulting samples 'single crystal thin films' of doped material. The temperature dependence of the resistance of the resulting sample surface revealed metallic behaviour (Fig. 3.17). Takahashi *et al.* estimated the thickness of the conducting region as ~0.65 μm, and transport properties of the thin film were found to be identical to that of a reduced single crystal.

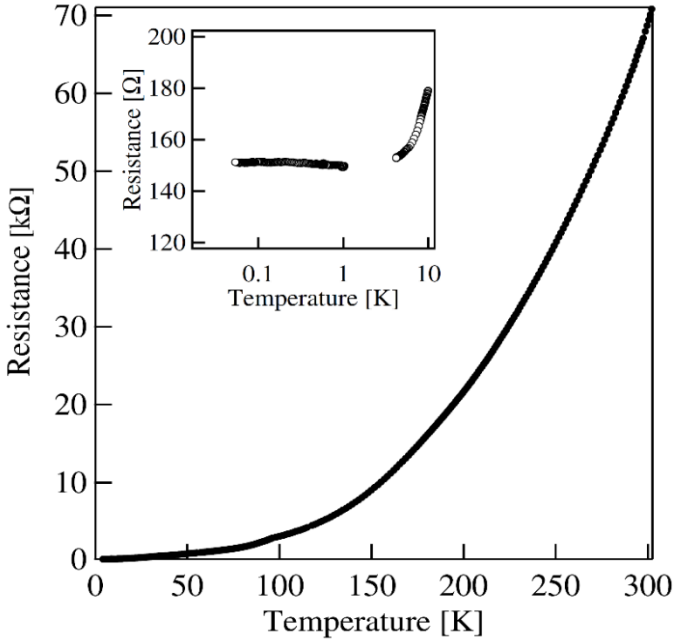

Fig. 3.17 Resistance as a function of temperature for a surface reduced $SrTiO_3$ single crystal with the inset showing resistance in the temperature range 10.00-0.06 K. This material is prepared by applying a hydrogen plasma to a thin film of $SrTiO_3$, data taken from ref. [256].

In another report, relaxation of the transport properties was observed when $SrTiO_3$ single crystal were doped with the aid of Ar^+ irradiation [257]. The temperature dependence of the Ar^+ irradiated samples revealed a conductive behaviour (Fig. 3.18a). Following Ar^+ bombardment, Schultz and Klein [257] found that the sheet resistance of

the sample increased with time, waiting interval after irradiation, at a temperature-dependent rate (Fig. 3.18b). The qualitative temperature dependence trend of the sheet resistance, however, remained the same. The temperature dependence of the resistance recovery rate, shown in the inset of Fig. 3.18b, follows an Arrhenius law with an activation energy of 0.97 ± 0.01 eV, which is found to be consistent with the activation energy of diffusing oxygen vacancies in $SrTiO_3$ [260]. The observed relaxation effects in the resistivity were attributed to the diffusion of oxygen vacancies [257].

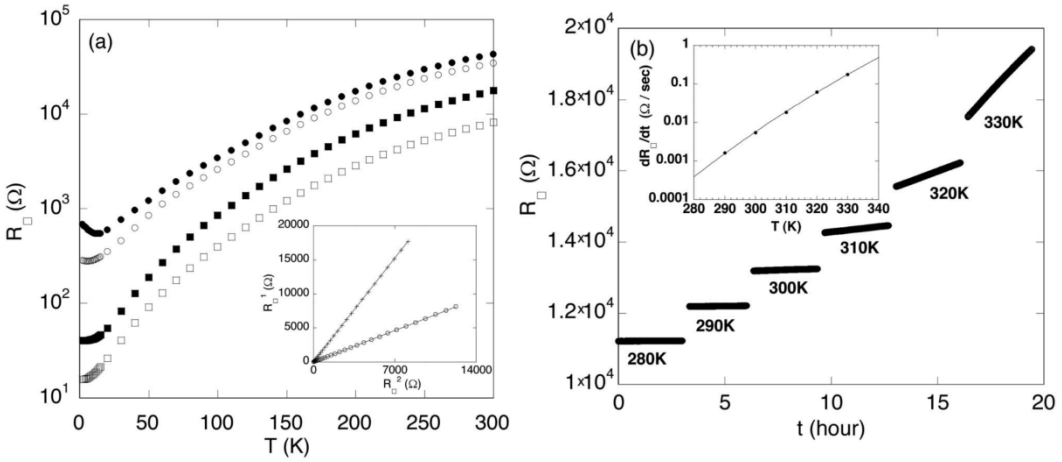

Fig. 3.18 (a) Temperature dependence of the sheet resistance (R□) for $SrTiO_3$ single crystal irradiated for 30 sec (circles) and 90 sec (squares). Open (full) symbols show the data taken shortly after (several days) irradiation. (b) Sheet resistance as a function of time at various temperatures. Inset shows the rate of change of sheet resistance as a function of temperature (circle), where solid line is the fit to the data. The figure is adapted from ref. [257].

3.3.3 Cathodoluminescence properties of $SrTiO_3$

Perovskite oxides such as $SrTiO_3$, $BaTiO_3$ and $(Ba,Sr)TiO_3$ have been extensively studied in the context of oxide-based electronics. Such materials, being able to accommodate various non-stoichiometries, have been shown to exhibit a broad spectrum of functional properties. $SrTiO_3$ is a typical band insulator with a bandgap of 3.2 eV [261]. Carrier doping, however, generates electronic states within the bandgap of the material. Moreover, structural disorders and non-stoichiometries lead to the creation of new electronic levels in the band gap. Such modifications can significantly influence the physical properties of the material. Hence, it is potentially important to

investigate the electronic band structure of the material. In this context, cathodoluminescence (CL) and photoluminescence (PL) spectroscopy are often employed, being powerful techniques that directly detect the optical transitions of defect centres. Depth resolved CL (DRCL) is capable of providing useful information about defect distribution within the material [262-264].

Undoped $SrTiO_3$ is known to emit green ($\lambda \sim 540$ nm) and infrared ($\lambda \sim 800$ nm) luminescence at low temperature ($T < 110$ K), whilst stoichiometric $SrTiO_3$ shows no emission at room temperature [265, 266], though thermal annealing of the crystal induces luminescence at room temperature as shown by Rho *et al.* [267]. Ion irradiation is also known to induce blue emission in $SrTiO_3$ [1, 268-270]. The present section will mainly review the CL studies carried out on undoped and reduced $SrTiO_3$.

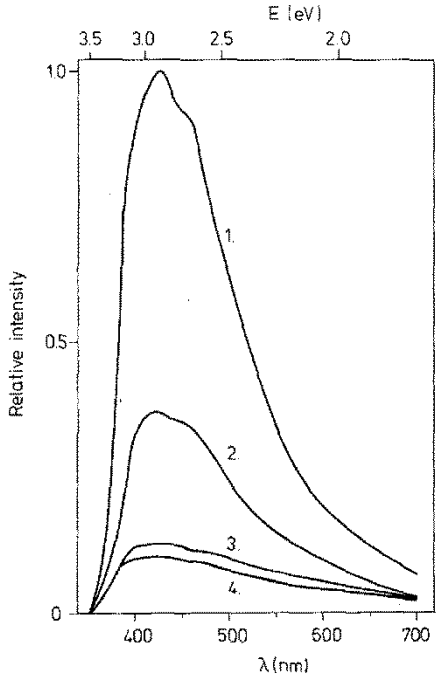

Fig. 3.19 CL spectra of $SrTiO_3$ ceramics first annealed in air at 1450 °C, then reduced in a dry hydrogen stream at 1100 °C for 30 minutes and afterwards doped with La. Curves 1-4 represent the CL spectra of samples doped with 2.0 mole %, 1.0 mole %, 0.3 mole % and undoped respectively. The figure is adapted from ref. [271].

Room temperature CL studies on $SrTiO_3$, $BaTiO_3$ and TiO_2 by Ihrig *et al.* [271] showed similar CL spectra for all three materials. The authors showed that shape and

location of the observed bands remained unaffected by doping and/or thermal treatment in reducing atmosphere (Fig. 3.19). Since all three materials have valence bands derived from O^{2-}-2p levels and low lying conduction bands derived from Ti^{3+}-3d states, similarity of the spectral distribution of CL was interpreted as the emission process being dependent on the electronic structure of these perovskites and independent of the sample preparation and impurities.

The luminescence processes in titanate perovskites are attributed to various phenomena such as self-trapped excitons (STE's) [272, 273], oxygen vacancies, surface states [274], charge transfer vibronic excitons (CTVE's) [275, 276] and transitions associated with intrinsic defects in the TiO_6 complexes [277, 278]. To elucidate the mechanism of luminescence processes, Yang *et al.* [279] reported a detailed analysis of the CL spectra for undoped and doped $SrTiO_3$ samples annealed both in air and low oxygen partial pressure (PO_2). Deconvolution of the CL spectra revealed five components; blue (2.9 eV), green (2.4 eV), IR (1.57 eV, 1.55 eV, 1.44 eV). Fig. 3.20(a-c) shows the CL spectra of the as-received single crystal, annealed in air and low P O_2. The authors also derived a diagram of the electronic levels generated by intrinsic or extrinsic defects within the bandgap (Fig.3.20d). The existence of luminescence bands in untreated $SrTiO_3$ single crystal indicates that the as-received crystal is non-stoichiometric and exhibits intrinsic defects. The 2.9 eV emission was assigned to an electronic transition between a donor state generated by a doubly ionized oxygen vacancy and the valence band i.e. $V_O^{\bullet\bullet} \rightarrow$ VB. The lower intensity of this component in Fig.3.20b is understood as the result of air annealing reducing the number of oxygen vacancies in the sample. The 2.4 eV emission was interpreted as a charge transfer between Ti^{4+} and O^{2-} via intrinsic CTVEs, whilst IR emission was assigned to STE's between in-gap states involving Schottky intrinsic defects (Fig.3.20d).

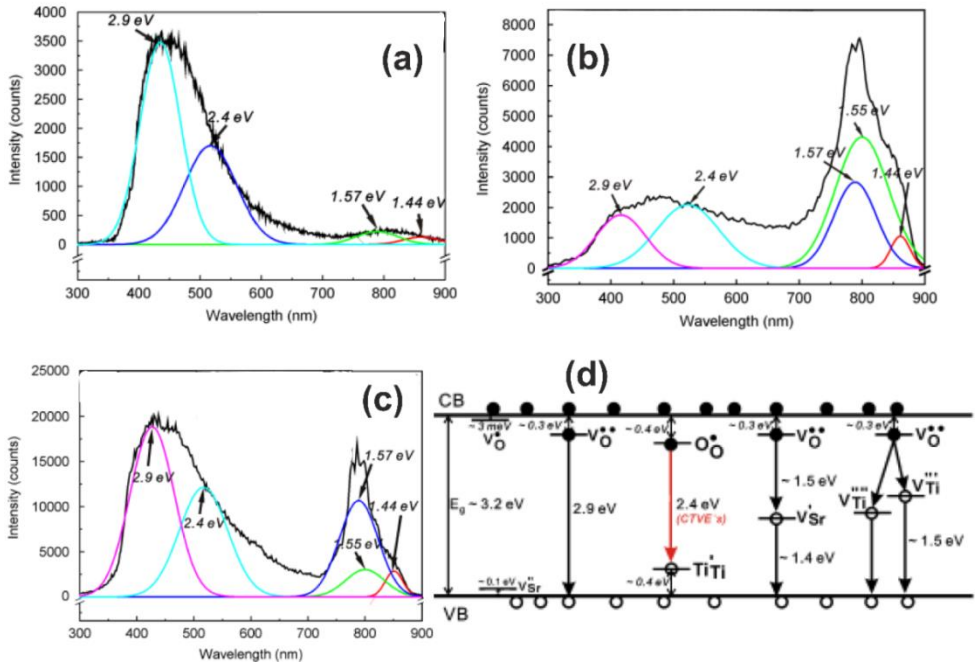

Fig. 3.20 Deconvolved CL spectra of (a) as received $SrTiO_3$ single crystal (b) $SrTiO_3$ ceramic annealed in air (c) annealed in low P_{O2}. (d) Schematic diagram of optical transitions between in-gap energy states associated with intrinsic defects. Adapted from ref. [279].

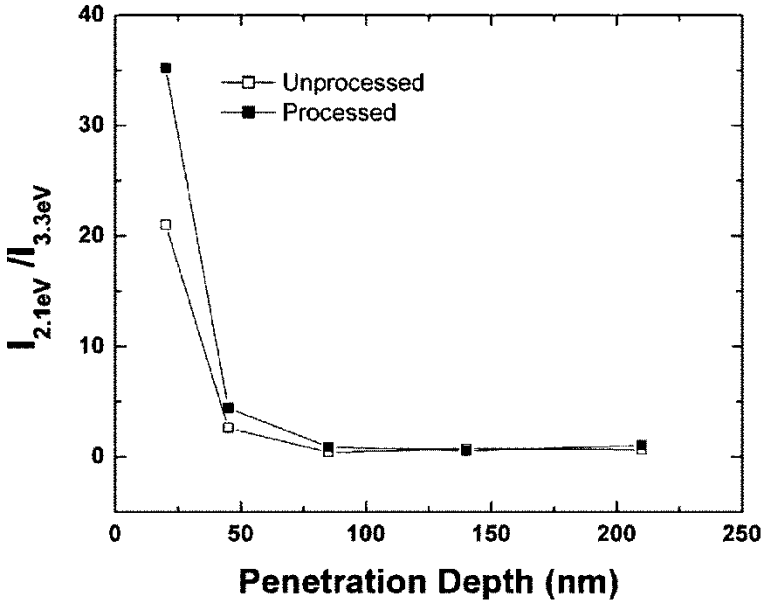

Fig. 3.21 Penetration depth dependence of the intensity ratio of the 2.1 eV peak to the 3.3 eV peak for unprocessed and processed $SrTiO_3$ single crystal. The figure is taken from ref [262].

The issue of defect distribution in the unprocessed and vacuum annealed $SrTiO_3$ single crystal was investigated by Zhang *et al.* [262]. Using DRCL, they found the dominant defects in $SrTiO_3$ were oxygen vacancies (V_O) and Ti interstitials (Ti_i), the

distribution of which showed a strong dependence on materials growth and processing conditions. CL spectra of both unprocessed and processed $SrTiO_3$ single crystals showed peaks around 3.3, 2.5 2.1 and 1.64 eV which were assigned to $SrTiO_3$ bandgap emission, V_O complexes and Ti_i respectively. Intensity analysis showed that V_O defects exist with relatively high concentration in the near surface region while Ti_i appeared for depths starting at 85 nm (140 nm) for the unprocessed (processed) single crystal. Thermal annealing in low P_{O2} increased the concentration of V_O, however, this effect was limited to 50-80 nm below the surface as shown in Fig.3.21, where the intensity ratio of the 2.1 eV peak to the 3.3 eV peak is plotted against penetration depth. The intensity ratio remained almost constant for depths beyond 85 nm indicating the presence of V_O mostly in the near surface region.

3.3.4 Summary and outlook

This section has outlined the defect induced optical and electrical properties in $SrTiO_3$ systems. Point defects such as impurity atoms or oxygen vacancies introduce paramagnetic properties which are investigated with the aid of ESR. The as-received single crystals are shown to have transition metals ions as impurities such as Fe, Cr, Mn. These ions have been shown to substitute for Ti ions with various oxidation states in the lattice and introduce in-gap states that are elucidated through Photo-ESR. Moreover, ESR investigation of the thermally reduced or Neutron irradiated $SrTiO_3$ single crystals revealed the formation of "off centred" Ti^{3+} centres. Illumination of the as-received single crystals with UV- light, however, demonstrated the Ti^{3+} centres that arise from the regular Ti sites as a result of charge transfer from the valence band to the conduction band. The untreated single crystals which are good insulators, become conductive when reduced. The presence of defects, such as dislocations, however 'heal out' during prolonged annealing which reduces the number of free carriers as shown by various reports. Reduction process also induces room temperature luminescence

behaviour due to the generation of defect states within the band gap of crystal. It is, therefore, highly desirable to investigate the nature of defect induced band gap states in order to optimize the optical and electrical transport behaviour in single crystal. In this context, electrical transport measurements combined with ESR and CL investigation could give valuable information.

3.4 Conclusion

This chapter reviews a diverse range of studies on the surface structures of $SrTiO_3$(111) surface, the influence of semiconducting surfaces on the growth of fullerenes, defect induced optical and electric properties of reduced $SrTiO_3$ single crystal. Based on these investigations, research work is proposed to improve our knowledge and understanding of defect driven properties of the surfaces and their utilization for the growth of functional materials. Moreover, optical and electrical properties of the $SrTiO_3$ single crystals could be optimized through controlled engineering of defects within the crystal. Various experiments are carried out in the following chapters to investigate these properties by employing powerful microscopy and spectroscopy techniques.

Chapter 4

Reconstructions on the $SrTiO_3$(111) surface

4.1 Background and overview

The polar (111) surface of $SrTiO_3$ has been shown to host a range of surface reconstructions, depending on the preparation conditions. For samples annealed in UHV at 850 °C, a surface with (√7×√7)R19.1° and (√131×√13)R13.9° coexisting reconstructions was obtained [88]. The $SrTiO_3$(111) surface sputtered with argon ions and annealed either in UHV or in an oxygen rich environment produced a family of n×n reconstructions [29]. Chiaramonti *et al.* [89] investigated the formation of 3×3, 6×6 and 9×9 surface reconstructions as a function of annealing time and oxygen partial pressure. Recently, Feng *et al.* [90] used STM to investigate the evolution between the 4×4, 5×5 and 6×6 reconstructions by depositing Ti and Sr. These reports exemplify the role of non-stoichiometry, surface chemistry and preparation procedures of different reconstructed surfaces. Nevertheless, these surfaces are often found to co-exist with each other and the quest for obtaining a particular surface reconstruction in a controlled manner remains a challenge. To tackle this enduring challenge, the evolution among various surface reconstructions is investigated in this chapter. This is done by simply varying the processing conditions such as annealing temperature, time and environment. These conditions also enable the formation of monophased surfaces that

could open a pathway for utilizing them in the growth of functional materials and engineering them for novel concepts of oxide based electronic devices.

Another important aspect of the $SrTiO_3$(111) surface is the theoretical investigations that are limited only to the 1×1 unit cell until now. In order to elucidate the structure of large unit cells theoretically, atomic resolution STM images of the surface reconstructions would be very helpful. Therefore, efforts have been made to obtain clear atomic resolution STM images of the surface reconstructions. These images will be used by Prof. Laurence Marks at the Northwestern University, USA, to solve the surface structures using DFT calculations as part of a long term collaboration with Prof. Martin Castell. The atomic resolution images of the reconstructed surfaces are also essential to identify the adsorption sites of guest molecules on the surface. Furthermore, a new 2×2 surface reconstruction is discovered in the present work that is an addition to the family of n×n reconstructions.

4.2 Experimental details

Single crystals of $SrTiO_3$(111) surfaces used for experiments in this chapter were supplied by PI-KEM, Ltd., UK, and were doped with 0.5 wt% Nb to facilitate the STM investigations. The sample preparation and STM imaging were carried out in the JSTM-4500XT and JSTM-4500S systems, both operating at a base pressure of 10^{-8} Pa. The as received samples were first degassed in UHV to remove carbon contamination prior to sample preparation. Atomically flat reconstructed surfaces were prepared by first sputtering the samples with Ar^+ ions and then annealing. Ar^+ ion sputtering was performed with a PSP Vacuum technology ion source ISIS3000 that is attached to the JSTM-4500XT and operates at an Ar pressure of 2×10^{-3} Pa. On the JSTM-4500S, a VG Microtech EX03 ion gun, operating at an argon pressure of 4.5×10^{-4} Pa, was used to sputter the samples. The sputtering beam energy was kept at 0.5 keV, and the duration

of sputtering varied from 6-20 minutes. The samples were then annealed in UHV or in an oxygen rich environment to prepare various reconstructed surfaces described in this chapter. The temperature of the samples was monitored with a Leeds and Northrup optical pyrometer. The sputtering time, annealing temperature and annealing environment are the critical factors that affect the formation of reconstructed surfaces. After annealing the samples, the surface structures were characterized with STM. All the STM images reported in this chapter were obtained in constant current mode.

4.3 The 5×5 and 6×6 coexisting reconstructions

The surface morphology of a $SrTiO_3$(111) sample that is sputtered with Ar^+ ions for 20 minutes and then annealed in UHV for 30 - 40 minutes at a temperature around 1050-1100 °C is shown in Fig. 4.1a. The figure shows the formation of terraces that are separated by step edges which align themselves with the <110> direction. The value of step heights, measured from the line profile of several STM images, is found to be 0.221 ± 0.02 nm. This corresponds to the d_{111} lattice parameter (0.225 nm) of $SrTiO_3$, consistent with previous investigations [29]. The terraces are covered with two different ordered domains which are labelled as 'α' and 'β'. Fig. 4.1b shows a magnified STM image of the domain 'α' with a surface unit cell indicated by a black diamond. This is a typical appearance of the surface usually observed in the STM images. The periodicity of this surface has a measured value of 2.77 ± 0.04 nm. This corresponds to approximately five times the bulk unit cell along the <111> direction (0.55 nm). An atomic resolution STM image of the 5×5 reconstruction taken from a flat terrace is shown in Fig. 4.1c, where the surface structure can be seen in more detail. A unit cell of the 5×5 reconstruction can be divided into two distinguishable triangular halves: one exhibits three bright dots at the centre and the other contains a dark centre. Fig. 4.1d shows an STM image of the domain 'β' at higher magnification. The periodicity

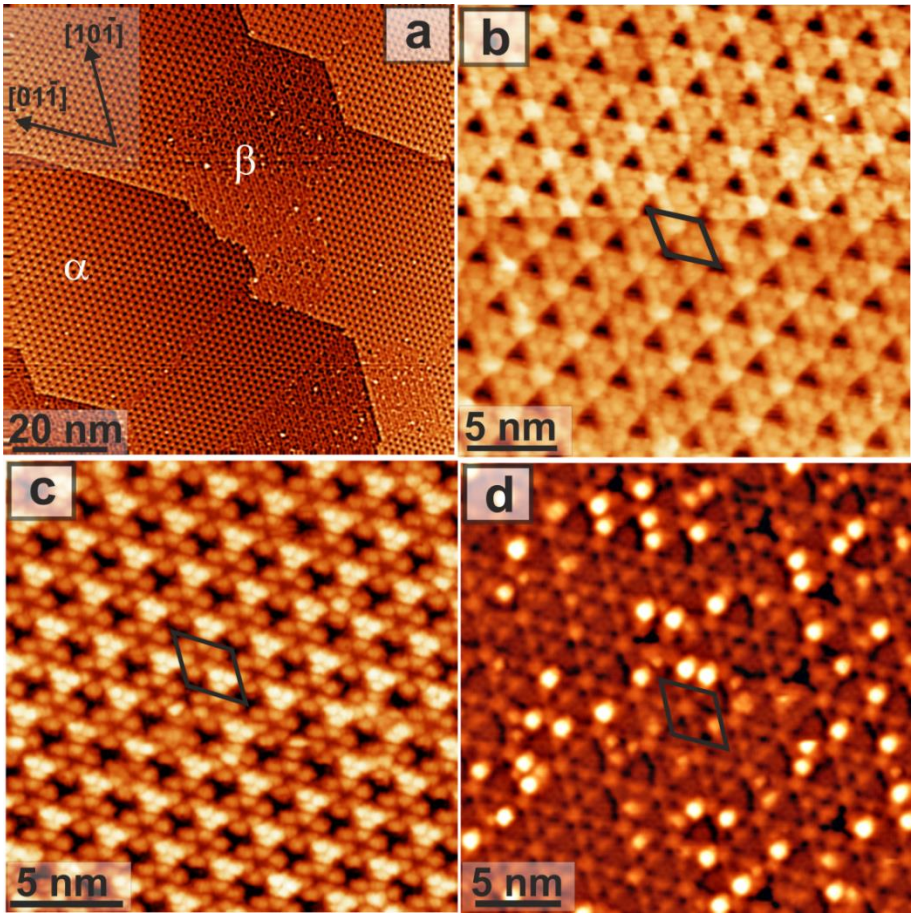

Fig. 4.1 STM images of the $SrTiO_3$(111) reconstructed surfaces following Ar^+ ion sputtering and UHV annealing. (a) The image shows terraces separated by the step edges. The terraces are made up of the 5×5 (indicated as 'α') and 6×6 (indicated as 'β') reconstructions. (b) STM image of the 5×5 reconstruction with a surface unit cell indicated. (c) Atomic resolution image of the (5×5) reconstruction. (d) STM image of the 6×6 reconstructed surface with a unit cell indicated in the figure. The imaging parameters are: (a) V_s = 2.02 V, I_t = 0.24 nA (b) V_s = 1.90 V, I_t = 0.26 nA, (c) V_s = 2.28 V, I_t = 0.26 nA, (d) V_s = 1.634 V, I_t = 0.28 nA.

measured from the STM images is equal 3.33 ± 0.06 nm, which corresponds to a 6×6 reconstructed surface. The unit cell of the 6×6 reconstruction is indicated in the figure by a black diamond. The image shows bright spots that are frequently observed on the 6×6 surface The origin of these bright spots is not understood yet but could be due to some unknown contaminations that are observed on this particular surface. These bright spots are previously reported to change positions and sometimes disappear at low applied bias [29].

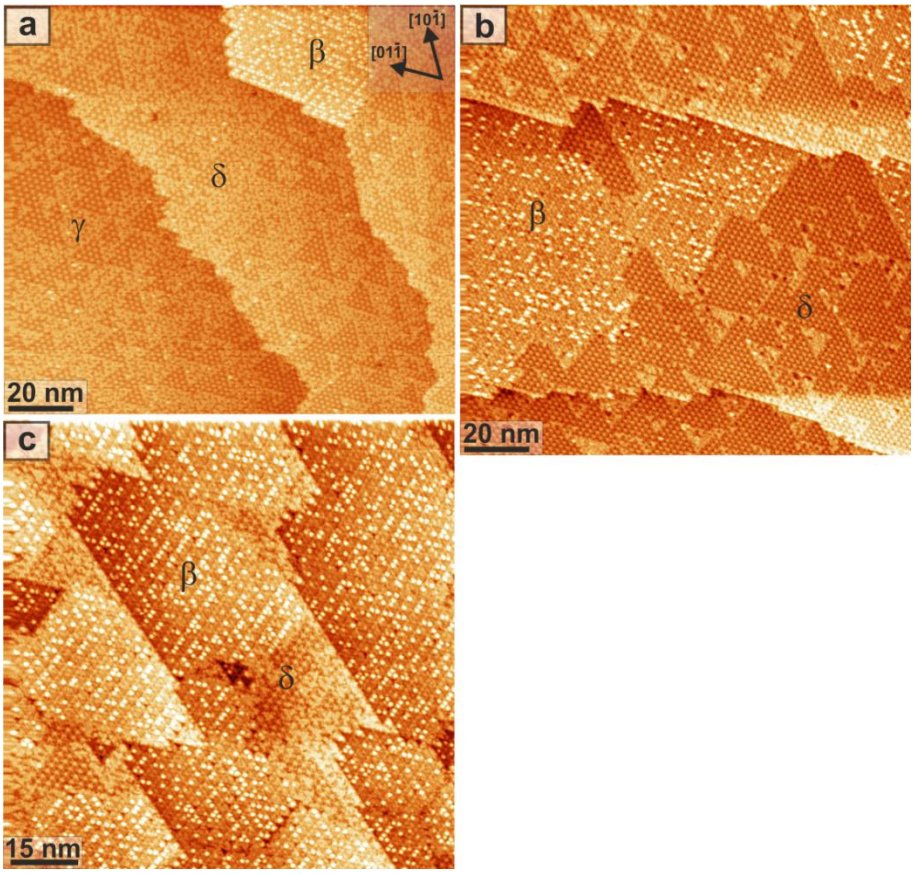

Fig. 4.2 Room temperature STM images showing the evolution of surface morphology of the $SrTiO_3$ (111) reconstructed surfaces following increased annealing temperatures and/or times. Three regions are labelled as β (6×6 reconstruction), γ (disordered region) and δ (4×4 reconstruction) in the images. The images show: (a) terraces are predominantly covered with disordered regions at 950 °C, (b) the δ regions are extended to a large area, while β regions are large and continuous without any disorder between them at 1050 °C, (c) the terraces are predominantly covered with β regions at 1100 °C. The imaging parameters are: (a) V_s = 1.85 V, I_t = 0.32 nA (b) V_s = 1.86, V, I_t = 0.32 nA (c) V_s = 1.841 V, I_t = 0.33 nA.

4.4 From the 6×6 to the 4×4 reconstruction

Fig. 4.2a shows an STM image of a $SrTiO_3$(111) surface that is sputtered with Ar^+ ions for 6 minutes and then UHV annealed at a temperature around 950 °C for 30 minutes. The surface is comprised of large terraces separated by step edges, oriented along the <110> crystallographic directions. Three regions are marked in the figure as 'β', 'γ' and 'δ'. The 'γ' regions cover most of the surface and appear disordered, whereas the 'δ' regions are ordered domains within small triangular patches. The third region labelled as 'β' is made up of well-ordered domains over a continuous region.

Annealing the sample with a surface similar to that shown in Fig. 4.2a at a temperature around 1000-1050 °C for 1 hour in UHV results in a surface morphology shown in Fig. 4.2b. The 'δ' regions are extended to a relatively large area, but the disordered regions (γ) are still evident in the image. The 'β' domain is ordered over a large area, and the periodicity of this region has a measured value corresponding to the 6×6 reconstruction. Similarly, the periodicity of the 'δ' domain corresponds to the 4×4 reconstruction.

Fig. 4.2c is an STM image taken after annealing a sample with a surface morphology similar to that observed in Fig. 4.2b at higher temperature. In this case, the sample was annealed at 1100 °C for one hour in UHV. The terraces are predominantly covered with the 6×6 domain ('β' regions), and only small regions containing 4×4 reconstruction ('δ' regions) are observed. This suggests that the periodicities are solely a function of annealing temperature. The atomic resolution STM of the 4×4 reconstruction taken from a terrace is presented in Fig. 4.3a. Two regions are labelled as 'A' and 'B' in the figure. These regions, at first glance, look very similar to one another. However, a closer inspection reveals that they are not exactly equal but instead they are non-superimposable mirror images of each other. This can be better understood by examining the unit cell marked by a white diamond in the magnified view of region 'A' in the inset of Fig. 4.3a. The unit cell of the reconstruction can be divided into two distinguishable halves, i.e., one contains three bright spots at the centre and the other exhibits three dots. When viewed along the $[01\bar{1}]$ direction, for example, a dot appears to the left of the bright spots in region 'A', whereas it appears to the right of bright spots in region 'B'. In other words, it can be seen that the three dots in a unit cell of 'A' region are rotated with respect to that of 'B' region. This is shown schematically in Fig. 4.3b, where the arrangement of three dots is shown. The bright spots are shown in yellow, while the three dots are represented by the red spheres. This makes the two

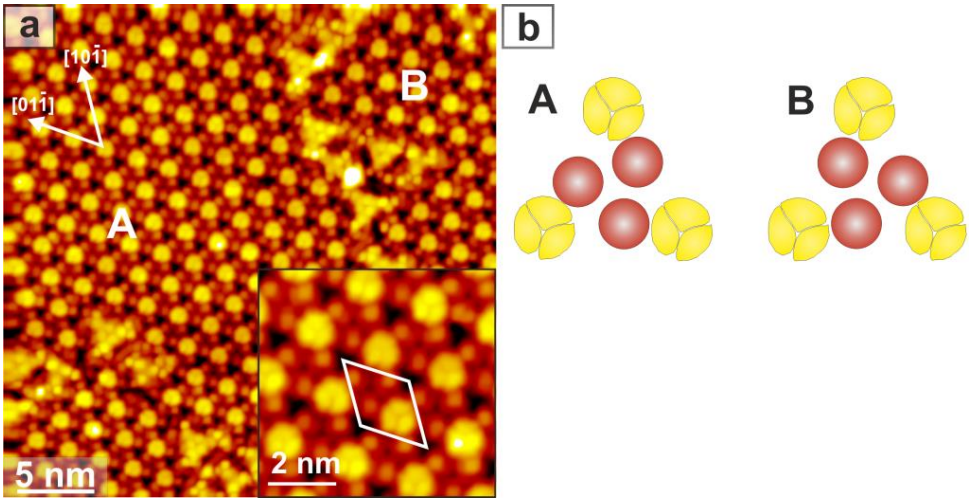

Fig. 4.3 (a) An atomic resolution STM image of the $SrTiO_3$(111)-4×4 reconstructed surface with two regions labelled as 'A' and 'B'. The inset displays a magnified view of region 'A'. The unit cell of 4×4 reconstruction is indicated by a white diamond in the inset and exhibits two inequivalent parts: one contains three bright spots and the other comprises of three dots. The ordered domain in 'A' region is non-superimposable image of that in domain 'B' region. (V_s = 2.0 V, I_t = 0.5 nA). (b) A schematic showing the arrangement of three dots. The red spheres represent the three dots, whereas the bright spots are shown in yellow.

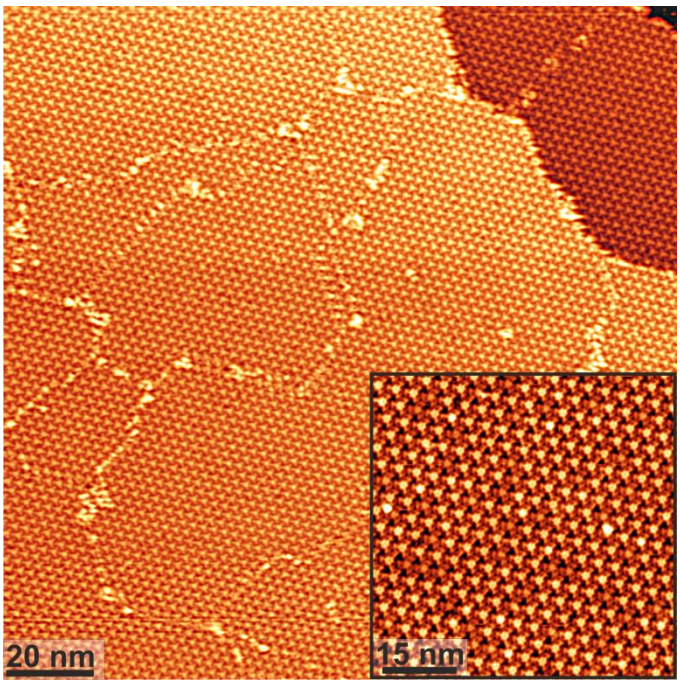

Fig. 4.4 A large STM image of the $SrTiO_3$(111)- 4×4 reconstructed surface (V_s = 2.00 V, I_t = 0.38 nA). The surface morphology shows white lines separating the ordered domains. The inset is a high resolution STM image of the 4×4 reconstruction taken from a flat terrace (V_s = 2.00 V, I_t = 0.365 nA).

regions non-superimposable mirror images of one another. Hence region ‘A’ and ‘B’ represents two separate chiral domains with unit cell consisting of a chiral portion and bright spots (non-chiral part).

The effects of annealing environment and temperature on the surface morphology of Ar^+ sputtered samples have also been investigated. The sample was first sputtered for 6 minutes and then annealed in the presence of an oxygen partial pressure (4.5×10^{-4} Pa O_2) at 950 °C for two hours. The resultant surface exhibits both the 4×4 and 6×6 reconstructions. However, when the annealing temperature is further increased to 1050 °C, the resultant surface shows a morphology presented in Fig. 4.4. Scanning across the sample shows no evidence of either the disordered regions or 6×6 reconstruction, which were observed in Fig. 4.2. Instead the surface is exclusively covered with the 4×4 reconstruction. This indicates that the 6×6 reconstruction is an oxygen deficient surface as compared to the 4×4 reconstruction. The surface morphology exhibits large flat terraces with a typical size greater than 300 nm. The terraces are covered with a network of white lines that form domain boundaries. A representative high resolution STM image of this surface is shown in the inset of Fig. 4.4.

4.5 From the 4×4 to the 3×3 reconstruction

A sample that is covered with a 4×4 reconstruction (as shown in Fig. 4.4) was further heated to a temperature around 1100 °C for 2 hours in 4.5×10^{-4} Pa O_2. The sample was then cooled and the surface structure was checked with STM at room temperature. The surface morphology is shown in Fig. 4.5a. The image consists of a number of terraces separated by step edges that are aligned along the <110> lattice directions. The terraces are covered with two coexisting regions. The surface structure of one ordered region (labelled as ‘δ’) corresponds to the 4×4 reconstruction (similar to

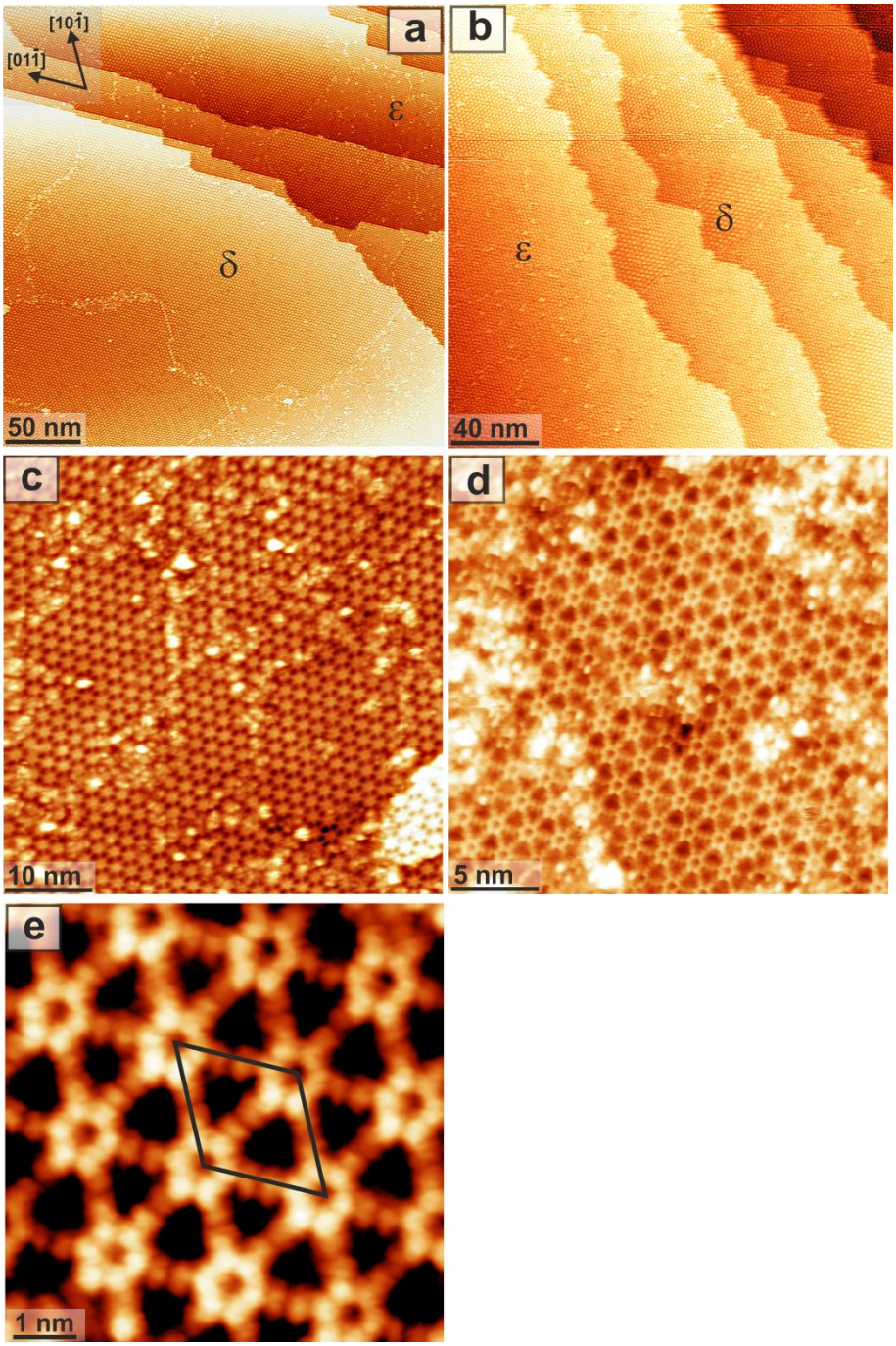

Fig. 4.5 STM images showing the evolution of surface morphology of the $SrTiO_3$(111) reconstructed surfaces. The samples were first sputtered with Ar^+ ions and then annealed in an oxygen rich environment. All the images were obtained at room temperature. The images show: (a) large area of the terraces is predominantly covered with the 4×4 reconstruction (δ), whereas small regions show the formation of the 3×3 reconstruction (ε) at 1100 °C, (b) the terraces are predominantly covered with the 3×3 reconstruction (ε) at 1150 °C, (c) a high resolution STM image of the 3×3 reconstruction, (d) an atomic resolution STM image of the 3×3 reconstruction. (e) A magnified STM image of the 3×3 reconstruction with a unit cell indicated. The imaging parameters are: (a) V_s = 1.998 V, I_t = 0.52, (b) V_s = 2.132 V, I_t = 0.365 nA, (c-e) V_s = 1.998 V, I_t = 0.375 nA.

that shown in Fig. 4.3), and covers a large area of the terraces. The domain boundaries are evident in the regions covered with the 4×4 reconstruction. The second ordered domain covers small regions of the terraces and is labelled as 'ε'. Fig. 4.5b is a large scale STM image taken after annealing the sample with a surface morphology similar to that shown in Fig. 4.5a. In this case, the sample was annealed at 1150 °C for 3 hours in the presence of an oxygen partial pressure (4.5×10^{-4} Pa O_2) and then cooled to room temperature. The terraces are now predominantly covered with the 'ε' domain, whilst only small regions of the 4×4 reconstruction ('δ') remain as evident in the image. This indicates that the evolution of the ordered structure ('ε' domain) from the 4×4 reconstruction is a function of annealing temperature and time. A room temperature STM image of the 'ε' domain is shown in Fig. 4.5c. The measured periodicity of this domain corresponds to the 3×3 reconstruction. The surface structure of the 3×3 reconstruction can be seen as a network of hexagonally arranged bright spots, with each spot connect to adjacent one through a bright line. Fig. 4.5d is an atomic resolution STM image taken from a flat terrace. Although the disordered regions are present on the surface, a hexagonal lattice of the 3×3 reconstruction can be clearly seen. A magnified STM image of the 3×3 lattice is shown in Fig. 4.5e. The contrast of the image is adjusted in order to show greater detail of the surface. The unit cell of the 3×3 reconstruction is indicated by a black diamond in the figure. Here, the bright spots can be clearly resolved. Each bright spot is further comprised of six dots and exhibits a dark centre. The network of bright spots is connected through a line comprised of two dots.

4.6 From the 3×3 to the 2×2 reconstruction

A sample that is covered with a 3×3 reconstruction similar to that observed in Fig. 4.5b was further heated to a temperature around 1200°C for 5 hours in 6.0×10^{-4} Pa O_2. The sample was then cooled to room temperature, and the surface structure was

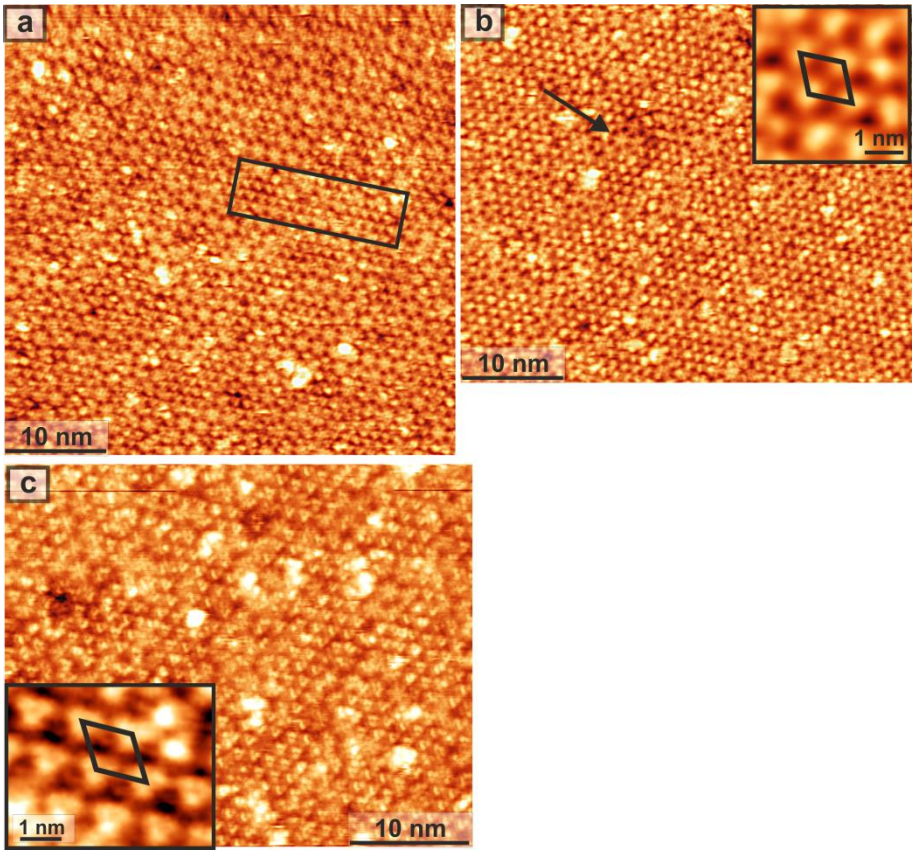

Fig. 4.6 STM images showing the evolution of surface morphology of the $SrTiO_3$(111) reconstructed surfaces as a functions of annealing temperature and time. All the images were obtained at room temperature. The images show: (a) the majority the surface is covered with the 3×3 reconstruction, whereas small regions show the formation of the 2×2 reconstruction (as indicated by the rectangle) at 1200 °C, (b) the surface is largely covered with the 2×2 reconstruction at 1280 °C, (c) a high resolution STM image of the 2×2 reconstruction. The inset is a magnified image with a unit cell indicated. The imaging parameters are: (a) V_s = 2.2 V, I_t = 0.402 nA (b) V_s = 1.978 V, I_t = 0.38 nA (c) V_s = 1.941 V, I_t = 0.375 nA.

checked with STM. Fig. 4.6a is a representative image of this surface taken from a flat terrace. Regions of the surface can be seen that have different periodic arrangements. The majority of the surface is covered with the 3×3 reconstruction, but small regions show a new structure that exhibits a short range order as highlighted by a rectangle. The periodicity of this structure has a measured value equal to 1.01 ± 0.13 nm, which corresponds to the 2×2 reconstruction. It is important to note that this reconstruction is not the same as the TiO nanophase surface with a 2×2 unit cell, reported by Russell and Castell [29]. The TiO(111)-(2×2) surface was formed after annealing the sample at 1400 °C in UHV, whilst the 2×2 reconstruction presented in Fig. 4.6 evolved after

annealing the sample in an oxygen rich environment and has not been reported previously. Moreover, the TiO(111)-(2×2) reconstruction imaged with both positive and negative applied bias due to the conductive nature of the surface. However, the 2×2 reconstruction in the present case can only be imaged at positive bias, typically above 2.0 V.

Fig. 4.6b is an STM image taken after annealing a sample covered with a surface similar to that shown in Fig. 4.6a at 1280 °C for 5 hours in 6.0×10^{-4} Pa O_2. The resultant surface is predominantly covered with the 2×2 reconstruction, and small regions with the 3×3 reconstruction are still evident on the surface as indicated by an arrow. Additionally, the surface also shows a disorder in some regions. The 2×2 reconstruction can be seen as a network of bright spots as shown in the inset of Fig. 4.6b. A high resolution STM image of the 2×2 reconstructed surface taken from a flat terrace is shown in Fig. 4.6c. The surface unit cell is indicated by a black diamond. The bright spots appear to consist of three dots as shown in the inset of Fig. 4.6c.

4.7 Discussion

The $SrTiO_3$(111) surface accommodates a wide range of non-stoichiometries, and results in a number of surface reconstructions that depends on the sample preparation [29, 88, 89]. However, it is difficult to obtain a particular reconstructed surface in a reproducible and controlled manner. The work presented in this chapter is focused on a systematic study of the evolution and then progression of monophase surface reconstructions on $SrTiO_3$(111) surface by varying the annealing temperature, time and annealing environment.

Sputtering the sample surface with Ar^+ ions introduces structural defects such as oxygen vacancies that affect the stoichiometry of the surface and near surface region [1]. The degree of disorder depends on the sputtering energy and time [1, 280]. Upon

heating the sample, the top surface layers of the sample become increasingly ordered and thus results in a reconstructed surface. Samples that are sputtered with Ar^+ ions for 20 minutes and subsequently annealed at around 1050 °C in UHV for 30 minutes exhibit a surface morphology which has predominant phase with 5×5 reconstruction along with small domains of 6×6 periodicity, and is in agreement with the work reported by Russell and Castell [29].

Sputtering the sample for a short time (6 minutes) and subsequent UHV annealing at 950 °C for 30 minutes results in the formation of coexisting 4×4 and 6×6 reconstructions (Fig. 4.2a). This coexistence has previously been reported by Russell and Castell, and suggests that both the reconstructions are of similar composition and surface energy. The 6×6 reconstruction is continuous over larger areas of the surface, whereas the areas covered with the 4×4 reconstruction are smaller and separated by the disordered regions. However, STM images obtained from a sample after prolonged annealing show the 4×4 reconstruction extended over larger areas of the surface (Fig. 4.2b). On further annealing the sample at a temperature of 1100 °C in UHV, the surface is predominantly covered with the 6×6 reconstruction. However, annealing a sputtered sample at 1050 °C in oxygen partial pressure leads to an interesting observation of a monophased 4×4 reconstruction, with no indication of the 6×6 reconstruction (Fig.4.4). The 4×4 reconstruction has not been achieved as a monophase until now. This suggests that 6×6 reconstruction is an oxygen depleted phase as compared to the 4×4 reconstruction, and adds further support to the previous AES investigations [29].

The formation of the 4×4 reconstruction in UHV could be understood in the context of bulk-assisted re-oxidation [281]. The oxygen concentration gradient between the sputtered surface and bulk of the $SrTiO_3$ sample act as a driving force for the process of self-diffusion exchange with the bulk and provides oxygen which leads to the formation of the 4×4 periodicity. Prolonged annealing, however, slows down the

process of self-diffusion. At this point continued annealing in UHV is most likely destabilizing the 4×4 phase as the concentration of oxygen required for this phase is reducing. On the other hand the 6×6 reconstruction, which is more oxygen deficient phase as compared to 4×4, is extending over larger region with prolonged annealing.

The evolution of 3×3 reconstruction from a surface with 4×4 periodicity is achieved by further annealing of sample at 1100 °C in an oxygen environment as shown in Fig. 4.5. The 3×3 reconstruction is seen to extend over a large area of the surface upon increasing the annealing temperature and time as evident in the STM image of Fig. 4.5b. This suggests that the 3×3 reconstruction is a more oxygen rich phase than the 4×4 reconstruction and can only be obtained by annealing a sample in the presence of an oxygen partial pressure, consistent with the work reported by Russell and Castell [29]. The final surface that is a new addition to the n×n family of reconstructions is the 2×2 reconstruction. The surface is formed by further annealing a sample covered with the 3×3 reconstruction in a more oxygen rich environment. STM images show a coexistence of both the 2×2 and 3×3 reconstructions, suggesting that both the reconstructions have a similar composition and surface energies. The 2×2 reconstructed surface is achieved over a large area after annealing the sample at 1280 °C for 5 hours (Fig.4.6b). This indicates that the 2×2 reconstruction is a more oxygen enriched phase as compared to the 3×3 reconstruction. After the addition of the 2×2 reconstruction to the n×n family, the progression from oxygen depleted to oxygen-enriched reported by Russell and Castell then becomes:

Oxygen depleted, 5×5 < 6×6 < 4×4 < 3×3 < 2×2, Oxygen enriched

The underlying mechanism for the formation of these reconstructions could be understood in the context of thermodynamic stability. The creation of a given reconstructed surface requires particular surface treatment i.e., a combination of optimum sputtering and annealing to minimize the surface free energy and become

thermodynamically stable. Sputtering the sample with Ar^+ ions increases the mobility of Ti ions, which diffuse towards the surface upon heat treatment thereby giving rise to Ti enriched surfaces [29, 282]. By varying the annealing conditions, the chemical potential of the surface species changes and consequently the surface undergoes a transition from one ordered phase to another in order to lower its surface free energy [283].

In the present study, plausible structural models for atomic scale structures are limited. The average separation between the nearest neighbour bright spots measured from the STM images of the 5×5 (Fig. 4.1c) and 4×4 reconstructions (Fig. 4.3) is 0.7 nm, which is greater than the inter-atomic distance of Ti ions. This indicates that each bright spot is possibly composed of a cluster of atoms, and the electron density has contribution from multiple atoms. This was observed for the $SrTiO_3$(001) surface, where structural models established through DFT calculations revealed that each spot observed in the STM images is not a truly atomic feature [46]. In contrast, the spots observed in the STM images of the 3×3 and 2×2 reconstructions (Fig. 4.5d and 4.6c respectively) are 0.3 nm apart, which is comparable to the Ti-Ti interatomic distance in titanium dioxide [284, 285] and thus each dot observed in the STM image could be attributed to an individual Ti atom.

STM is a valuable technique for obtaining real space images of a conductive surface at the atomic level, but its inability to provide reliable chemical identification of surface species remains an unresolved, fundamental problem. The STM is sensitive to the electronic structure in the vicinity of the Fermi level, so cannot unequivocally reflect the chemical nature of particular atomic species at the surface. Russell and Castell elucidated the surface chemistry of reconstructed $SrTiO_3$(111) surfaces with the aid of AES. They found that the surface phases are TiO_x rich with varying oxygen stoichiometry that depends on the preparation conditions, including as Ar^+ ion

sputtering, annealing temperature and environment. However, the chemical composition of a surface obtained through AES is spatially averaged, so surfaces with multiple phases complicate any quantitative estimate of stoichiometry. Due to the complex nature of the perovskite oxides, additional experimental methods combined with theoretical calculations should be implemented to render the surface structure of the family of n×n reconstructions. In this regard, recent studies revealed that atomic force microscopy (AFM) has the analytical capability to identify the individual atoms on the surface [286, 287]. Similarly, transmission electron diffraction (TED) or scanning transmission electron microscopy (STEM) can be combined with spectroscopic techniques such as electron energy loss spectroscopy (EELS) and energy dispersive X-ray spectroscopy (EDX) for viable interpretation of the reconstructed surfaces [288-290]. Additionally, theoretical methods such as DFT calculations should be implemented for thorough determination of the surface structures and the results can be compared with the experimental images to provide viable structural models.

4.8 Summary

This chapter has addressed a systematic study of the evolution among the family of n×n surface reconstructions (n = 2, 3, 4, 5, 6) by varying the Ar^+ ion sputtering time, annealing temperature, time and environment. Surfaces predominantly covered with one type of surface reconstruction and even with monophased reconstruction are achieved by adjusting the above mentioned parameters which is an important step towards the realization of these distinct surfaces for the epitaxial growth of functional materials.

Longer sputtering times followed by UHV annealing lead to the formation of 5×5 reconstruction, whereas comparatively short sputtering and subsequent annealing results in a surface with coexistent 4×4 and 6×6 reconstructions. Further annealing in

UHV at higher temperature produce a surface solely covered with the 6×6 reconstruction. A monophased 4×4 reconstruction is formed after annealing the sputtered sample in oxygen-rich conditions. The evolution of the 3×3 from 4×4 reconstruction, and that of 2×2 from 3×3 reconstruction has also been investigated. Moreover, atomic resolution STM images of the reconstructed surfaces are obtained which will be compared with STM image simulations obtained through DFT calculations to solve the surface structures, and to identify the specific adsorption sites of guest molecules in the investigation of surface reactivity of the reconstructed surfaces. The detailed study of the latter is presented in the next chapters.

Chapter 5

Magic clusters of fullerenes on the $SrTiO_3$(111)-5×5 reconstruction

5.1 Background and overview

The $SrTiO_3$(001) surface has been shown to host a rich variety of reconstructions and nanostructured surfaces by varying the sample preparation procedures [27, 28, 291]. Due to their unique chemical and topographic nature, the nanostructured $SrTiO_3$(001) surfaces have been demonstrated to arrange fullerene molecules into particular configurations corresponding to the underlying surface [30, 169-171]. There are few reports on the study of $SrTiO_3$(111) surface with a special focus on the link between surface preparation methods and its properties [29, 88]. In order to exploit further properties of the $SrTiO_3$(111) surface, Russell investigated the growth of fullerene molecules [55]. However, this work was only limited to the $SrTiO_3$(111)-5×5 reconstruction and involved heat treatment of the substrate surface during deposition for the production of close-packed islands. A detailed investigation is required to explore how the non-stoichiometric surface structures could be made functionally useful for device applications.

The study presented in this chapter is an extension of the work reported in the previous chapter, where the evolution of various surface reconstructions was investigated as a function of surface preparation conditions. Here, the surface reactivity of $SrTiO_3$(111)-5×5 and 6×6 reconstructed surfaces is investigated through deposition of fullerenes, namely C_{70} and C_{60}. The 5×5 reconstruction has been shown to be the most oxygen deficient phase among the family of n×n surfaces [29], and hence is an ideal platform to see the effects of non-stoichiometries on its reactivity. Fullerenes are used as prototype molecules which are capable of providing valuable information about the molecule interactions and are also attractive from the point of view of their potential applications in molecular based devices. The interaction of these molecules with the $SrTiO_3$(111) reconstructed surface should provide an insight into the surface reactivity. At the same time, these reconstructions will be explored as a template for the ordering of fullerenes.

5.2 Experimental details

In this chapter, results on the interaction of reconstructed $SrTiO_3$(111) surfaces with fullerenes are presented and discussed. These studies were performed to explore how the non-stoichiometric surfaces structure influence the growth of fullerenes. The experiments were performed on Nb doped epi-polished $SrTiO_3$(111) single crystals. The JEOL-4500XT system was used for the sample preparation and STM imaging. The samples were prepared according the procedures mention in Chapter 4. After achieving the atomically flat reconstructed surfaces, fullerenes were deposited and surfaces covered with molecules were characterized with STM. Fullerenes C_{60} and C_{70}, with high purity (> 99.9%), were obtained from Dr Kyriakos Porfyrakis at the Department of Materials, University of Oxford. Both C_{60} and C_{70} fullerenes were introduced into separate Knudsen Cells (K-cells). The K-cells were then mounted to the STM chamber of JEOL-4500XT, and outgassed prior to the deposition of molecules. The K-cells were

then heated to temperatures around 290 °C and 370 °C for the deposition of C_{60} and C_{70}, respectively. Deposition was performed with the $SrTiO_3$ samples held at room temperature.

5.3 Interaction of 5×5 and 6×6 coexisting surfaces with fullerenes

Fig. 5.1a is an STM image following evaporation of C_{70} fullerenes on the 5×5 and 6×6 co-existing surfaces held at room temperature. The surface was formed by sputtering the sample for 20 minutes and then annealing in UHV at 1100 °C for 30 minutes (c.f. chapter 4). The image consists of two terraces separated by a step edge. The left terrace is covered with the 5×5 reconstruction, whereas the right terrace is made up of the 6×6 reconstructed surface. C_{70} produced large two dimensional islands on the 6×6 reconstruction at submonolayer coverage. The formation of large islands indicates that fullerenes are able to migrate on the surface at room temperature. The height of fullerene islands formed on the 6×6 reconstruction is found to be typically of the order of ~1 nm. The orientations of these islands appears to be random and not influenced by the 6×6 reconstructed surface, suggesting the relationship between the C_{70} overlayer and template surface is not epitaxial. The most striking features are observed on the 5×5 reconstruction, where individual molecules and clusters are evident in the image. This is highly unusual behaviour which can be contrasted to that observed on the 6×6 reconstruction and previous STM studies of fullerenes on surfaces, where fullerenes usually produce close-packed islands with an hexagonal arrangement [101]. The STM image of Fig.5.1b illustrates the deposition of C_{60} on a 5×5 and 6×6 co-existing surface at room temperature. Similar to C_{70}, C_{60} molecules also produce close-packed islands on the 6×6 reconstruction. However, clusters and individual molecules are observed on the 5×5 reconstructed surface. A detailed study of the interaction of 5×5 reconstruction with both C_{60} and C_{70} fullerenes is described in the following sections.

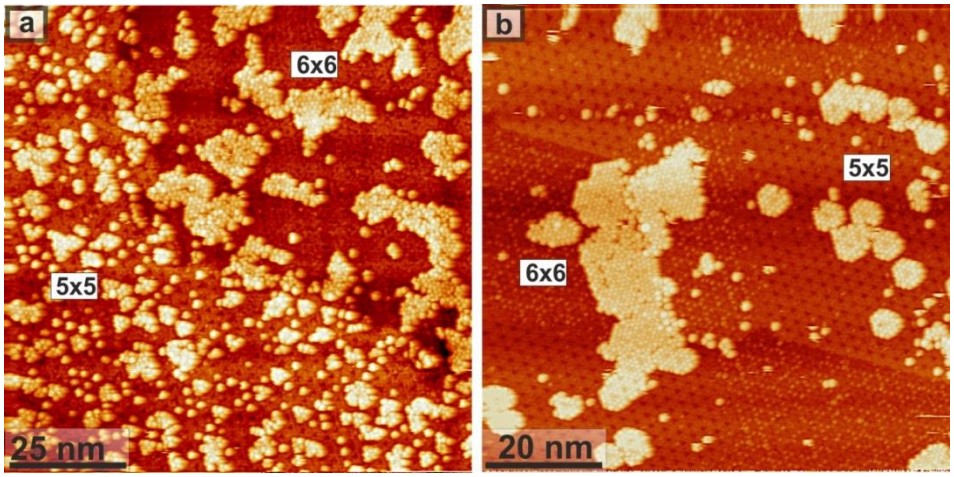

Fig. 5.1 Fullerene molecules deposited at room temperature on a surface with 5×5 and 6×6 coexisting reconstructions. (a) C_{70} produces close-packed islands on the 6×6 reconstruction, whereas individual molecules and clusters are evident on the 5×5 reconstruction (V_s = 1.52 V, I_t = 0.26 nA). (b) STM image of C_{60} fullerenes deposited on the 5×5 and 6×6 coexisting reconstructions. The molecules produce large islands on the 6×6 reconstruction, and smaller clusters on the 5×5 reconstruction (V_s = 1.90 V, I_t = 0.15 nA).

5.4 Interaction of the $SrTiO_3$(111)- 5×5 reconstruction with fullerenes

5.4.1 Adsorption of C_{70}

Fig. 5.2a shows an atomic resolution STM image of 5×5 reconstructed surface with a unit cell indicated by a black diamond and was previously shown in Fig. 4.1c. A unit cell of the 5×5 reconstruction can be divided into two distinguishable triangular parts: one part exhibits three bright dots at the centre and the other contains a dark centre. A schematic representation of the unit cell is shown in Fig. 5.2b. The measured corrugation height of the bright spots with respect to the dark spots is 1.0 ± 0.1 Å (the error bar given is the standard deviation of the measurements). The 5×5 reconstruction contains triangular depressions with a measured averaged depth of 1.9 ± 0.3 Å. In the following text these are referred as 'triangular holes'.

Following initial deposition, when C_{70} molecules were deposited for 5 minutes, the majority of the C_{70} molecules are observed as isolated bright spherical protrusions with no tendency to form close-packed islands, with the exception of a few apparent

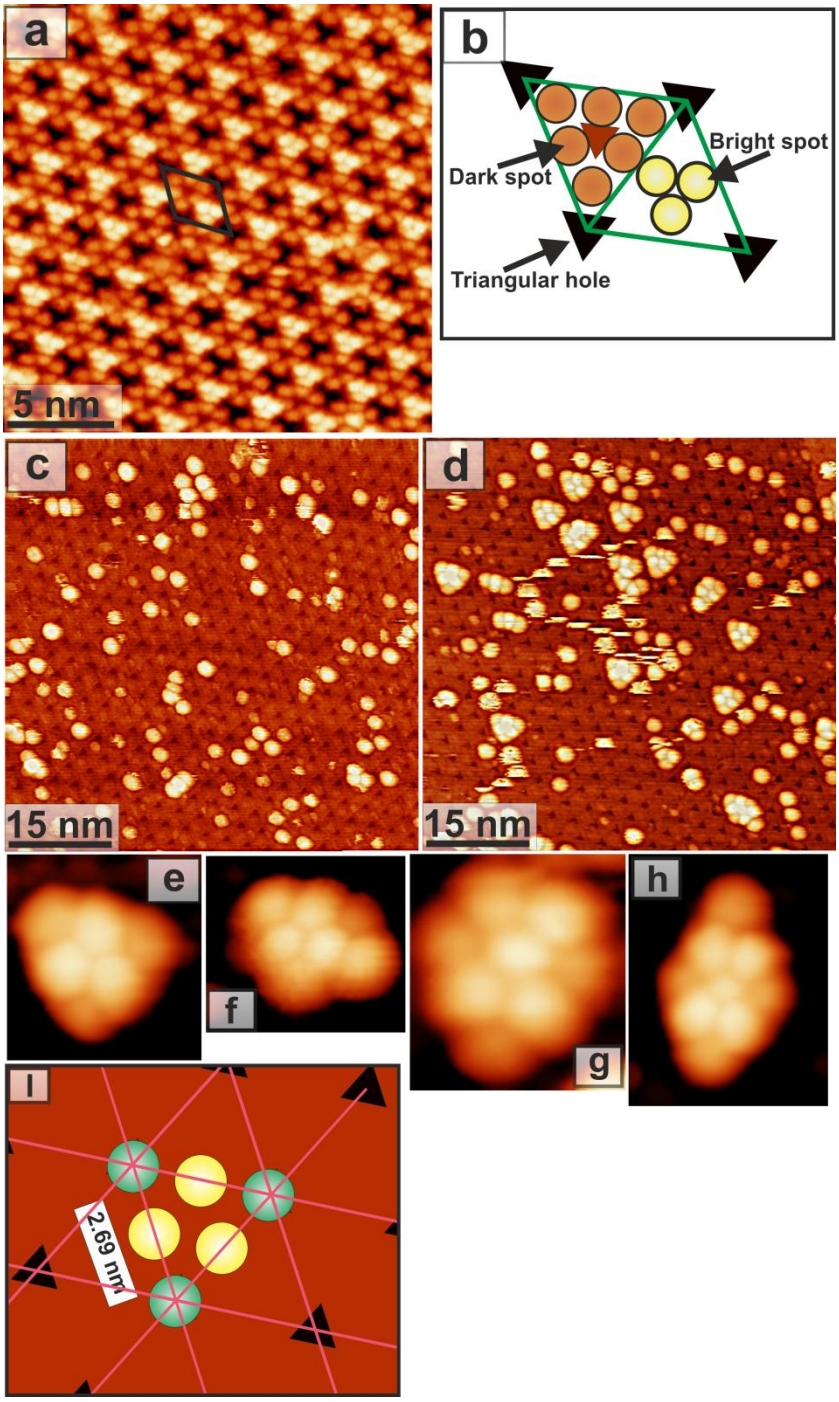

Fig. 5.2 Interaction of the $SrTiO_3$(111)-5×5 reconstructed surface with fullerene C_{70}. (a) STM image of the 5×5 reconstruction (V_s = 2.28 V, I_t = 0.26 nA). (b) A schematic representation of a 5×5 unit cell.(c) STM image of C_{70} deposited for 5 minutes. The majority of the molecules adsorb individually on the triangular holes of the unit cell (V_s = 2.0 V, I_t = 0.20 nA). (d) STM image taken after depositing molecules for 10 minutes. The image shows C_{70} adsorbed individually and arranged into various magic clusters (V_s = 2.0 V, I_t = 0.20 nA). (e) - (h) Magnified images of the 6, 7, 8 and 9-fold clusters. The geometrical shape of a 6-fold cluster is triangular, while the 9-fold cluster possesses the shape of a parallelogram. (i) A geometrical model of the 6-fold cluster.

small clusters consisting of two or three molecules. This is shown in the room temperature STM image of Fig. 5.2c. The observation of separated individual molecules indicates a strong interaction between C_{70} and a highly preferential adsorption site on the 5×5 template surface that diminishes the migration of molecules from approaching each other to form close-packed islands. There is no preference for step edges as adsorption sites for the fullerenes. By careful inspection of several STM images, the triangular hole of the 5×5 unit cell is found to be the highly preferential adsorption site for the fullerenes. This indicates that the triangular hole is a highly reactive site to trap individual fullerenes when they arrive at the surface. The apparent height of the adsorbed molecules measured with respect to the substrate is 8.2 ± 0.7 Å, which is smaller than the van der Waals diameter of C_{70}. Since the measured depth the triangular hole of a 5×5 unit cell is ~2 Å, this demonstrates that C_{70} fullerenes sink deep into the hole. The lateral diameter of the individual C_{70} molecules, measured from the line profile of STM images, is found to be ~20 Å. The size of individual molecules appearing large in the STM images can be attributed to the tip convolution effect.

A further increase of the C_{70} coverage to 10 minutes results not only in the confinement of more individual fullerenes into the triangular holes of unit cell, but also produces various regular shaped clusters. This is shown in the STM image of Fig. 5.2d, where C_{70} molecules rearrange themselves into various clusters. The observed clusters are composed of a minimum of two to maximum of nine molecules (in the following text these clusters are referred as n-fold clusters, where n is the number of C_{70} molecules in a cluster). The most frequently observed cluster is the 6-fold cluster that exhibits a well-defined triangular shape with three-fold rotational symmetry. The cluster is comprised of six C_{70} molecules, where each molecule at the corner and centre exhibits two and four nearest neighbours, respectively. Within each 6-fold cluster, the central three molecules appear brighter than the corner molecules in STM images. The measured apparent height difference between the bright and dim molecules is 1.91 ±

0.22 Å on average. This is consistent with the corrugation measured for the bare template surface, indicating the apparent height difference between the dim and molecules can be attributed to surface topography, where the corner molecules of the 6-fold cluster are pinned in the triangular holes of the unit cell and the bright molecules reside atop the surface. The separation between two dim molecules in the 6-fold cluster had a measured value of 2.69 ± 0.11 nm. This separation is comparable to the unit cell periodicity of the $SrTiO_3$ (111)-5×5 unit cell, indicating an epitaxial relationship of the 6-fold cluster relative to the template substrate. Magnified STM images of the 6, 7, 8 and 9-fold clusters are shown in Fig. 5.2e-5.2h. It is likely that the 7, 8 and 9-fold clusters have evolved from a 6-fold cluster by the addition of C_{70} molecules. The 9-fold cluster has the shape of a parallelogram with molecules at the corner appearing dim as compared to the central molecules. These clusters are less abundant on the template surface as compared to the 6-fold cluster, indicating the substrate has a dominant role in stabilizing the 6-fold cluster. The results are analysed by means of a simple geometrical model as illustrated in Fig. 5.2i. The green spheres represent C_{70} molecules occupying the triangular holes while the yellow ones correspond to molecules residing atop the surface.

A representative large scale STM image after the deposition of C_{70} molecules for 25 minutes is shown in Fig. 5.3a. The sample surface is covered with individual molecules, indicating that the majority of the available preferred adsorption sites are occupied by C_{70} molecules. The image also features small irregular islands of molecules. It is more likely that they could be formed after occupying majority of the available adsorption sites i.e. the triangular hole of the 5×5 unit cell. This is shown in the STM image of Fig. 5.3b, where the islands can be seen. Apart from the individual molecules, the 6-fold clusters are also evident in the figure.

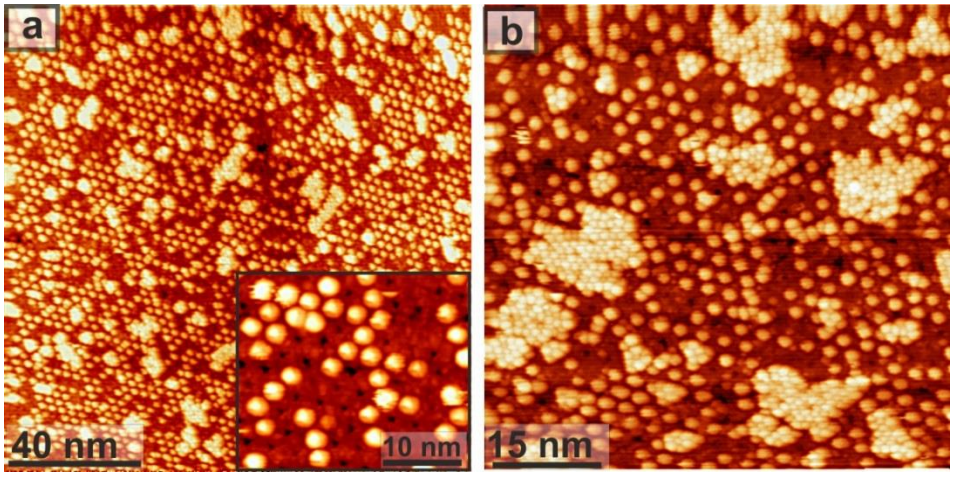

Fig. 5.3 STM images of the 5×5 surface after the deposition of C_{70} molecules for 25 minutes. (a) A large scale STM image showing the individual adsorption of C_{70} molecules on the 5×5 reconstructed surface. The image also shows the formation of islands (V_s = 2.0 V, I_t = 0.20 nA). The inset is a magnified STM image that shows individual molecules adsorbed at the corner hole of the 5×5 unit cell. (b) A high resolution STM image showing the individual molecule adsorption and island formation (V_s = 2.0 V, I_t = 0.18 nA).

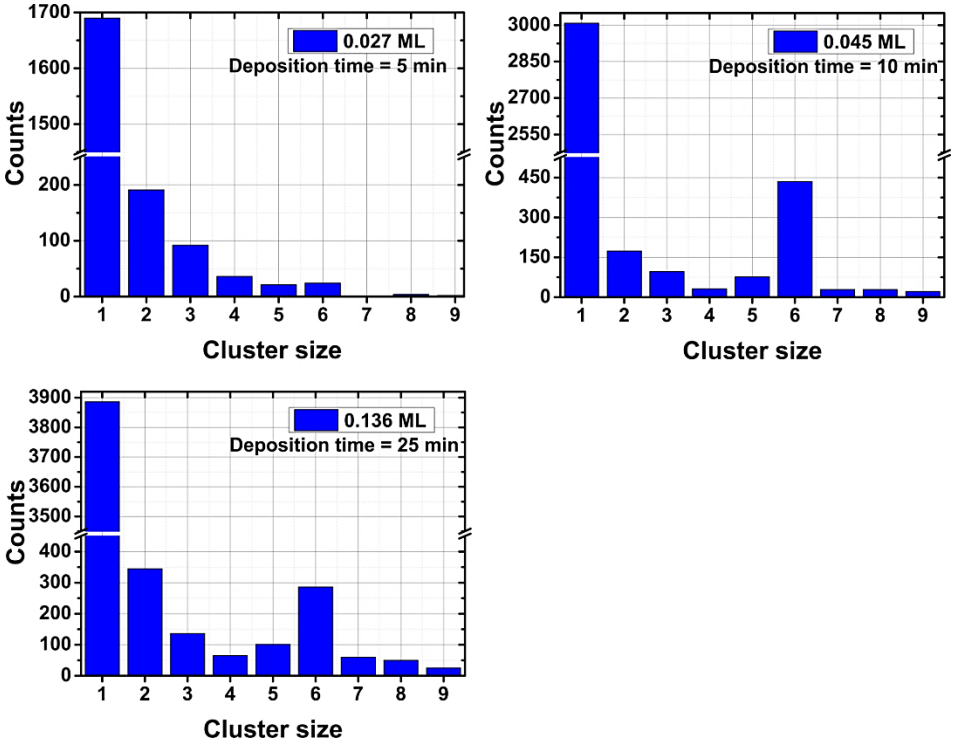

Fig. 5.4 Histograms of the population of individual C_{70} molecules and magic clusters at 5, 10 and 25 minutes of deposition time. Statistical analysis for each deposition was obtained from several STM images, where the number of individual molecules and clusters were counted. The x-axis represents the number of molecules in a cluster. The y-axis represents the observed population of each cluster in the STM images. The corresponding coverage for each deposition time is also indicated.

Fig. 5.4 presents the statistical data of molecules deposited for 5, 10 and 25 minutes. The data for each deposition time is taken from randomly chosen STM images, where the number of individually adsorbed molecules and n-fold clusters were counted in each image. The statistical analysis performed on various images for each deposition time was then plotted as histograms to investigate the distribution of individual molecules and n-fold clusters. The coverage of fullerenes for each deposition time is determined by counting the total number of molecules, including the islands, in the STM images. Here, 1ML coverage of fullerenes on the 5×5 reconstructed surface is defined as 1.15 molecules per 1 nm^2. It can be seen from Fig. 5.4 that the majority of the molecules are adsorbed individually, and only few molecules produced the 6-fold clusters. The number of individual molecules increases as the coverage increases. This indicates that the corner hole of the unit cell is a highly reactive site for the molecules to adsorb on to. On the other hand, the 6-fold initially increased with C_{70} coverage and then decreased at higher deposition (25 minutes). This decrease could be attributed to the formation of large irregular shaped islands at high coverage that are frequently observed on the surface in STM images.

5.4.2 Adsorption of C_{60}

The STM image of Fig. 5.5a illustrates the interaction of the 5×5 reconstructed surface with C_{60}. The deposition was performed for 5 minutes at room temperature. C_{60} molecules adsorb individually as well as arrange themselves into various types of clusters on the 5×5 reconstructed surface. The observed clusters are composed of a minimum of two to maximum of 30 molecules. The step edges are not favoured as nucleation sites for the fullerenes to adsorb to. Instead, individual molecules and clusters were typically observed in the middle of terraces. The most abundantly observed clusters are the 6-fold and 27-fold with well-defined shapes. The image in

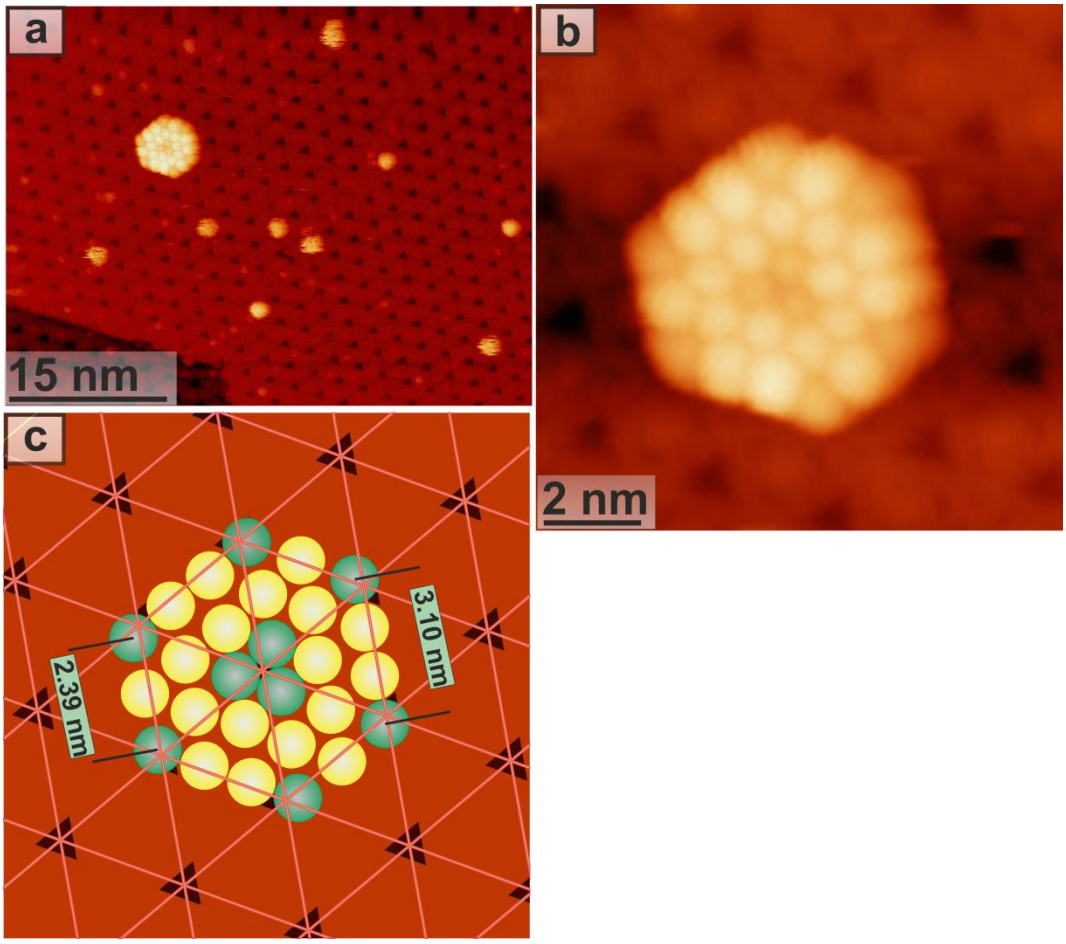

Fig. 5.5 STM images demonstrating the interaction of the 5×5 reconstructed surface with C_{60} fullerenes. (a) Image taken after the deposition of C_{60} molecules for 5 minutes. The image shows adsorption of individual molecules and the formation of a 27-fold cluster (V_s = 1.80 V, I_t = 0.18 nA). (b) A magnified STM image of the 27-fold cluster. The cluster exhibits the shape of a hexagon (V_s = 1.80 V, I_t = 0.18 nA). (c) A geometrical model of the 27-fold cluster. The schematic illustrates that the corner molecules of the cluster are slightly shifted from the centre of the corner hole adsorption site in order to accommodate three molecules along the long side.

Fig. 5.5a features the adsorption of individual molecules, and the formation of a 27-fold cluster. A magnified STM image of the 27-fold cluster is shown in Fig. 5.5b. The cluster exhibits three-fold rotational symmetry. All the observed 27-fold clusters have an identical shape and orientation with respect to the underlying 5×5 surface. Within the cluster, there are three molecules at the centre and one at each corner that appear dim as compared to other molecules. This indicates that these molecules are topographically lower than the bright ones. The apparent height difference between the three dim molecules relative to the bright ones is ~1 Å, while the corner dim molecules

reside 1.7 ± 0.3 Å lower than the bright molecules. This demonstrates that the adsorption geometry of the corner molecules of the hexagon is different from the central dim molecules. The measured variation in apparent height of C_{60} molecules is consistent with the corrugation of the 5×5 reconstruction, indicating that this effect is due to the structural features of the underlying substrate surface.

Based on experimental investigations, a geometrical model of the 27-fold cluster is shown in Fig. 5.5c. The schematic shows the arrangement of C_{60} molecules in the cluster with respect to the 5×5 reconstruction. A hexagonal grid, pink lines, in the figure corresponds to the 5×5 lattice, where the grid intersections correspond to triangular holes of the substrate. The sketched spheres correspond to C_{60} molecules with a diameter of 1.01 nm (van der Waals diameter). The green spheres correspond to C_{60} molecules that appear dim in the cluster, whereas the yellow spheres represent the bright molecules. The average separation between dim molecules along the long side is 3.10 ± 0.06 nm as measured from a number of STM images, which is greater than the unit cell of the 5×5 reconstruction i.e., 2.76 nm. Similarly, the average separation between the centres of dim molecules along the short side of hexagon has a value of 2.39 ± 0.08 nm which is smaller than the unit cell of the 5×5 reconstruction. The observed difference in the length of sides in the cluster and the unit cell of the underlying substrate could be understood in the scenario of the corner dim molecules which are slightly pushed from the centres of the triangular holes of the 5×5 substrate. The central two bright molecules (yellow spheres) along the long axis exert pressure on the corner dim molecules (green spheres) in order to accommodate the four molecules which results in a slight displacement of corner dim molecules from the centre of the triangular hole.

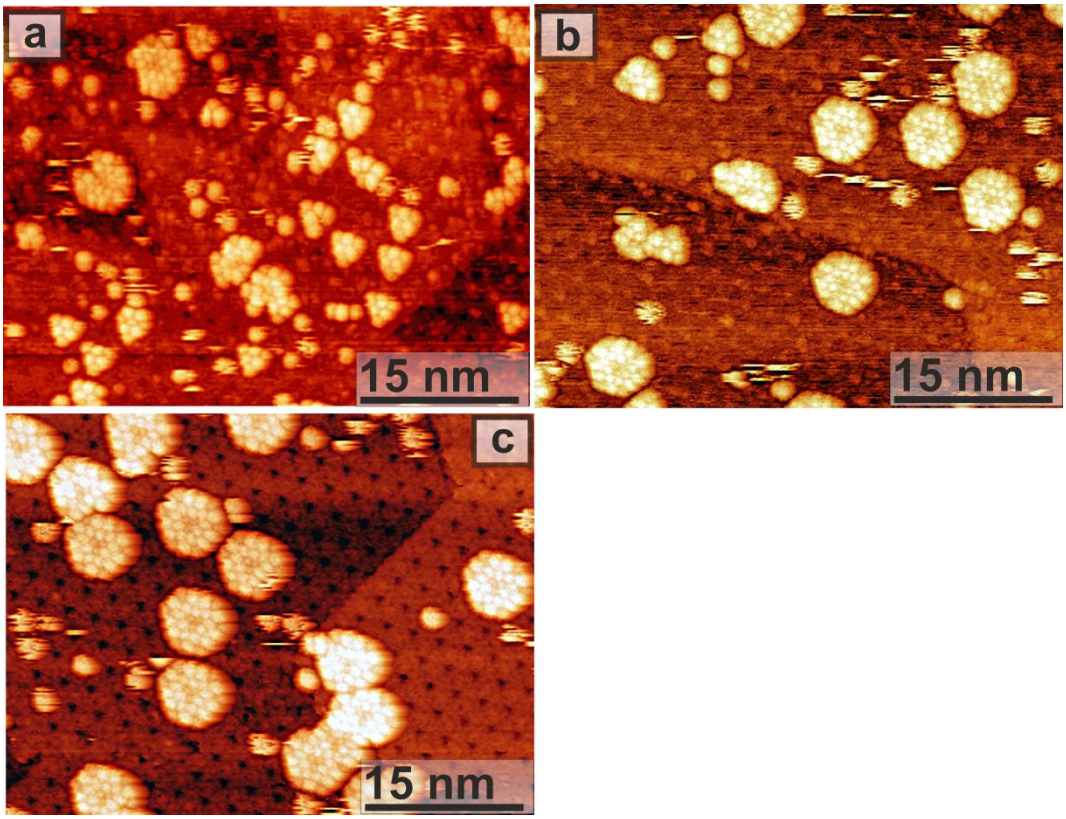

Fig. 5.6 STM images demonstrating the interaction of 5×5 reconstructed surface with C_{60} fullerenes at various depositions. (a) Image is taken after depositing C_{60} molecules for 10 minutes. In addition to individual adsorption, C_{60} arrange themselves into variety of clusters. The 6-fold and 27-fold cluster are frequently observed on the 5×5 reconstruction (V_s = 2.20 V, I_t = 0.21 nA). (b) A representative STM image of C_{60} fullerenes deposited for 15 minutes (V_s = 1.52 V, I_t = 0.26 nA). (c) STM showing that the number of of 27-fold clusters has increased at higher coverage (25 minutes) (V_s = 1.64 V, I_t = 0.26 nA).

Upon further increasing the deposition time to 10 minutes, the surface is covered with individual molecules and various clusters as shown in the STM image of Fig. 5.6a. The majority of the observed structures are the 6-fold and 27-fold clusters. It has also been observed that molecules are occasionally attached to or dragged by the STM tip during imaging that lead to the formation of 24, 25 and 26-fold clusters. The 28, 29 and 30-fold clusters appeared to have the same shape as that of the 27-fold cluster, except with additional molecules attached to either side of the 27-fold cluster. By increasing the deposition above 10 minutes, without subjecting the substrate to thermal annealing, the population of 27-fold clusters is observed to increase (Fig. 5.6b and 5.6c). However,

some regions of the surface also showed large islands with a close-packed separation of 1nm.

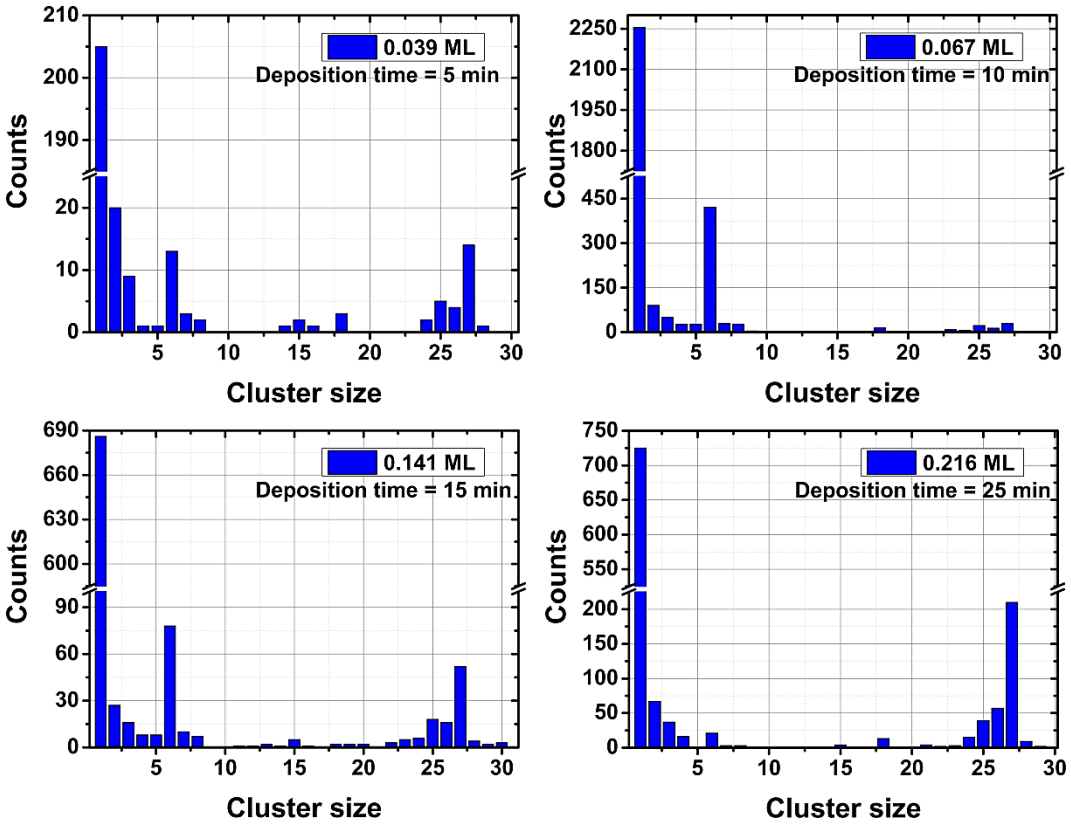

Fig. 5.7 Histograms for the number of C_{60} individual molecules and the magic clusters observed on the 5×5 reconstructed surface at 5, 10, 15 and 25 minutes of deposition time. The x-axis represents the cluster size i.e., the number of molecules in a cluster, whereas the y-axis shows the population of each cluster based on the statistical data of several STM images of each deposition time. The coverage of C_{60} for each deposition time is also indicated in the figure.

The statistical analysis of STM images for each deposition time is presented in Fig. 5.7. The number of individual molecules and clusters were counted in randomly chosen STM images. The figure depicts the histograms for 5, 10, 15 and 25 minutes of deposition. The coverage for each deposition time is also determined and shown in the figure. For 5 minutes of deposition, the majority of C_{60} molecules show individual adsorption and form magic clusters. When the deposition time is further increased to 10 minutes, the number of individual molecules as well as the formation of magic clusters is increased. At higher coverage, when molecules are deposited for times greater than

10 minutes, the observed population of 27-fold clusters shows an increase while the number of 6-fold clusters and the individually adsorbed molecule count is reduced.

5.5 Discussion

When molecules are deposited at room temperature, the 6×6 surface encouraged the formation of usual close-packed island as was also observed for other surfaces [101]. This indicates that the 6×6 reconstructed surface interacts weakly with fullerene, and molecules tend to optimize their intermolecular interactions (van der Waals) through the island formation. In contrast, the $SrTiO_3$(111)-5×5 reconstructed surface has a strong influence on the ordering of fullerene molecules. Fullerenes absorbed as individual molecules and also produced molecular clusters with magic numbers on the 5×5 reconstruction. The dark triangular corner hole of the 5×5 unit cell, as shown in Fig. 5.2a and 5.2b, appears to be a highly preferential bonding site for the fullerenes molecules. Among the semiconductors, silicon surfaces have been demonstrated to interact strongly with fullerene molecules. Individual fullerenes have been reported to scatter across the Si(111)-7×7 surface randomly with various adsorption configurations, where close-packed island formation is completely inhibited [118, 121, 125]. C_{70} fullerenes, in the present study, also produced clusters among which 6-fold clusters are in the majority and have a well-defined triangular shape. In case of C_{60}, the most frequently observed clusters are the 6-fold and 27-fold with well-defined geometrical shapes. The important difference in the adsorption behaviour of C_{70} and C_{60} on the 5×5 surface was the tendency to adsorb individually and the absence of 27-fold clusters in the case C_{70}. The individual adsorption of C_{70} is highly favourable on this surface as compared to C_{60} as demonstrated by the images shown in Fig. 5.3 and Fig. 5.6. The number of individually adsorbed molecules rises as the deposition time goes up and most of the triangular holes of the unit cell are occupied for the deposition time of 25 min (Fig. 5.3). The absence of 27-fold clusters in the case of C_{70} could be understood in

the scenario of molecular structure of C_{70} fullerenes. C_{70} exhibits the shape of a rugby ball and could adopt two possible orientations on the surface i.e. "standing" and "lying down" [172]. If C_{70} has to produce the 27-fold clusters, a standing orientation will be required to adopt a similar configuration as that of C_{60}. The lack of 27-fold clusters suggests that C_{70} fullerenes may need more energy to adopt this particular configuration. The population of 6-fold clusters in case of C_{70} molecules is observed to increase when the deposition time rises from 5 min to 10 min. However, their number reduced for deposition duration higher than 10 min (Fig. 5.4). This decrease is most probably an outcome of large island formation at higher coverage when molecule-molecule interactions start competing with the molecule-substrate interaction. In the case of C_{60}, the population of 27-fold clusters increases throughout with the deposition time. However, the population of individually adsorbed molecules and 6-fold clusters decreases for deposition time longer than 10 min (Fig. 5.7). The throughout consistent increase of 27-fold cluster population with coverage and decrease of 6-fold cluster and individually adsorbed molecule population at higher coverage indicates that 27-fold cluster formation is not only highly favoured but also most stable packing configuration for C_{60} on 5×5 surface.

5.6 Summary

In summary, I have demonstrated a distinct behaviour of fullerenes C_{60} and C_{70} on the non-stoichiometric 5×5 and 6×6 reconstructions of polar $SrTiO_3$(111) surface. Fullerenes, deposited at room temperature, produced close-packed islands on the 6×6 reconstruction. However, both C_{60} and C_{70} adsorbed individually and produced clusters with well-defined shape and orientation with respect to the underlying 5×5 reconstruction. The chemical nature and topographic features of the 5×5 reconstruction has a dominant role in the confinement of individual fullerenes to a specific adsorption site and stabilizing the clusters with magic numbers. The observation of individual

adsorption along with magic clusters points to the higher reactivity of the 5×5 reconstruction as compared to the 6×6 reconstructed surface. The higher reactivity is most likely related to the higher oxygen depletion in the former reconstruction as compared to the latter [29]. These systems, possessing the additional advantage of room temperature stability, could be further developed for novel electronic devices by understanding the important concepts related to the physical properties of these magic clusters. Furthermore, the $SrTiO_3$(111)-5×5 reconstruction is appealing from the structural point of view and could serve as an template for growth of other functional molecules, such as endohederal fullerenes, for the development of future electronic devices.

Chapter 6

Templated ordering of fullerenes on $SrTiO_3$(111) reconstructed surfaces

6.1 Background and overview

In the previous chapter, the influence of reconstructed $SrTiO_3$(111) surfaces on the adsorption behaviour of fullerene molecules was investigated. The $SrTiO_3$(111)-5×5 surface, which is a highly reduced surface among the family of (n×n) reconstructions, interacted strongly with fullerenes as indicated by the individual adsorption and the formation of magic clusters. The triangular hole of the 5×5 unit cell appeared to be highly reactive due to its dominant role in the individual adsorption and stabilizing the clusters. Such exotic arrangement of fullerenes raises an interesting question: How does the surface reactivity of the 5×5 reconstruction affect the ordering of fullerene overlayers? On the other hand, the 6×6 reconstruction exhibited weaker interaction with fullerenes and allowed them to form close-packed islands through the molecule-molecule interactions. The nature of interaction between a surface and fullerenes varies for different reconstructions [30]. This is due to the difference in chemical nature and surface topography of the template surface that could modify the properties of fullerene molecules as a result of charge transfer between the molecules and the surface. The

charge transfer between the molecule and the semiconductor or metal surfaces could significantly influence the distribution of electronic charge and their geometric configuration at the interface [101, 103]. Moreover, growth of fullerenes on patterned surfaces has recently attracted much interest due to their potential applications in molecular based devices. This also emphasizes the importance of the nature of molecule-substrate interface for device performance. The results reported in this chapter are based on the investigation of surface reactivity of the $SrTiO_3$(111)-n×n reconstructions through fullerene overlayers on the surface. The thermal annealing of the $SrTiO_3$(111) reconstructed surface covered with fullerene molecules, deposited at room temperature, are expected to produce close-packed islands through the migration and/or diffusion of molecules on the surface. The results are discussed and interpreted to investigate the reactivity of various reconstructions of the (n×n) family.

6.2 Experimental methods

The techniques used in this chapter are similar to those in previous chapters. All the experiments were carried out in the JSTM-4500XT system. The samples were prepared according to the preparation methods discussed in chapter 4. In brief, the samples were first sputtered and then annealed to prepare atomically flat reconstructed surfaces. Fullerenes, C_{60} and $C_{70,}$ were first deposited at room temperature on the reconstructed surfaces to investigate the influence of the template surface on the adsorption behaviour of fullerene molecules. These results are outlined in the previous chapter. The sample surfaces covered with molecules were then annealed at temperatures between 200-280 °C, and then cooled to room temperature. The STM investigations were carried out at room temperature.

6.3 Fullerenes on the 5×5 reconstruction

6.3.1 Self-assembly of C_{60}

The first template is based on the 5×5 reconstruction. Fig. 6.1a is an atomic resolution STM image of the 5×5 reconstruction with a surface unit cell indicated by a black diamond. C_{60} fullerenes, when deposited at room temperature, adsorbed individually and produced magic clusters on the 5×5 reconstructed surface (c.f. previous chapter). When the sample surface covered with C_{60} molecules is annealed at around 200 °C for 30 minutes, fullerenes coalesced into large islands. This is illustrated in the room temperature STM image of Fig. 6.1b, where two dimensional islands of C_{60} can be observed. This demonstrates that fullerenes are able to migrate on the surface at the annealing temperature, and islands are formed through the aggregation and rearrangement of fullerene clusters. A few regions, as an example, are indicated by white arrows where the 27-fold clusters can be seen to attach to the islands. The image also features individual molecules and isolated 27-fold clusters.

Although islands are observed in the STM images similar to that shown in Fig. 6.1b, long-range ordered domains of C_{60} molecules are not observed. The sample is therefore further annealed at higher temperatures between 250-280 °C for 30 minutes. During heating, C_{60} are expected to diffuse on the surface and produce well-ordered islands. Upon cooling the surface, STM images revealed the formation of ordered islands. An example is shown in the STM image of Fig. 6.1c, where an ordered overlayer can be observed. In contrast to fullerenes on other surfaces [292], the step edges are not preferential nucleation sites for the C_{60} islands. Instead, islands are observed in the terraces and sometimes along the step edges. The measured height of the C_{60} overlayer is typically of the order 1.0 nm, indicating the overlayer is single layer in thickness. The C_{60}-C_{60} nearest neighbour distance is measured to be 1.01 ± 0.06 nm.

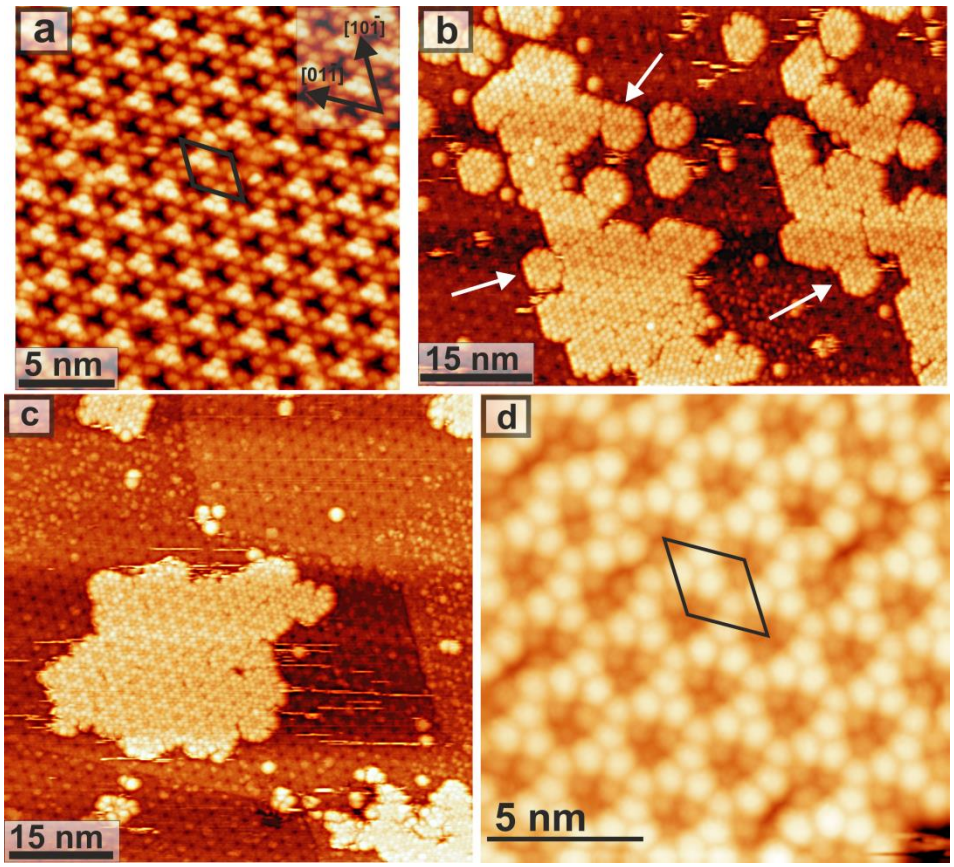

Fig. 6.1 Room temperature STM images of fullerene C_{60} on the $SrTiO_3$(111)-5×5 reconstructed surface. (a) An atomic resolution STM image of the 5×5 reconstructed surface. (b) Image showing the 27-fold clusters and large islands after annealing the sample at 200 °C for 30 minutes. (c) An epitaxial island of C_{60} array following annealing the surface at 250-280 °C for 30 minutes. The overlayer exhibits triangular features that run along the crystallographic direction of the template surface. (d) A high resolution STM image of the C_{60} overlayer, where the dim triangular features are clearly resolved. The dim triangles produce hexagonal pattern with a separation equivalent to that of the underlying 5×5 surface. Scanning parameters are: (a) V_s = 2.28 V, I_t = 0.26 nA (b) - (d) V_s = 1.61 V, I_t = 0.26 nA.

The C_{60} overlayer exhibits an ordered array of dim triangular features that run along the crystallographic direction of the substrate. Fig. 6.1d is a high resolution STM image of the C_{60} overlayer that features well organised hexagonal arrangement of the dim triangles of molecules. These triangles are periodically spaced at a separation of 2.77 ± 0.03 nm, which corresponds to the periodicity of underlying 5×5 substrate. This suggests an epitaxial relationship between the C_{60} overlayer and underlying surface. Furthermore, each triangle can be seen to consist of three molecules. These three molecules appear dim as compared to other molecules. The bright and dim contrast of

C_{60} molecules have been previously observed by STM on a variety of solid surfaces and attributed to adsorbate-induced reconstructions [101, 293, 294]. The driving force responsible for changing the structure of underneath surface has been attributed to strong molecules-substrate interactions, where dim molecules occupy nanopits of the reconstructed surface, and are situated lower than the bright molecules. However, in some cases the original surface reconstruction is preserved and the appearance of bright and dim C_{60} in the overlayer is associated with the structural features of the underlying substrate [142, 147, 292]. Other explanation, apart from the topographic variations of the substrate, suggests that the appearance of bright and dim molecules is due to the electronic and molecular orientation effects [295, 296]. The apparent height difference between the dim and bright molecules in the fullerene layer of Fig. 6.1d is averaged at 1.06 ± 0.16 Å. This is consistent with the corrugation measured for bare template surface, indicating the apparent height difference between the dim and bright molecules can be attributed to the surface topography. It is interesting to note that the 27-fold cluster also contain three dim molecules at the centre, where the measured apparent height difference between the bright and dim molecules has a value (~1 Å) consistent with that measured in the present case. This suggests that the C_{60} ordered arrangement evolved from the conglomeration and rearrangement of the 27-fold clusters.

In order to identify the adsorption positions of the C_{60}, grid lines are drawn through the centre of the triangular holes of 5×5 lattice. This is demonstrated in the STM image of Fig. 6.2a, where intersection of grid lines locates the position of the triangular hole. It can be seen that the lines are intersecting at the centre of dim molecular triangle. A schematic representation of a unit cell of the C_{60} array, superimposed on the STM image of $SrTiO_3$(111)- 5×5 surface is shown in Fig. 6.2b. The sketched circles correspond to C_{60} molecules with a diameter of 1.0 nm (van der Waals diameter). In the figure, a green triangle is marked that represents the adsorption positions of dim C_{60} sitting on top of the dots i.e. corners of the green triangle. The

adsorption positions of bright molecules are represented by a yellow triangle (the bright part of the 5×5 unit cell). A geometrical model of the C_{60} array, based on the experimental investigations, is illustrated in Fig. 6.2c. The yellow spheres represent C_{60} molecules that are situated on the bright part of underlying 5×5 unit cell, whereas the green spheres correspond to the dim molecules and occupy the dark part.

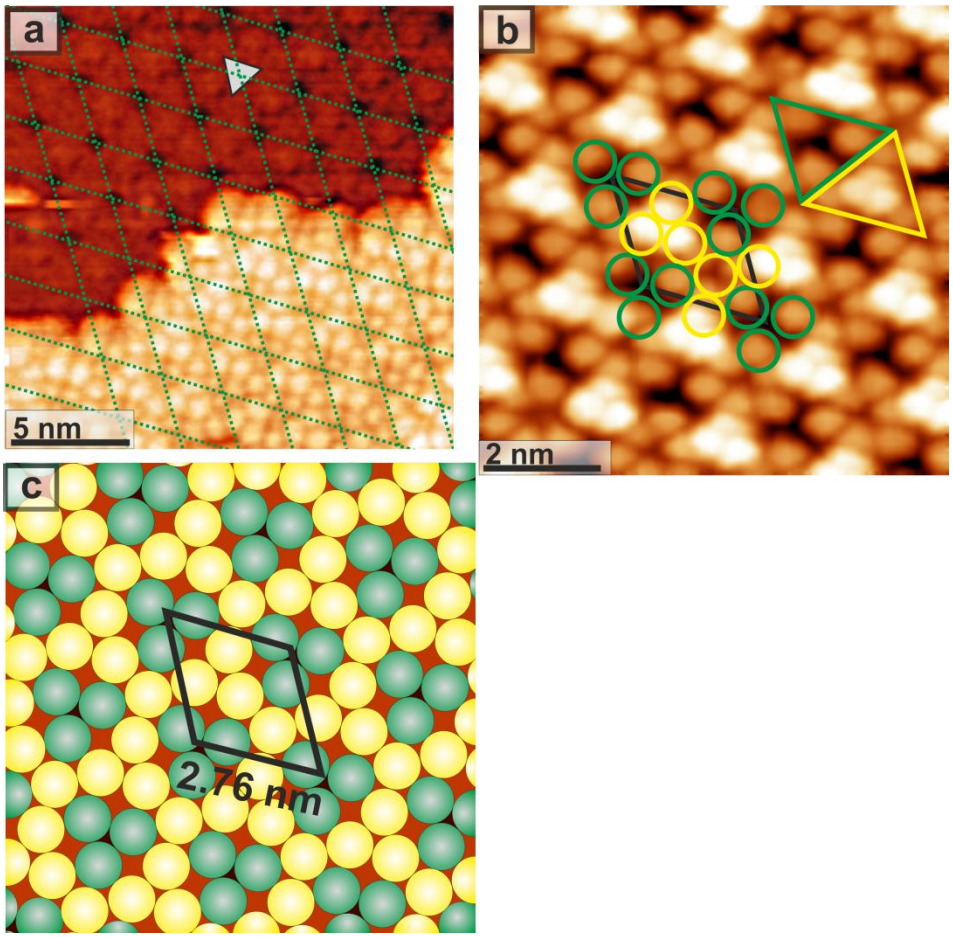

Fig. 6.2 (a) STM image showing superposed gridlines to identify the adsorption positions of dim molecules within the C_{60} array relative to the 5×5 reconstructed surface. The triangular hole of the 5×5 unit cell is also drawn for clarity and lies at the intersection point of grid lines. (b) A schematic representation showing the arrangement of C_{60} superimposed on the STM image 5×5 reconstruction. (c) A geometrical model of the C_{60} overlayer. The green spheres correspond to the dim molecules, whereas the yellow spheres represent the bright molecules.

The proposed mechanism of the molecular configuration shown in Fig. 6.1 and 6.2 can be further understood by carefully considering the relationship between different molecular structures. This is shown in the schematic of Fig. 6.3, where the evolution from one ordered structure to another is shown. The cluster growth sequence

as shown in the figure is illustrative only and for the purpose of showing the repeating molecular motif. The green spheres in the figure correspond to molecules adsorbed at the triangular hole, which appear dim in the ordered structure, whilst the yellow spheres represent the bright molecules. Initially, when deposition is performed with the substrate held at room temperature, molecules adsorb individually and produce various clusters (c.f. Chapter 5). The clusters are formed as a result of molecular diffusion to form energetically favoured ordered structures, the size and shape of which is determined by various factors such as the topographic features of the surface. The majority of the observed clusters are 6-fold and 27-fold. The formation of 6-fold cluster is illustrated in Fig 6.3a, where three trapped molecules at the triangular holes of the unit cell surround three molecules occupying positions atop the surface. Similarly, the 27-fold cluster evolves when three 6-fold clusters arrange themselves in such a way that the corner molecule of each 6-fold cluster shares the triangular hole of the 5×5 unit cell (Fig. 6.3b). The empty space between the clusters is then filled by the capturing of nine additional molecules to form the 27-fold cluster as indicated by the small arrows.

Fig. 6.3c demonstrates a proposed mechanism for the formation of an ordered overlayer during the heat treatment of the sample. From careful inspection of the STM images, it appears that the 6-fold cluster captures an additional molecule during the diffusion process which leads to the rearrangement of molecules in such a way that a close-packed structure consisting of seven molecules is formed. This is shown in the figure, where three dim molecules produced a close-packed arrangement with four bright molecules. In this particular arrangement, the dim molecules are slightly displaced from the centre of the triangular hole. The ordered arrangement of the C_{60} overlayer then evolves through the aggregation of these close-packed structures, shown in Fig. 6.3d, as repeated units of the ordered overlayer. The footprint of the central three dim molecules in the ordered arrangement is similar to that of the 27-fold cluster.

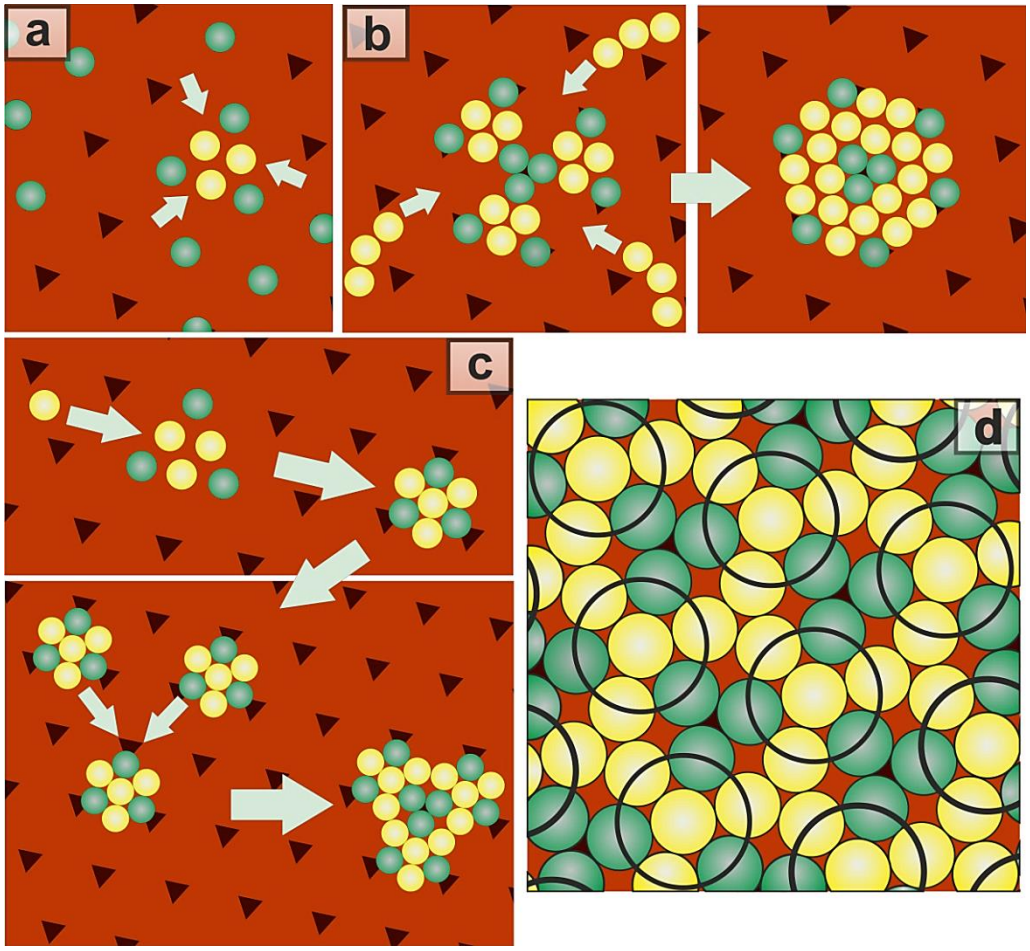

Fig. 6.3 Models showing the evolution of the ordered structures. Green spheres are C_{60} molecules adsorbed at the triangular hole of the 5×5 unit cell, whilst the yellow represent the molecules residing atop the surface. (a) Figure showing the adsorption of individual molecules and formation of 6-fold cluster. (b) The evolution of 27-fold cluster from the 6-fold cluster. (c) A proposed mechanism showing the formation mechanism of the two dimensional ordered overlayer during heat treatment of the sample. (d) The ordered overlayer is composed of repeated closed packed structures, with the component seven-member units indicated with black rings.

C_{60} molecules also produced another ordered phase on the 5×5 reconstructed surface. STM images of this arrangement are shown in Fig. 6.4. Scanning the sample surface over a large area reveals the formation of two dimensional islands as shown in Fig. 6.4a. The height of fullerene islands measured from STM images is 0.96 ± 0.06 nm. The fullerene layer exhibits dim features of molecules that are aligned along the crystallographic directions of 5×5 reconstructed surface. These features consist either of single or three molecules as can be seen in the inset of Fig. 6.4a. The arrangement of

three dim molecules is similar to that observed in the first phase shown in Fig. 6.1d. The dim features are separated by 2.80 ± 0.13 nm, which is comparable to that of the 5×5 unit cell.

A close inspection of STM images reveals that some regions of the fullerene islands exhibit a well-ordered arrangement of the molecules, where the dim molecules form an ordered array with hexagonal pattern (Fig. 6.4b and 6.4c). Within the island, the dim molecules are situated 1.74 ± 0.42 Å lower than the bright molecules. This is consistent with the measured depth of triangular hole of 5×5 unit cell, i-e., 1.9 ± 0.3 Å, suggesting that dim C_{60} are pinned at the triangular hole of template unit cell. This is further demonstrated in the STM image of Fig. 6.4b, where the grid lines are drawn through the centre of the corner holes of 5×5 lattice. The intersection of these grid lines locates the position of the triangular hole. In the image, the lines are intersecting at the position of dim molecules and hence justifying the adsorption of these molecules on the corner hole of the underlying template surface. Within the ordered domain as shown in the high resolution STM image of Fig. 6.4c, dim molecules are periodically spaced at a separation equivalent to the width of three fullerenes giving a closed-pack separation of 0.95 nm. This value is smaller than the equilibrium van der Waals diameter of fullerenes, but is in good agreement with the close-packed separation measured in other STM studies of fullerenes on surfaces [292, 297]. Based on these observations, a geometrical model of the ordered arrangement of C_{60} molecules is illustrated in Fig. 6.4d. The yellow and green spheres correspond to bright and dim molecules, respectively. The hexagonal arrangement, however, exhibits a short range order typically of the order of few unit cells. Annealing conditions, such as further annealing of the sample for longer time and/or at slightly higher temperature, appear to have no effect in producing an ordered arrangement over extended area. After a brief annealing of the sample at temperature above 500 °C, molecules desorb from the surface without decomposition.

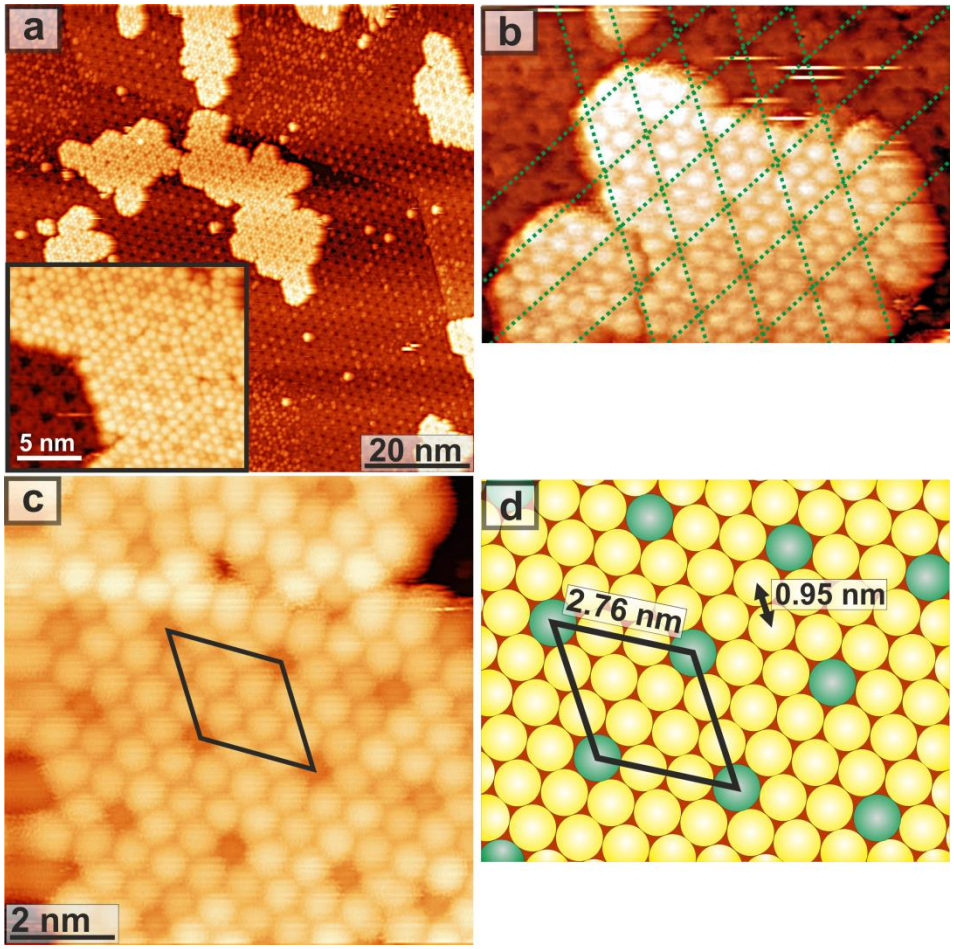

Fig. 6.4 STM images and geometrical model of an ordered phase produced by C_{60} fullerenes on the $SrTiO_3$(111)-5×5 reconstructed surface. (a) The image showing two dimensional islands of C_{60} molecules. The inset shows a magnified STM image, where the dim features of single and three molecules can be observed. (b) Image showing grid lines are superposed to tie the position of dim molecules of the C_{60} array. (c) A high resolution STM image showing an ordered array of dim molecules arranged in hexagonal manner. (d) A geometrical model of the C_{60} ordered phase. The green spheres are dim molecules, pinned at the corner hole of 5×5 unit cell, and the yellow spheres correspond to bright molecules in the fullerene layer. Scanning parameters are: (a) V_s = 1.61 V, I_t = 0.26 nA (b) V_s = 1.61 V, I_t = 0.26 nA (c) V_s = 1.61 V, I_t = 0.26 nA.

6.3.2 Self-assembly of C_{70}

Upon room temperature deposition, C_{70} molecules adsorbed individually and produced magic clusters on the 5×5 reconstructed surface (c.f. previous chapter). When the surface is annealed at 250-280 °C for 30 minutes, two dimensional islands are observed in the STM images. Fig. 6.5a shows a room temperature STM image of the surface. The formation of large islands indicates that molecules are not strongly bonded

to the surface, and are able to migrate on the surface during the heat treatment. The individual molecules and 6-fold clusters are also observed on the surface, and are evident in the figure. The height of C_{70} islands, measured from the STM images, is 1.01 ± 0.10 nm. The C_{70} fullerenes produced a hexagonal structure similar to that of C_{60} illustrated in the STM image of Fig. 6.4c. This indicates that the C_{70} layer adopted a commensurate growth similar to that observed for C_{60} molecules. A high resolution STM image of the C_{70} island is shown in Fig. 6.5b. Like the case for C_{60}, the C_{70} overlayer also exhibits an ordered array of dim molecules arranged in hexagonal pattern. The measured depth of the dim molecules, relative to the bright ones, in the hexagonal domain is ≈ 2 Å. The dim molecules are periodically spaced at 2.80 ± 0.11 nm, which is comparable to that of underlying surface.

Fullerene C_{70} resembles a rugby ball, having a van der Waals diameter of 1.01 nm and 1.06 along the minor and major axis, respectively. When deposited on solid surfaces, C_{70} molecules can adopt two orientations: "standing" and "lying down", where the major axis is perpendicular and parallel to the surface, respectively [172, 298, 299]. In the "standing" orientation, C_{70} molecules are expected to adopt the same arrangement as that of C_{60}. This is due to the fact that the diameter of C_{70} molecules along the minor axes is similar to that of that of C_{60} fullerenes, and would represent spheres when projected on a two dimensional plane. Therefore, the observed arrangement can be attributed to "standing" orientation of C_{70} fullerenes. However, it raises an immediate question that why C_{70} fullerenes do not produce the ordered arrangement similar to that observed for C_{60} in Fig. 6.1d? A possible explanation could be related to the triangular features of C_{60} overlayer that resembles the central three dim molecules of the 27-fold clusters. As discussed above, the ordered domain shown in Fig. 6.1d is most likely formed by the conglomeration and rearrangement of the 27-fold clusters. Since C_{70} fullerenes do not produce 27-fold clusters, it explains why an arrangement similar to that of Fig. 6.1d is not formed here and also justifies the

formation mechanism of epitaxial island of Fig. 6.1d from 27-fold cluster at the same time.

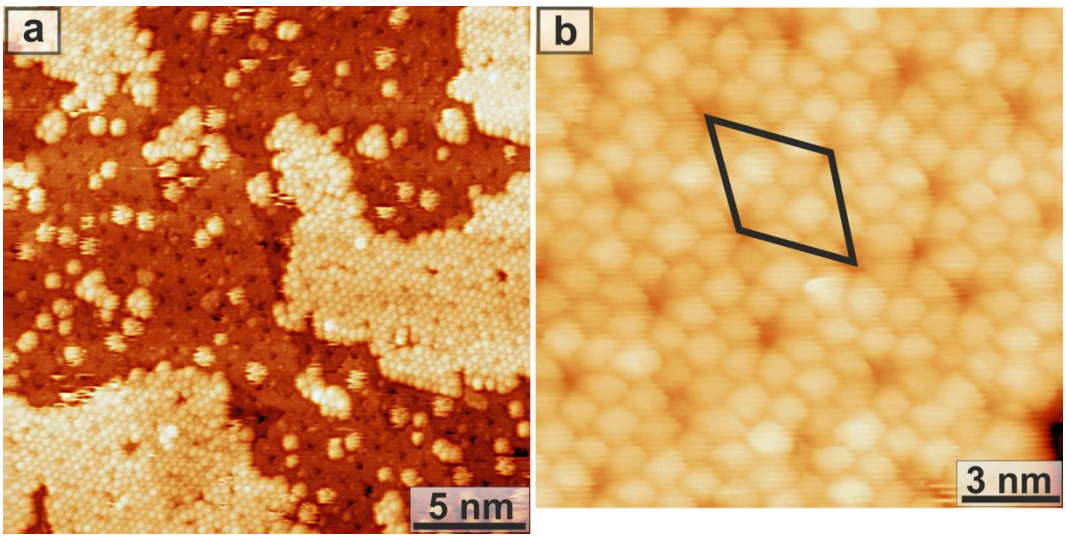

Fig. 6.5 STM images of fullerene C_{70} on the $SrTiO_3$(111)-5×5 reconstructed surface. (a) The image shows large islands of fullerenes C_{70}. The fullerene layers maintain an epitaxial relationship with the underlying substrate. The individual molecules and 6-fold clusters are also evident in the image. (b) A high resolution STM image of the C_{70} array showing the hexagonal arrangement of dim molecules. The scanning parameters are: (a) V_s = 2V, I_t = 0.2 nA (b) V_s = 2V, I_t = 0.2 nA.

C_{70} also formed another ordered phase on the 5×5 reconstructed surface. Fig. 6.6a is an STM image showing an island of the C_{70} fullerenes. The apparent height of the islands is measured to be of the order of 1nm. The C_{70}-C_{70} nearest neighbour distance is measured to be 1.08 ± 0.04 nm. The fullerene layer exhibits a periodic array of dim molecules arranged in hexagonal manner. This is shown in the high resolution STM image of Fig. 6.6b, where an ordered arrangement can be seen. The measured depth of the dim molecules relative to the bright ones is ~1.9 Å. The separation between two neighbour dim molecules is measured to be 2.75 ± 0.10 nm, which is equivalent to the unit cell periodicity of the underlying 5×5 surface. However, careful analysis of several STM images suggests that the crystallographic directions of the C_{70} overlayer are not aligned with that of the template surface. Instead, axes of the fullerenes lattice is rotated

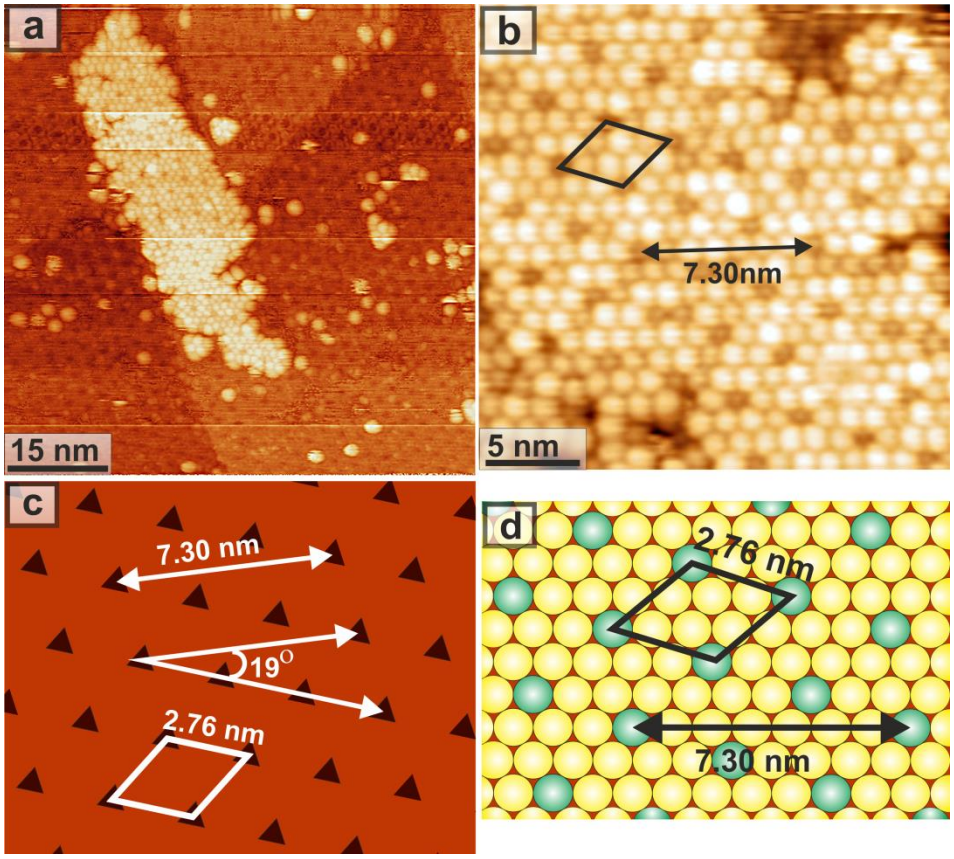

Fig. 6.6 Room temperature STM images and schematic representation of fullerene C_{70} on the $SrTiO_3$(111)-5×5 reconstructed surface. (a) STM image showing a large island, where C_{70} adopted a substrate commensurate growth (V_s = 2.0 V, I_t = 0.2 nA). (b) A high resolution STM image of the C_{70} ordered domain. The image shows an ordered array of dim molecules, where the separation between two neighbour dim molecules is equivalent to that of the underlying surface. The unit cell indicated by a black diamond corresponds to that of the 5×5 reconstruction (V_s = 2.0 V, I_t = 0.2 nA). (c) A schematic showing the C_{70} array is rotated by 19° with respect to the underlying 5×5 surface. (d) A geometrical model for the C_{70} adopting a lying down configuration. The unit cell of the 5×5 reconstruction is also indicated the figure.

by 19° with respect to that of the template surface, consistent with that reported by Russell [55]. The separation between two dim molecules along the fullerene row, measured from the STM images, is 7.29 ± 0.04 nm and is indicated in the figure. A similar value was also obtained for a bare surface, when the separation was measured between two triangular holes of the 5×5 lattice along the direction of C_{70} lattice. This is illustrated in the schematic of Fig. 6.6c that shows the orientation of both lattices. This suggests that the dim molecules occupy the triangular hole of the unit cell, where the two lattices overlap with each other. As the periodicity of underlying 5×5 surface is

2.76 nm and equals 7.30 nm when multiplied by √7, C_{70} fullerenes lattice adopt a (√7×√7)*a*-R19° arrangement, where *a* = 2.76 nm [55].

C_{70} fullerenes, due to their reduced symmetry, can generally adopt either the "standing" or "lying down" orientation on the substrate surface. In the "standing" orientation, the ordered arrangement of C_{70} would be similar to that of C_{60}, which has already been observed and discussed above (Fig. 6.5). Since the van der Waals diameter of a C_{70} molecule along the minor axis is 1.01 nm, and seven molecules will have a length of 7.07 nm which is less than 7.30 nm. On the other hand, along the major axis, seven molecules will have a length of 7.42 nm which is close to the measured value of 7.30 nm [55]. Hence, it is most likely that C_{70} adopt the lying down orientation and is in agreement with that reported by Russell. A geometrical model for the C_{70} ordered array is shown in in Fig. 6.6d, where the yellow and green spheres correspond to bright and dim C_{70} fullerenes, respectively. The model assumes that C_{70} adopt a "lying down" configuration on the surface with long axes along the horizontal direction. In each row, six C_{70} fullerenes are followed by a dim molecule. Similar to the case for C_{60}, the desorption temperature of C_{70} fullerenes is around 500 °C.

6.4 Fullerenes on the 6×6 reconstruction

The influence of 6×6 reconstruction on the growth of fullerenes is also investigated. An STM image of the 6×6 reconstructed surface is shown in Fig. 6.7a. The image shows bright spots that are frequently observed on the 6×6 surface. These bright spots are not molecules but could be unknown species that are observed on this particular surface. Fullerenes C_{70}, deposited on the 6×6 reconstructed surface at room temperature, produced non-epitaxial islands. The surface covered with fullerenes is then annealed at 200 °C for 30 minutes. Fig. 6.7b shows an STM image of the surface covered with C_{70} islands. The islands are typically found in the middle of terraces and

do not show preferential growth along the step edges. The height of fullerene layer is measured to be on the order of 1nm, and the C_{70}-C_{70} nearest neighbour distance is measured to be 1.1 ± 0.07 nm. The C_{70} islands appear disordered and are not influenced by the underlying 6×6 substrate. This suggests that the relationship between molecules and the surface is not epitaxial.

Fullerenes C_{60}, deposited at room temperature for 25 minutes, produced large islands on the 6×6 reconstruction. After annealing the sample at 200 °C for 30 minutes, the C_{60} islands formed a well-ordered arrangement. Fig. 6.7c shows a room temperature STM image of the surface, where C_{60} molecules have produced a typical close-packed structure. The height of C_{60} layer with respect to the template surface is measured to be 0.95 ± 0.04 nm. The C_{60}-C_{60} intermolecular distance in the fullerene layer is averaged at 9.7 ± 0.1 Å, which is slightly less than the van der Waals diameter of C_{60}. The C_{60} overlayer exhibits bright and dim contrast of molecules. The dim patterns of molecules appear to follow the crystallographic direction of the 6×6 reconstruction. The measured periodicity of a unit cell, indicated in the inset of Fig. 6.7c, within the C_{60} array is 3.32 ± 0.04 nm, which is equivalent to that of the 6×6 reconstruction. This suggests an epitaxial relationship between the fullerenes and substrate surface. The apparent height difference between dim and bright molecules is 0.92 ± 0.19 Å. The topographic features of 6×6 reconstruction involve triangular depressions that are ~ 1 Å in depth. The origin of bright and dim molecules in the STM images could be attributed to the corrugation of the substrate, where the dim molecules are situated at lower adsorption site than the bright molecules. A geometrical model is shown in Fig. 6.7d, where the dim and bright molecules are represented by green and yellow spheres, respectively.

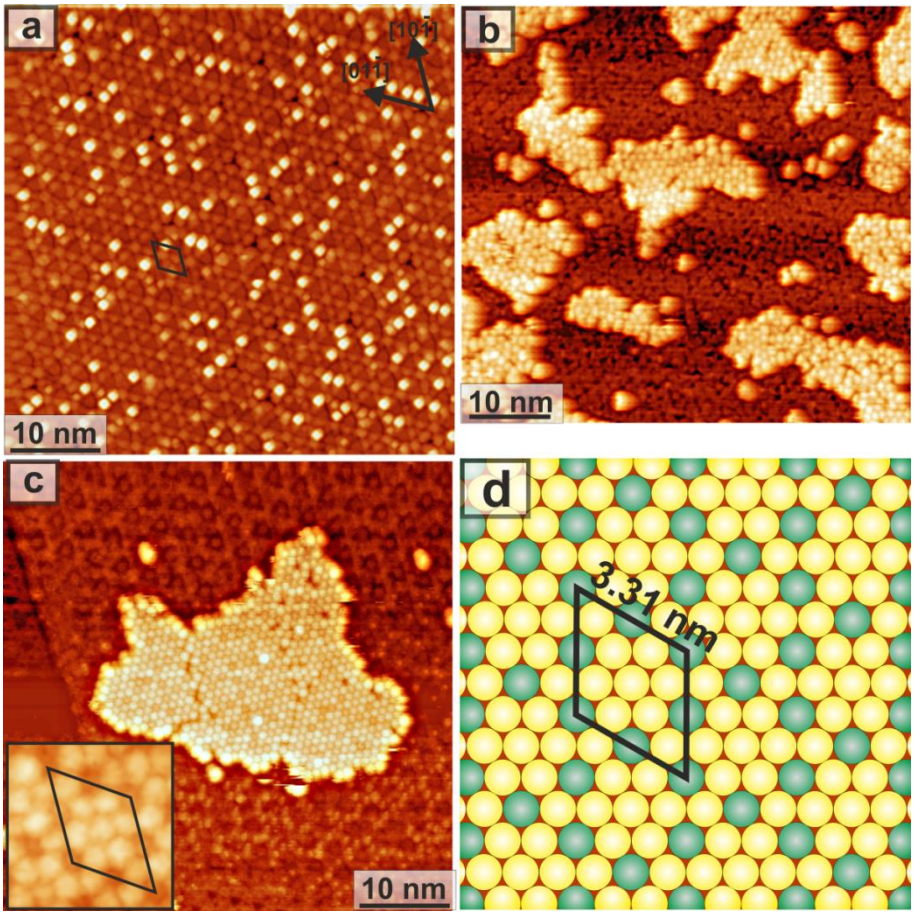

Fig. 6.7 (a) A high resolution STM image of the 6×6 reconstructed surface. (b) STM image showing islands of the C_{70} fullerenes. The island appear disordered and there is no relationship between the C_{70} overlayer and the underlying 6×6 reconstruction (c) STM image showing an island of the C_{60} fullerenes. The C_{60} array exhibits bright and dim molecules, where the dim pattern of molecules run along the crystallographic direction of the substrate and the overlayer maintain an epitaxial relationship. The inset is a zoomed STM image showing the unit cell of the C_{60} ordered phase. (d) A proposed geometrical model of the C_{60} array. Scanning parameters are: (a) V_s = 1.85V, I_t = 0.26 nA, (b) V_s = 2.0 V, I_t = 0.18 nA (c) V_s = 1.61 V, I_t = 0.26 nA.

6.5 Fullerenes on the 4×4 reconstruction

The third template in the course of surface reactivity investigation is based on the 4×4 reconstruction. An atomic resolution STM image of the 4×4 reconstruction is illustrated in STM image of Fig. 6.8a. A unit cell of the 4×4 reconstructed surface is indicated by a white diamond. Room temperature deposition of fullerene molecules for 15 minutes on 4×4 surface resulted in the formation of non-epitaxial islands. The samples were then annealed at 200 °C for 30 minutes to obtain ordered overlayers. A

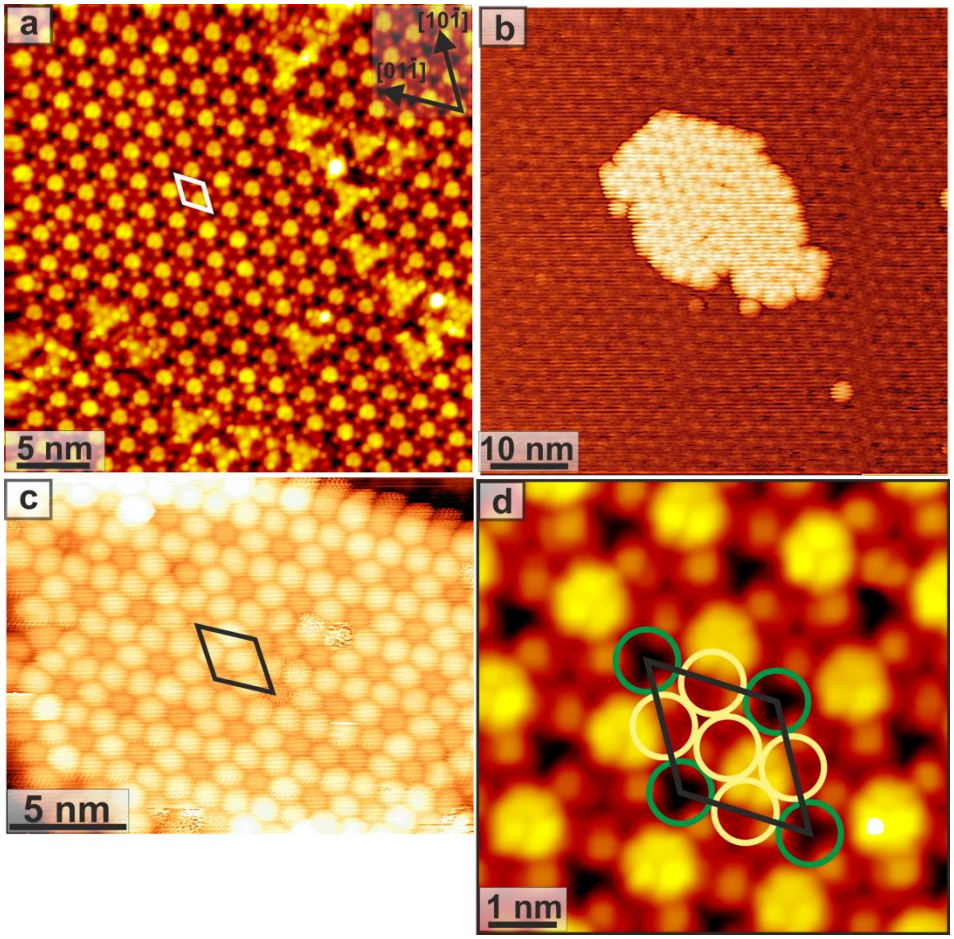

Fig. 6.8 Representative STM images of C_{70} fullerenes deposited on the $SrTiO_3$(111)-4×4 reconstructed surface. (a) Atomic resolution STM image of the 4×4 surface. (b) An epitaxial island of C_{70} on the 4×4 reconstructed surface. (c) A high resolution STM image of the C_{70} overlayer. (d) Schematic illustration of a unit cell of the fullerene array superimposed on the atomic resolution STM image of $SrTiO_3$ (111)- 4×4 surface. The green circles correspond to the dim molecules, whereas the yellow circles represent the bright molecules. Scanning parameters: (a) V_s = 2.0 V, I_t = 0.50 nA, (b) V_s = 2.0 V, I_t = 0.20 nA, (c) V_s = 2.0 V, I_t = 0.23 nA. (d) V_s = 2.0 V, I_t = 0.50 nA.

representative STM image is shown in Fig. 6.8b, where C_{70} produced two dimensional islands. The apparent height of the C_{70} islands measured from the STM images is found to be 0.95 ± 0.05 nm, indicating the overlayer is a single layer in thickness. Step edges are not favoured as preferential bonding sites. Instead, the C_{70} islands are typically observed in the middle of terraces and sometime along the step edges. The C_{70}-C_{70} close-packed separation measured from a number STM of images is found to be 1.11 ± 0.03 nm. This separation is comparable to the van der Waals radii of C_{70} and is in line with previous STM studies of C_{70} on other surfaces [170]. A high resolution STM

image of the fullerene island is shown in Fig. 6.8c. The overlayer consists of an ordered array of dim molecules that are arranged in hexagonal pattern. These dim molecules are periodically spaced at 2.22 ± 0.04 nm, which corresponds to the periodicity of underlying 4×4 surface. This indicates an epitaxial relationship between the C_{70} overlayer and template surface. The apparent height difference between the bright and dim molecules in the C_{70} overlayer is measured at 1.45 ± 0.30 Å. The 4×4 reconstruction, as shown in Fig. 6.8a, exhibits triangles which can be seen as dark depressions in the STM image. The depth of these triangles, measured from the line profile of STM images, is 1.50 ± 0.12 Å. This suggests that appearance of dim and bright patterns in the C_{70} overlayer is due to the structural features of the underling surface, where the dim molecules occupy the triangular hole of the unit cell and are situated slightly lower than the bright molecules. Deposition of C_{60} for 15 minutes on the 4×4 surface at room temperature and subsequent annealing at 200 °C for 30 minutes revealed the formation of close-packed islands identical to that of C_{70} overlayer demonstrated in STM images of Fig. 6.8b and 6.8c. A schematic representation of the hexagonal array of fullerenes, superimposed on the STM image of underling 4×4 surface, is shown in Fig. 6.8d. The sketched circles are 1 nm in diameter and correspond to the van der Waals diameter of fullerenes. Molecules are sketched as green and yellow circles that represent molecules adsorbed at the triangular hole and atop the surface, respectively.

Since both C_{60} and C_{70} fullerenes produced similar ordered arrangements on the 4×4 reconstructed surface, one would expect that C_{70} adopt a “standing” orientation on the surface. In this case, C_{70} molecules would represent spheres of similar size as that of C_{60} fullerenes. A geometric representation of this arrangement is shown in Fig. 6.9a. Fullerenes are sketched as spheres of diameter equal to 1 nm, which is the equilibrium van der Waals diameter. The green spheres correspond to molecules that appear dim in

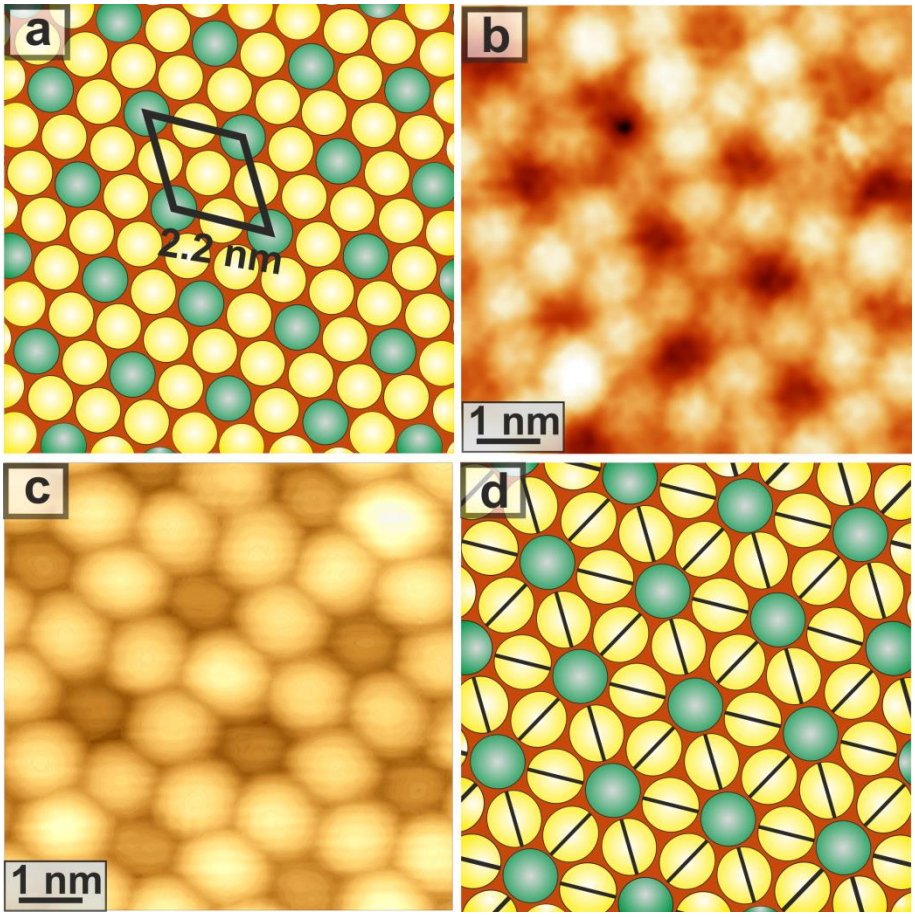

Fig. 6.9 (a) A representative model of the fullerene overlayer, where the green sphere represents molecules adsorbed at the corner hole of the 4×4 unit cell triangle and yellow spheres reside atop the surface. (b) A magnified STM images of C_{60} molecules adopting an arrangement similar to that shown in part a. (c) A zoomed STM image of the C_{70} island showing the lying down orientation. The bright molecules appear to be rotating with respect to each other, whilst the dim appears as circular. (d) A representative model of the C_{70} overlayer, where each bright molecule is rotated by 60 degrees with respect to its neighbours. The black lines are drawn to represent the major axis of C_{70} molecules.

the overlayer, whereas the bright molecules are represented by the yellow spheres. The black diamond corresponds to the unit cell of ordered arrangement, which also represents the unit cell of 4×4 reconstruction. However, it is also possible that C_{70} molecules could adopt a "lying down" orientation. This is due to the fact that the available space is large enough to fit any configuration of C_{70} molecules. This would allow maximum number of carbon (C) atoms to interact with the underlying surface that in turn result in a strong bonding as compared to the standing orientation. Fig. 6.9b and 6.9c are the high resolution STM images of C_{60} and C_{70} fullerenes, respectively. It

can be seen that C_{60} appear spherical in the STM image, whereas the C_{70} fullerenes appear as elongated. This suggests the lying down orientation of C_{70} molecules. Moreover, the Fig. 6.9c also demonstrates that the bright C_{70} molecules are rotated with respect to each other. Although, the orientation of dim molecules cannot be clearly resolved in the STM image, it is more likely that these molecules adopt the standing orientation. In this way, each dim molecule with a standing orientation would be surrounded by six bright molecules that are rotated with respect to each other. This can be better understood by the geometrical model of Fig. 6.9d, where the major axis of each bright molecule (yellow sphere) is rotated by 60 degrees with respect to its neighbours. By repeating this arrangement, the model would produce the pattern observed in the STM image of Fig. 6.9c.

6.6 Molecule substrate interactions

The $SrTiO_3$(111)-5×5 reconstructed surface causes fullerenes C_{60} and C_{70} to adsorb individually and produce magic clusters upon room temperature deposition. These adsorption configurations are highly stable not only at room temperature but also at higher annealing temperatures as demonstrated in the STM images of Fig. 6.1a and 6.5a. Due to strong interaction of the substrate surface with fullerenes, relatively high annealing temperatures are required to produce well-ordered epitaxial islands. After annealing the sample at temperature around 250-280 °C, well-ordered epitaxial islands of C_{60} molecules are formed on the surface (Fig. 6.1 and 6.4). Similarly, C_{70} produced epitaxial ordered phases with standing and lying down configuration (Fig. 6.5 and 6.6). The self-assembly of molecules on a solid surface is governed by a balance between molecule-molecule and molecule-substrate interactions. The interplay between molecules and surface play a more subtle role due to the chemical nature and surface topography of the substrate surface. The 5×5 reconstruction strongly influences the way molecules assembled on the surface as evident by the highly compact ordered

arrangement of C_{70} and C_{60} molecules (Fig. 6.4 and 6.5). Moreover, after a brief annealing above 500 °C, fullerenes desorb without decomposition from the 5×5 surface. The desorption temperature for C_{60} overlayer having weak or predominantly ionic interactions with different substrates has been reported to be 427- 600 °C [30, 300]. If we use the desorption temperature as a measure to determine the molecule-substrate bonding strength, the interaction of C_{60} submonolayer with the 5×5 surface can be attributed to either strong van der Waals or weakly/predominantly ionic [30].

The molecule-substrate bond strength reduces significantly for the 6×6 reconstruction. The relationship between the C_{70} overlayer and its underlying surface is found to be non-epitaxial. Annealing the surface has no effect to order the C_{70} fullerenes. C_{60} molecules, however, produced epitaxial overlayers on 6×6 surface upon annealing at 200 °C followed by cooling to room temperature (Fig. 6.7). The 4×4 surface produced epitaxial overlayers for both type of fullerenes pointing to a stronger molecule-substrate interaction for this template compared to the 6×6 reconstruction although being relatively less oxygen deficient. The surface topographic features of 6×6 surface are comparatively flat and hence the lack of site coordination results in a weak interaction between the substrate and the molecules. Based on above experimental observations, the 5×5 surface appeared to have the highest molecule-substrate bond strength while the 6×6 reconstruction has the least. One could suggest that both the non-stoichiometry and surface topographic features determine the extent of molecule-substrate interaction and hence the surface reactivity.

6.7 Summary and conclusion

To summarize, the surface reactivity of non-stoichiometric 5×5, 6×6, and 4×4 reconstructions on the $SrTiO_3$(111) surface is investigated through the self-assembly of fullerene molecules. Close-packed overlayers are obtained through annealing of the

$SrTiO_3$(111) reconstructed surfaces covered with fullerenes. The 5×5 reconstructed surface strongly dictates the self-assembly of fullerenes. Distinct epitaxial islands of C_{60} and C_{70} are observed on the 5×5 reconstructed surface owing to strong molecules-substrate interactions. The presence of individually adsorbed molecules and magic clusters, which forms immediately upon deposition of fullerene molecules at room temperature, even after annealing further justifies the strong bonding between molecules and the substrate. C_{70} fullerenes produce two ordered phases on the 5×5 surface by adopting the "standing" and "lying down" configurations. The 6×6 reconstruction, on the other hand, interacts less strongly with fullerenes as indicated by the non-epitaxial growth of C_{70} molecules on this template surface. This is most likely due to the relatively flat surface topographic features. The 4×4 reconstruction drives an epitaxial growth of both C_{60} and C_{70} molecules and hence more reactive than the 6×6 reconstruction. The relatively strong molecule-substrate bonding strength of the 4×4 reconstruction as compared to that of 6×6 surface is most likely due to its surface topography.

Chapter 7

The role of oxygen vacancies in the bulk properties of $SrTiO_3$ single crystals

7.1 Background and overview

Previous chapters were mainly focused on the reconstructions on the $SrTiO_3$(111) surface and their utilization for template assisted growth of fullerenes. Surface reconstructions were produced through Ar^+ sputtering and subsequent annealing in UHV or in an oxidizing environment. Deviation from the ideal stoichiometry in the bulk of the crystal is also known to induce various physical properties [44, 255, 267]. In this context, oxygen vacancies are particularly intriguing [301]. Many fascinating phenomena such as ferromagnetism [4, 302, 303], superconductivity [304] and room temperature luminescence [267] have been reported due to oxygen vacancies. Since the oxygen vacancies act as electron donors, electrical transport properties can be controlled by incorporating the oxygen vacancy content in $SrTiO_3$ [39]. Oxygen vacancy related defects are also known to produce the in-gap states [250, 301] and hence lead to modification in the electronic structure of material. This implies that the capability of controlling these point defects is essential for tailoring the electronic properties.

One of the simplest routes to incorporate the oxygen vacancies in metal oxides is high temperature annealing in a reducing atmosphere [243]. Oxygen content can be controlled by simply varying the experimental parameters such as annealing temperature, annealing time, and oxygen partial pressure in the annealing environment. There is a substantial amount of work on the elucidation of physical properties in $SrTiO_3$ induced by thermal annealing in a reduced environment [39, 254, 256, 305]. Various structural forms of $SrTiO_3$ are studied, such as polycrystal, thin film and single crystal where single crystal being the most ordered form. Extended defects are found to be very important as they could accumulate the oxygen vacancies in a confined region [251]. Moreover, the spatial distribution of the oxygen vacancy complexes can enhance or decrease the free carrier density [249]. Despite of widespread investigations on the reduced $SrTiO_3$, a clear understanding of intrinsic defects has not yet been achieved. The following chapter is focused on the electrical and luminescence properties of thermally reduced $SrTiO_3$ single crystal. Evolution of these properties with annealing time is utilized for the understanding of oxygen vacancy defects and their distribution within the crystal. Temperature dependent electrical transport and cathodoluminescence study is combined with electron paramagnetic resonance spectroscopy to get information over the role of oxygen vacancies in determining the physical properties of $SrTiO_3$ single crystals.

7.2 Experimental details

Epi-polised (001) oriented $SrTiO_3$ single crystals were supplied by PI-KEM Ltd., UK. As-received crystals ($2\times7\times0.5$ mm^3) were found to be electrically insulating, and were introduced into an ultra-high vacuum (UHV) system (model JSPM-4500S), operating at a base pressure of 10^{-8} Pa. Heat treatments were performed in the UHV at 750°C for times between 5-25 hours to controllably introduce oxygen vacancies into the as received material. The details of methods used to investigate the bulk properties

of the $SrTiO_3$ singles crystals are given in Chapter 2. Electrical resistivity measurements were performed, as a part of collaborative work, by Dr Naureen Akhtar at Zernike Institute for Advanced Materials, University of Groningen, The Netherlands. Cathodoluminescence (CL) measurements were carried out in a JEOL JSM 6500F scanning electron microscope (SEM) equipped with a CL detector. A sample holder was modified to investigate the CL properties of the as-received and reduced singles crystals under the same conditions. The ESR results reported in this chapter were obtained in a collaborative effort with Dr Richard George. The measurements were performed using an X-band spectrometer (Bruker EMX) housed in the CAESR, Inorganic Chemistry Laboratory, Oxford.

7.3 Results and discussion

7.3.1 Temperature dependence of electrical resistivity

Electrical resistivity of the reduced crystals was measured using standard four-probe method in the temperature range of 8-300 K. Fig. 7.1 shows the temperature dependence of the resistivity (ρ) of the reduced single crystals for different annealing times (t_{red}). A monotonic decrease in $\rho(T)$ is observed with increasing annealing times. This indicates that number density of free carriers increases throughout as t_{red} goes up, in contrast to some prior reports of an inhomogeneous thermal reduction process [251, 254, 255]. It is important to shed light on the nature of thermal reduction in single crystals before proceeding to the discussion of electronic transport properties. The character of the thermal reduction process is emphasized as highly inhomogeneous in some recent reports [254, 255], with the inhomogeneity associated with ‘easy’ diffusion paths for oxygen established at dislocations [253]. The density of dislocations is found to be higher within the near-surface region [252] leading to a concentration gradient of oxygen vacancies from surface to interior of the crystal. One of the prior reports on inhomogeneous reduction by K. Szot *et al.* [254] observed a decrease in resistivity with

annealing time only for $t_{red} \leq 10$ minutes. They showed that a prolonged annealing at 800 °C decreased the concentration of initially introduced defects as a result of a self-healing phenomenon, leading to a recovery in the resistivity of single crystal.

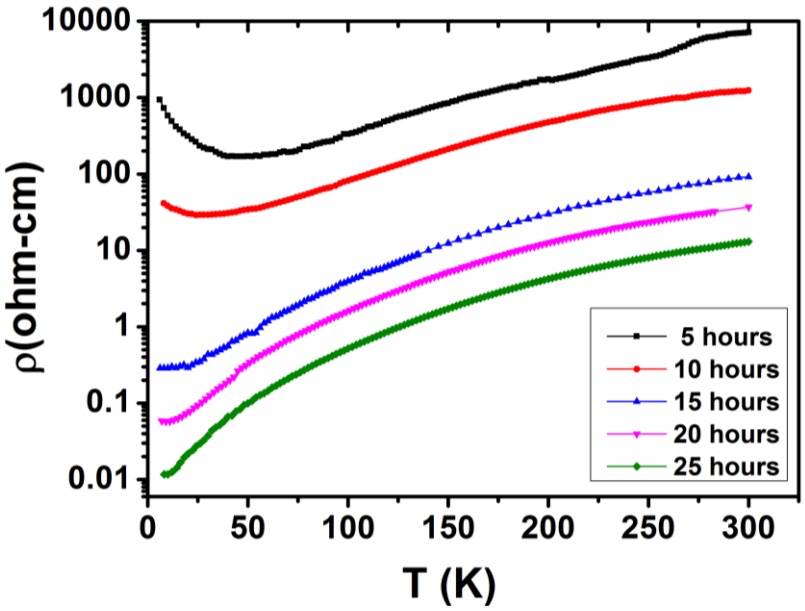

Fig. 7.1 Temperature (T) dependence of Resistivity (ρ) of reduced $SrTiO_3$ single crystals for different reduction times t_{red}. Annealing conditions used to reduce the samples are $P(O_2) = 7.5 \times 10^{-8}$ Pa, T=750 °C.

Another recent report by Spinelli *et al.* [39], however, argues against the strong inhomogeneous reduction process in $SrTiO_3$ single crystals. They studied the electronic transport properties in both Nb-doped and reduced single crystals and observed consistent behaviour of ρ(T) between both. This supports the homogeneous conduction in the reduced samples. They also observed a decreasing trend of resistivity with increasing annealing temperature. The number of oxygen vacancies should rise with an increase in annealing temperature and/or annealing time. Since our results also show a consistent decrease in resistivity with increasing t_{red}, the distribution of oxygen vacancies in reduced single crystals is expected to be homogenous.

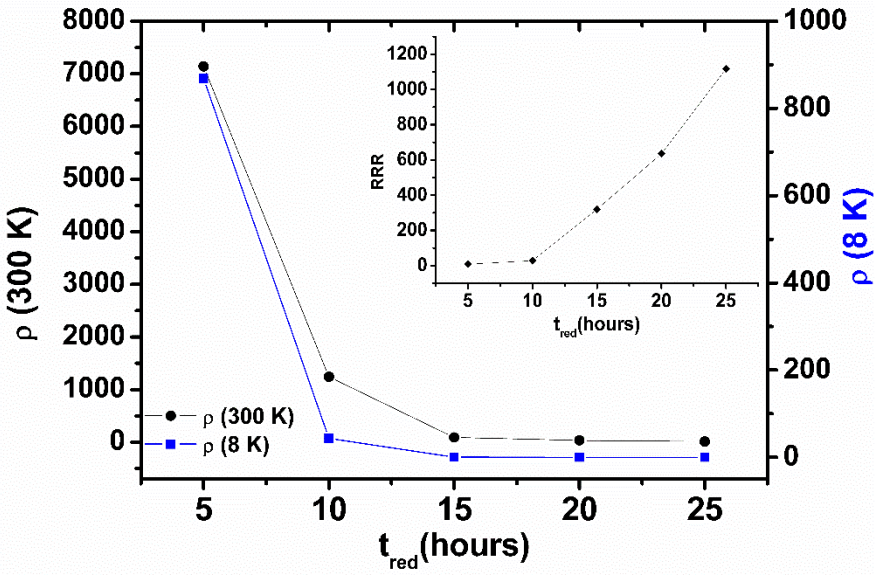

Fig. 7.2 Room temperature resistivity (ρ(300 K)) and resistivity at 8 K (ρ(8 K)) plotted as a function of annealing time (t_{red}). Inset is the residual resistivity ratio (RRR) plotted against t_{red}.

The ρ-T curves exhibit metallic behaviour for t_{red} = 15, 20 and 25 hours as shown by a positive dρ/dT in the whole temperature range (Fig. 7.1). However, dρ/dT changes sign for T < 40 K and T < 25 K for samples annealed for 5 and 10 hours respectively. The increase in low T-resistivity with decreasing temperature for lightly doped $SrTiO_3$ is observed in several studies [242, 255, 305] and is mostly attributed to the carrier freeze-out effects. In the present case, samples that are annealed for shorter times (t_{red} ≤10 hours) also exhibit carrier freeze-out which is seen as increase in resistance upon cooling at low temperatures.

The residual resistivity ratio (RRR), calculated as ρ(300 K)/ρ(8 K), increases with t_{red} and reaches a value as high as 1116. Such high values have been reported to occur in electron doped $SrTiO_3$ and at $LaAlO_3/SrTiO_3$ interfaces [39, 257, 306]. Fig. 7.2 shows the plot of ρ at 300 K and 8 K as a function of t_{red} with inset presenting RRR vs t_{red}. A sharp change in ρ and RRR is observed when t_{red} was raised from 5 hours to 15 hours which is also reflected as crossover from positive to negative dρ/dT in Fig. 7.1.

7.3.2 Electron spin resonance spectroscopy investigations

7.3.2.1 Paramagnetic centres in the as-received $SrTiO_3$ single crystal

Electrical resistivity measurements showed the presence of free carriers in reduced samples and their number increases with an increase in t_{red}. Oxygen vacancy may have different characters and the corresponding impact on the physical properties varies accordingly [248-250]. It can have different charged states and can also cluster with neighbouring oxygen vacancies, hence inducing additional electronic levels in the conduction band and/or within the band gap [249, 250, 301]. Position of these electronic levels within the band gap is, however, puzzling and reported with values varying from 0.003 eV to 1.0 eV below the conduction band bottom based on various theoretical and experimental studies [250, 301, 307-309]. To identify the defect centres associated with thermal annealing in the $SrTiO_3$ single crystals, ESR has been used to get required information. Since electrical resistivity measurements could not be performed on as-received crystal due to a high resistance, the ESR measurements were performed to identify the possible defects and their local structure. The obtained results will give information over the quality of the crystal used in the present study and at the same time will elucidate the effects of thermal annealing on the electronic structure and corresponding physical properties of $SrTiO_3$.

The as-received crystals showed no ESR signals at room temperature. Upon cooling the sample below 200 K, a number of resonance lines were observed. Angular dependent measurements were performed to identify the paramagnetic centres. Fig.7.3a shows the angular dependence of the as-received crystal at 110 K, above the structural phase transition of $SrTiO_3$. The resonance pattern is acquired by rotating the crystal, with the help of goniometer, by every 5° with respect to the magnetic field in a sweeping range of 1000-4000 G. The spectra show three families of point defects

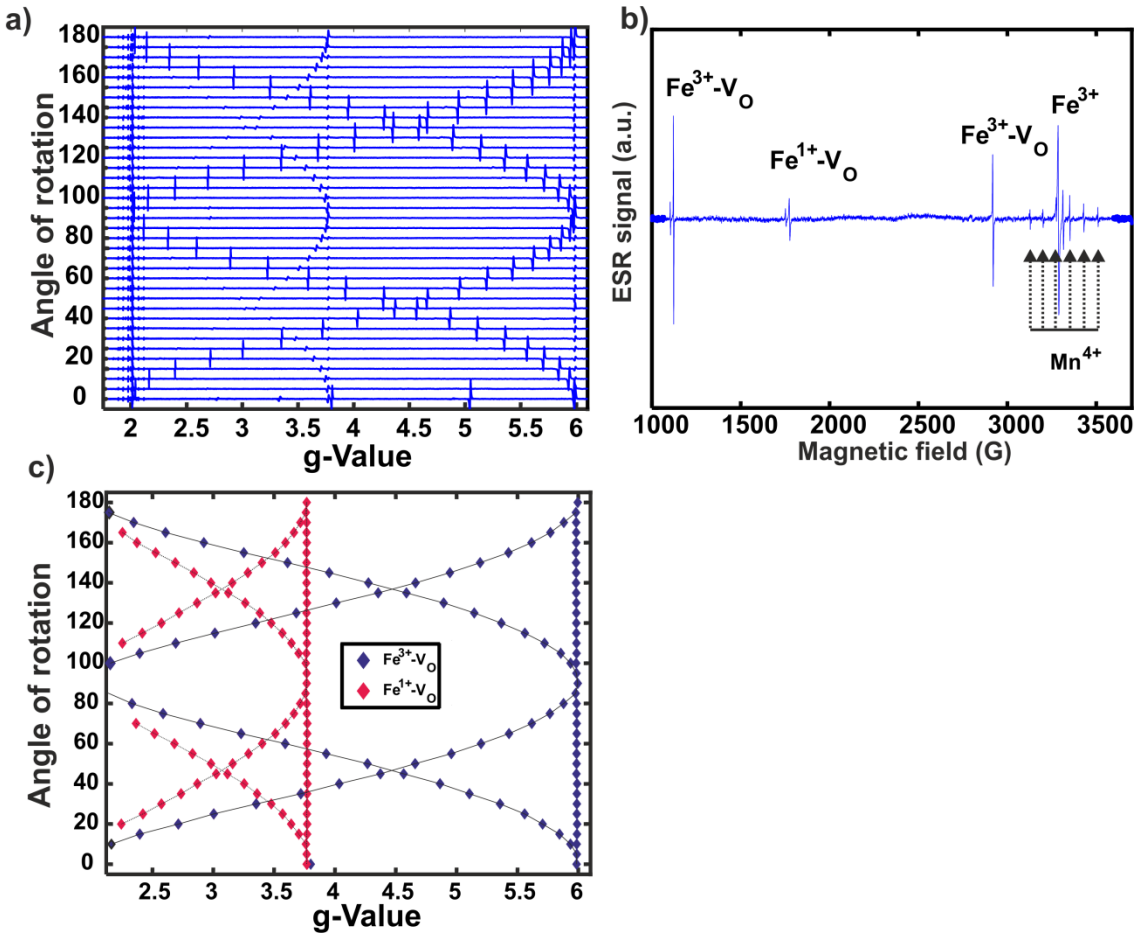

Fig. 7.3 (a) Angular dependence of the as-received $SrTiO_3$(001) single crystal measured at 110K. (b) The ESR spectrum showing the identified impurity centres. (c) The rotational behaviour of the Fe^{3+}-V_O and Fe^{1+}-V_O resonance fields for a rotation of magnetic field in the $SrTiO_3$ (001) plane.

belonging to the Fe centres. These are identified as Fe^{3+} [200, 201], Fe^{1+}-V_O [191, 192], and Fe^{3+}-V_O [198, 202], which are indicated in the ESR spectrum of Fig. 7.3b. The spectrum due to Fe^{3+} ions has been previously characterized with g-value equal to 2.004, and a cubic splitting parameter, *a*, of 0.02 cm^{-1} [194, 197, 200]. The iron-oxygen vacancy complex, Fe^{3+}-V_O, is an axial centre with strong anisotropic g-values between 2 and 6, and identical to those previously reported [197, 202]. The rotational behaviour of the resonance lines due to the Fe^{3+}-V_O centre is shown in Fig.7.3c for clarity, where the signal positions are represented by the blue diamonds. The third paramagnetic centre, Fe^{1+}-V_O, also consists of an axial line with anisotropic g-value ranging between 2 and 4 [191]. The resonance lines due to Fe^{1+}-V_O centre, in the present study, are

weaker than those of the Fe^{3+}-V_O complex. This suggests that the defect concentration of Fe^{1+}-V_O complex is lower than that of Fe^{3+}-V_O. The rotational behaviour of the g-values of Fe^{1+}-V_O is shown in Fig. 7.3c with red diamonds. The Fe^{1+}-V_O centre was previously reported to be a metastable state, and only observed after exposing a highly reduced sample to sub band-gap light [191, 192]. This indicates that the Fe^{1+}-V_O defect centre is stable in the present study and could be formed as a result of charge compensation. The ionic radius of Fe is comparable to that of Ti, and therefore preferentially substitutes Ti atoms octahedrally coordinated with six oxygen atoms in the host lattice. In order to maintain charge neutrality, the nearest oxygen atom leaves the crystal [189], giving rise to the above defect centres. In addition to the Fe related centres, a set of six isotropic resonance lines with a measured value of hyperfine constant around 75 ± 1 G and g = 1.994 ± 0.001 have also been observed. These lines are highlighted by the vertical dashed arrows in Fig.7.3b, and attributed to the Mn^{4+} ions substituted for Ti^{4+} in the host lattice [233].

The defect centres with different charge states are known to introduce various defect levels in the bandgap. The charge transfer mechanism between such defect centres and their light dependent properties have been widely studied with the aid of Photo-ESR. Having investigated the charge state and defect structure of Fe-vacancy complexes, this can be extended to study the influence of illumination on the signal intensity of their ESR spectrum. Although Fe^{1+}-V_O has previously been produced from Fe^{2+}-V_O by illuminating the sample with wavelength below 600 nm [191], the charge transfer mechanism between the Fe^{1+}-V_O and Fe^{3+}-V_O centres has not been studied yet. In order to investigate the photochromism of these defect centres in the as-received sample, ESR spectra are recorded under broadband illumination. The evolution of the relative intensity of defect centres are studied as a function of photon energy in the range ~1.45-3.0 eV (850-410 nm). Fig.7.4a shows the ESR spectrum due to Fe^{3+}-V_O

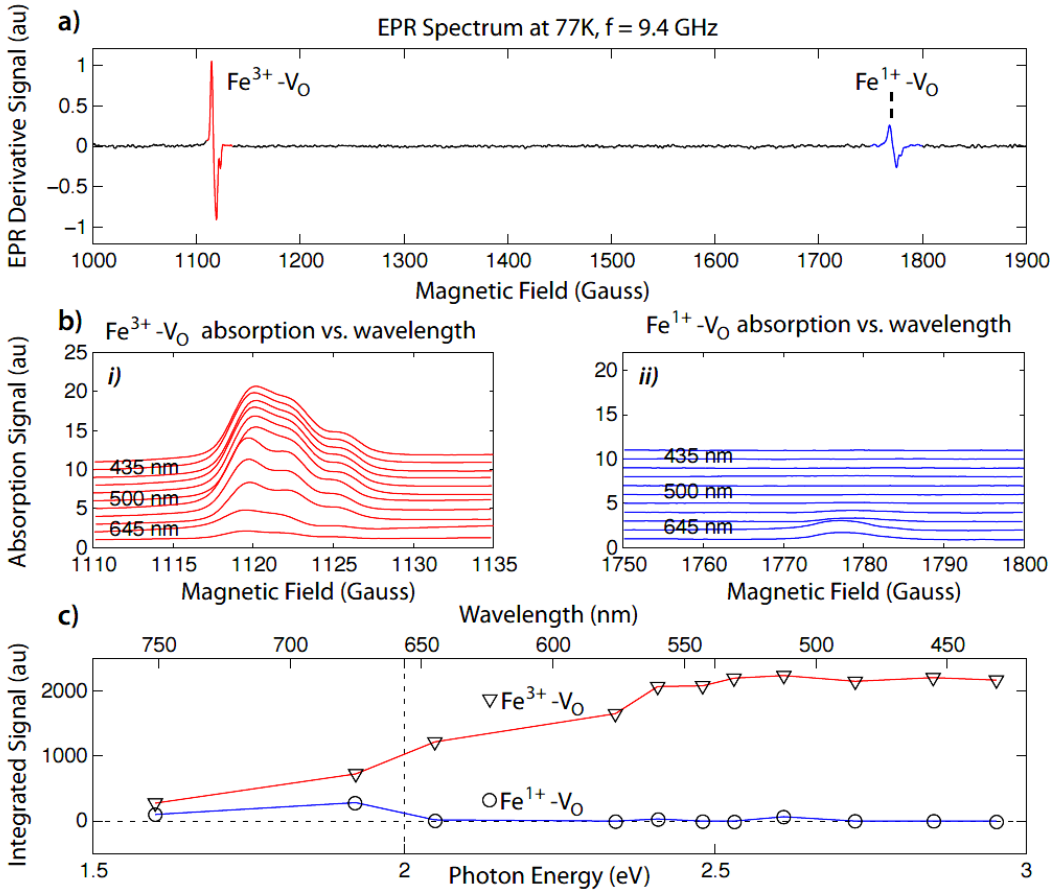

Fig. 7.4 Photo ESR data of Fe^{3+}-V_O and Fe^{1+}-V_O centres obtained from undoped sample. (a) ESR spectrum of the Fe^{3+}-V_O and Fe^{1+}-V_O centres taken at 77 K in the dark (b) Graphs showing the ESR spectra of both centres as a function of wavelength. (c) The intensity plot of Fe^{3+}-V_O (triangles) and Fe^{1+}-V_O (circles) centres as a function of energy.

and Fe^{1+}-V_O complexes taken in the dark at 77 K. Both the Fe^{3+}-V_O and Fe^{1+}-V_O shows a spectral response upon optical illumination over a range of wavelengths. Fig. 7.4 (b) and (c) shows the change in intensity of Fe^{3+}-V_O and Fe^{1+}-V_O complexes as a function of wavelength/energy, respectively. The intensity of the Fe^{3+}-V_O centre is observed to increase with photon energy and saturates at energy around ~ 2.5 eV, which is consistent with that reported by Dashdorj *et al.* [194]. In contrast, the signal due to Fe^{1+}-V_O centre disappears for photon energy greater than 2.1 eV. Scanning the sample over a wide magnetic field range showed no evidence of Fe^{2+}-V_O centre in the samples [191, 192]. Furthermore, resonance lines due to the Fe^{4+}-V_O centre [207] were also not observed in the measurements. The wavelength/energy dependent behaviour of the ESR

spectra of Fe^{3+}-Vo and Fe^{1+}-Vo complexes suggest a charger transfer mechanism. When the sample is irradiated with photons, an electron could be excited from the valence band edge to Fe^{4+}-V_O centre, a shallow acceptor in $SrTiO_3$ [210]. The capture of electrons at the Fe^{4+}-Vo defect level results in the creation of Fe^{3+}-Vo that causes the ESR intensity of Fe^{3+}-Vo to increase with optical illumination. This also gives an indirect indication of the presence of Fe^{4+}-V_O centre in the sample as this could only be the source to accept electrons and consequently convert to Fe^{3+}-V_O. The liberated holes produced during excitation could be subsequently trapped at Fe^{1+}-V_O centre forming Fe^{2+}-V_O which is not observed in the samples.

7.3.2.2 Ti^{3+} centre in the as-received and reduced crystals

ESR measurements have also been performed on the reduced samples to identify the defect centres. The samples that are reduced for 5 and 10 hours show an isotropic line centred at g = 1.9777, when measurements are performed at room temperature (Fig. 7.5a). This resonance line has been previously induced in samples that are highly reduced at temperature between 1100 °C and 1400 °C and quickly quenched to room temperature [310]. The origin of this centre has been attributed to the colour centre associated with oxygen vacancies. On the other hand, the highly reduced samples (t_{red} = 15, 20 and 25) showed no resonance at room temperature. This could be due to the conductive nature of the highly reduced samples, which lowered the Q factor of the cavity. Upon cooling the samples (t_{red} = 5, 10 hours) to temperature around 55 K, the EPR spectrum showed a number of resonance lines. The spectrum due to Fe^{3+}-V_O, Fe^{1+}-V_O and Mn^{4+} centres were not observed in any of the reduced samples. The angular dependent measurements are performed at 55K to identify the spin centres present in the reduced samples (Fig. 7.5b). The principal values of the g-factors measured from the angular dependence data are given below:

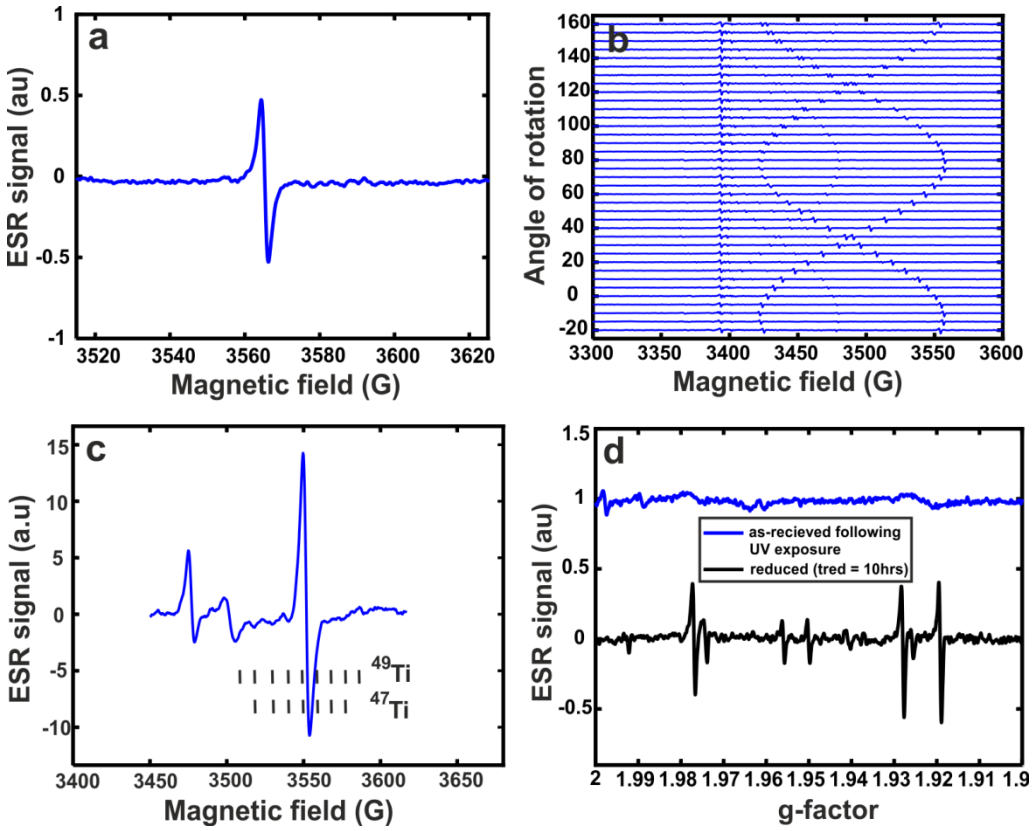

Fig. 7.5 The ESR spectrum of a sample reduced for 10 hours showing a resonance line due to a colour centre. (b) Angular dependencies of Ti^{3+} centres in the sample reduced for 10 hours at 55K. (c) Figure showing the hyperfine structure for the resonance line at g = 1.889. The spectrum is obtained at 55 K. (d) Plot showing the resonance lines due to Ti^{3+} centre in the as-received, following UV illumination, and reduced samples. The intensity due to Ti^{3+} centre in the reduced sample is stronger than that of the as-received crystal.

$$g_1 = 1.9960,\ g_2 = 1.9276,\ g_3 = 1.8879$$

These values are close to that of Ti^{3+} centre reported in the literature. The hyperfine structures for the resonance line at g = 1.8879 are weakly resolved after taking around 1600 scans. This is shown in Fig. 7.5c, where the hyperfine structure belonging to the ^{47}Ti (nuclear spin I = 5/2) and ^{49}Ti (I = 7/2) are indicated. The ^{47}Ti and ^{49}Ti exhibit natural abundance of 7.75% and 5.5%, respectively [241]. The value of hyperfine constant for the resonance line is determined to be 10 G, which is consistent with that measured by Laguta *et al.* [241] for the light-induced Ti^{3+} centres. Laguta *et al.* [241] observed the Ti^{3+} centre by illuminating the as-received $SrTiO_3$ single crystals with UV light. They suggested that Ti ions capture electrons from the valence band during the

illumination process, and give rise to ESR spectrum of Ti^{3+} centre. Apart from the photoinduced centre, another type of Ti^{3+} centre has also been reported in $SrTiO_3$ [237]. Schirmer *et al.* [237] suggested that Ti^{3+} is sitting "off centre" at a Sr^{2+} site and can be created by irradiating the as-received $SrTiO_3$ with fast neutrons, $E \geq 0.1$ MeV. According to their studies, Sr^{2+} vacancies are created during irradiation process and Ti^{3+} ion substituting the vacancy site migrate "off centre" towards one of the 12 O^{2-} due to relatively small ionic radii of Ti as compared to that of Sr ions. The same centre has also been reported in the reduced $SrTiO_3$ single crystals [238, 240]. However, it is important to note that the Ti^{3+} sitting "off centre" at a Sr^{2+} has not been observed by illuminating the sample with UV light.

The origin of Ti^{3+} centres in the present study are most likely arising from the in-site position of Ti ions as reported by Laguta *et al* [241]. This is due to the fact that the both the g-values and hyperfine structure are close to those measured by Laguta *et al*. Furthermore, measurements are performed on the as-received samples under UV-illumination to verify whether the ESR spectra arise from the anti-site Ti^{3+} ions on Sr^{2+} cites or from regular Ti sites. After illumination of the as-received crystal with UV light at 110 K, a new centre appeared in the ESR spectrum. The principal values of the g tensor, measured from the angular dependence of the resonance pattern, are varied between 1.996 and 1.8890. These values are consistent with those measured for the reduced samples, hence suggesting that the signal arises from regular Ti sites. However, the intensity of the photoinduced Ti^{3+} centre in the as-received samples is weaker as compared to that of the reduced crystals. This is shown in Fig. 7.5d, where the ESR spectrum of both the as-received and reduced samples is plotted. This indicates that the oxygen vacancies play an important role in the formation of Ti^{3+} centre, and can be attributed to Ti^{3+}-V_O centre.

7.3.3 Cathodoluminescence properties

Since the ESR technique is charge specific and can only give information about the paramagnetic defects, further investigations regarding the defects were performed by studying the luminescence behaviour of the samples. CL measurements are performed on $SrTiO_3$ single crystals with the incident electron beam voltage and current of 20 kV and 2×10^{-9} nA, respectively. Fig. 7.6 shows the CL spectra of as received and reduced samples. All the samples show an intense emission band in the blue region (~2.9 eV) and a weak emission band in the IR region (~1.5 eV). The IR luminescence arises from the intrinsic Schottky defects while the blue emission in $SrTiO_3$ is mainly attributed to oxygen vacancy centres [1, 279]. Luminescence intensity of the bands showed overall increasing trend with increasing t_{red} as shown in Fig. 7.6. This indicates that prolonged UHV annealing lead to an increase in oxygen vacancy content which results in higher number of electronic states within the band gap of the material. Hence, the corresponding radiative centres are increasing giving rise to higher CL intensity with annealing.

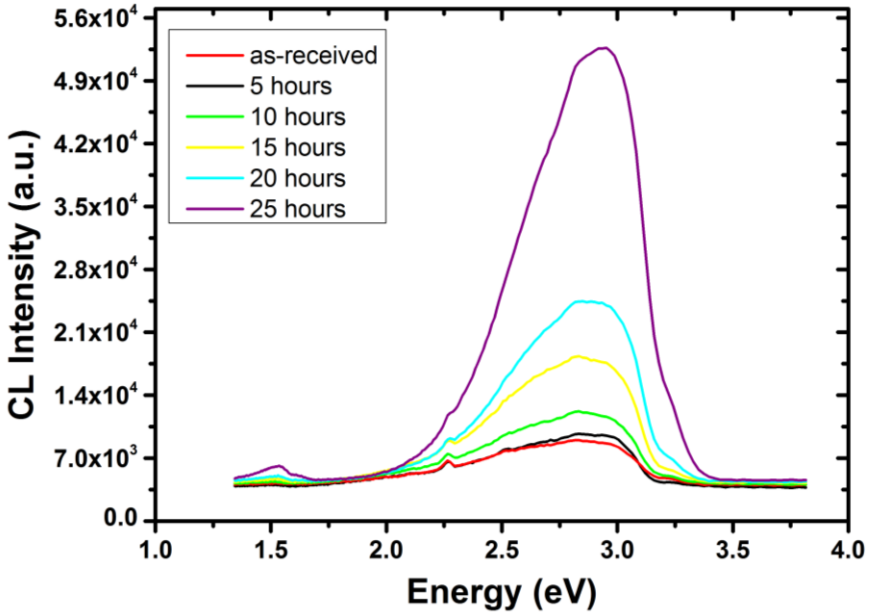

Fig. 7.6 CL spectra of the as received and reduced $SrTiO_3$ single crystals. Measurements are performed with a beam voltage of 20 kV.

To get further insight into the effect of reduction on emission properties, the intense broad band is deconvoluted using Gaussian line shape. Based on the criteria of reduced residual signal, best fitting of the spectra is obtained for six components for all the samples. Fig.7.7a shows the CL spectrum of a sample annealed for 25 hours, along with the deconvolved components. The resolved components are centred at 3.24 eV, 3.04 eV, 2.90 eV, 2.60 eV, 2.26 eV and 2.12 eV and cover the colour range from violet to yellow. Most of these observed emissions are related to the vacancy defects where oxygen vacancy generates donor level just below the conduction band while Sr vacancy leads to acceptor level above the valence band. Emission profile of as received single crystal, which is also deconvolved into six components described above, indicates the formation of numerous states within the band gap of the crystal. This indicates the presence of intrinsic defects which lead to additional electronic levels within the band gap of the material. A detailed study of in-gap energy states generated by intrinsic and extrinsic defects is reported by Yang *et al.* [279].

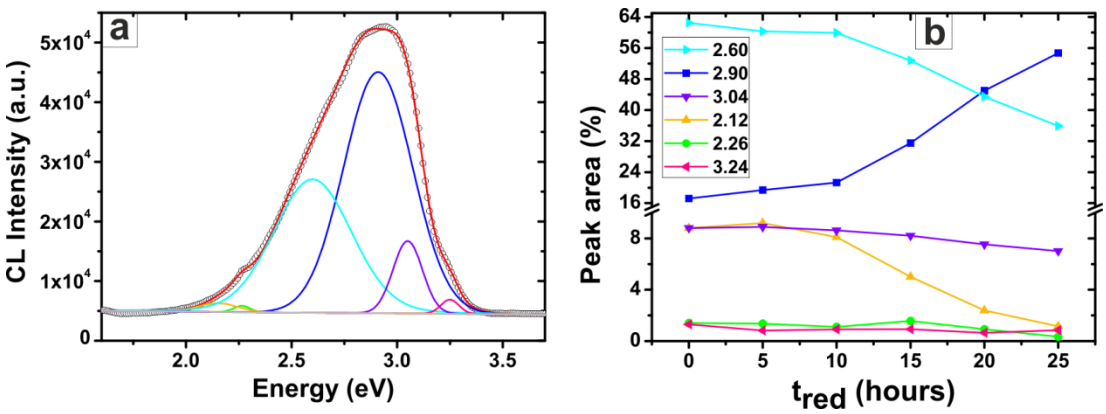

Fig. 7.7 (a) Deconvolved CL spectrum of the 25 hours annealed sample. Black open circles represent the experimental data and red solid line is the corresponding fit. (b) Peak area of the individual deconvolved components (3.24 eV, 3.04 eV, 2.90 eV, 2.60 eV and 2.26 eV) of the as-received and reduced single crystals plotted as a function of annealing time (t_{red}).

The highest energy component which is a weak shoulder of the main broad band is the band-edge transition. The violet (3.04 eV) component is ascribed to the de-excitation of electrons trapped at the donor level created by singly ionized oxygen

vacancy ($V_o^{\bullet}$) to the electronic state created by Sr vacancy ($V_{Sr}^{''}$), i-e., $V_o^{\bullet}$ (at ~0.003 eV [311]) → $V_{Sr}^{''}$ (at ~0.1 eV [311]). The origin of the observed 2.90 eV luminescence is attributed to electrons trapped in the donor state created by doubly ionized oxygen vacancy defect ($V_O^{\bullet\bullet}$) de-exciting to the valence band (VB). This blue emission at room temperature in oxygen deficient $SrTiO_3$ has been reported in several reports [1, 268, 279]. The resolved component centred at around 2.30 eV is reported to originate from charge transfer between Ti^{4+} and O^{2-} within the TiO_6 octahedron while the component appearing at about 2.6 eV is described due to $V_O^{\bullet\bullet} \rightarrow V_{Sr}^{''}$ transition [279].

The vacuum annealing process has a strong influence on the 2.90 eV, 2.60 eV and 2.12 eV components as can be seen in Fig.7.7b, where relative peak area of each deconvolved component is plotted against t_{red}. Thermal reduction of the $SrTiO_3$ single crystals produces oxygen vacancies, whose density increases as t_{red} goes up. This was also reflected in the electrical transport measurements where samples reduced for longer times showed higher conductivity. Hence the rate of $V_O^{\bullet\bullet}$ → VB transition events increases and consequently the intensity of the 2.90 eV emission. However, the intensity of 2.60 eV and 2.12 eV emissions decreases with an increase in t_{red} and is in contrast to that observed by Zhang *et al.* [262]. In their report, the origin of the latter was ascribed to the oxygen vacancy and this emission was most pronounced in samples containing greater oxygen vacancy content. Our observation, however, suggests that the origin of these emissions (2.60 and 2.12 eV) is associated with intrinsic defects whose concentration decreases with thermal annealing. Vacuum annealing appears to have negligibly negligible effect on 2.26, 3.04 and 3.24 eV emissions.

7.4 Summary

$SrTiO_3$ single crystals are thermally annealed in UHV for annealing times (t_{red}) 5-25 hours to incorporate the oxygen vacancies in a controlled manner. The effect of

oxygen vacancies on the electronic structure of $SrTiO_3$ single crystal and the corresponding impact on the physical properties is addressed through electrical resistivity, ESR and CL measurements. The as-received crystals are insulating when measured through standard four-probe method, and show the presence of in-gap states when studied through ESR and CL. ESR measurements show the presence of Mn and Fe impurities with various oxidation states. Thermal annealing in UHV introduces free carriers that result in electrical conductivity rise with t_{red}. ESR investigations of the reduced samples show the presence of Ti^{3+}-V_O centres. Continuous rise in the electrical conductivity with t_{red} suggests the homogeneous distribution of oxygen vacancies within the bulk of the reduced crystals. CL measurements show two broad bands, centred at the blue and IR region, at room temperature in all samples. Deconvolution of the intense broad band in blue region revealed six components centred at 3.24 eV, 3.04 eV, 2.90 eV, 2.60 eV, 2.26 eV and 2.12 eV. Thermal reduction, however, is found to affect the 2.90 eV, 2.60 eV, and 2.12 eV components significantly. The blue emission (~ 2.9 eV) component rises relative to others, while 2.60 and 2.12 eV components are observed to increase with in t_{red}. These trends are associated with an increase in oxygen vacancies and decrease in other intrinsic defects.

Chapter 8

Conclusions

8.1 Overview

This thesis has addressed the role of defects in various properties of $SrTiO_3$ single crystals. Numerous characterization techniques have been used to study both the surface and bulk properties of non-stoichiometric $SrTiO_3$. A number of reconstructions have been controllably produced on $SrTiO_3$(111) surface and the surface reactivity of the reconstructed phases has been investigated through the deposition of large guest molecules. The molecules used are fullerenes C_{60} and C_{70}. Both the bare reconstructed surfaces and surfaces covered with fullerenes are characterized using STM. Four-point probe method and CL spectroscopy along with ESR have been employed to study the bulk properties and defect structure of non-stoichiometric single crystals.

8.2 The surface reactivity of $SrTiO_3$(111)-n×n surfaces

Argon ion sputtering of the $SrTiO_3$(111) singles crystals and subsequent annealing produces a family of (n×n) reconstructions, where n = 2, 3, 4, 5, 6. The 2×2 reconstruction is newly discovered in the present work, while the others have been previously reported. The sputtering process introduces oxygen vacancies in the surface

region, and the degree of disorder depends on the sputtering time. By varying the sputtering time, annealing temperature and environment, **chapter 4** of this thesis has shown that a family of n×n reconstructions can be formed on the $SrTiO_3$(111) surface in a controlled and reproducible manner. Following sputtering for 20 minutes and annealing in the UHV environment produced the 5×5 reconstruction, which is highly oxygen deficient phase among the family of (n×n) surfaces. The rest of the reconstructions i.e. 2, 3, 4, 6 are formed after sputtering the sample for shorter time (6 minutes) and then simply varying the annealing temperature and environment. The family of (n×n) reconstructed surfaces are often observed to co-exist with each other. However, the increase in annealing temperature and oxygen partial pressures allowed the reconstructed surfaces to re-order and evolve from one phase to another.

These patterned surfaces could be controllably used for the growth of functional materials such as fullerenes, and hence bear a great potential in prospective technologies. The nature of self-assembly could vary from one reconstruction to another due to the variation in oxygen non-stoichiometry and surface topography. C**hapter 5 and 6** of the thesis are focused on the exploration of surface reactivity of the oxygen depleted surfaces through the deposition of fullerenes C_{60} and C_{70}. Fullerene molecules were deposited on the reconstructed surfaces held at room temperature. The 5×5 reconstruction appeared to be highly reactive and arranged fullerenes into a variety of unique configurations. The unit cell of the 5×5 reconstruction exhibits a highly reactive site which led not only to the adsorption of individual molecules but also played an important role in stabilizing clusters with magic numbers. In addition to the individual adsorption, the 6-fold and 27-fold clusters were the most frequently observed clusters in the case of C_{60}. The C_{70} molecules, however, did not produce the 27-fold clusters. This could be due the reduced symmetry of the C_{70} molecules that may need more energy to adopt a “standing” orientation and form the 27-fold clusters. The magic clusters exhibited a well-defined geometrical shape and were stable not only at room

temperature but also at higher temperatures (around 200 °C). Upon heating the 5×5 surface covered with fullerenes, further arrangements of molecules were obtained in the form of large ordered overlayers. Both the C_{60} and C_{70} produced hexagonal structures and have epitaxial relationship with the underlying 5×5 substrate. The C_{70} fullerenes adopted both the "lying down" and "standing" orientations on the surface. Fullerene molecules produced a disordered close-packed arrangement on the relatively oxygen enriched surfaces i.e. the 4×4 and 6×6 reconstructions. Upon heating the sample surface, epitaxial overlayers of the fullerenes were formed. The 6×6 reconstructed surface appeared to be less reactive than the 4×4 although being more oxygen deficient. This demonstrated that surface reactivity is determined by both the non-stoichiometry and the surface topography.

8.3 Electrical and optical properties of $SrTiO_3$ single crystals

Chapter 7 of this thesis demonstrates the oxygen vacancy driven electrical and optical properties of UHV annealed single crystals. The reduced $SrTiO_3$ samples showed a monotonic decrease is resistivity with an increase in annealing time, when measured through four-point probe method. Thermal reduction usually results in non-homogeneous distribution of oxygen vacancies in single crystals due to the presence of extended defects in the 'skin region' of crystals. Prolonged annealing in such systems then increases the electrical resistivity of the crystal due to healing of extended defects. In our case, decrease in electrical resistivity upon prolonged annealing indicated the homogeneous distribution of oxygen vacancies within the single crystal for the given annealing parameters. Effect of thermal reduction on the electronic structure and resulting luminescence behaviour of crystal was further studied by ESR and CL spectroscopy. ESR studies, which detect the defect centres with unpaired spin, showed the presence of Fe with various oxidation states and Mn impurities in the as-received single crystals. The reduced samples showed the Ti^{3+} centres associated with oxygen

vacancies which were absent in the as-received single crystals. CL spectroscopy, which is a powerful technique to investigate the electronic states in crystal through directly detection of optical transitions, showed a luminesce behaviour in all the samples, covering the blue and green regions. However, the extent of blue emission in oxygen deficient samples was seen to increase with annealing time. All these studies signify the role of oxygen non-stoichiometry in $SrTiO_3$ single crystals in introducing new properties and/or modification of existing properties.

8.4 Outlook

- The surface chemistry of the $SrTiO_3$(111)- n×n family of reconstructions is composed of TiO_x layers [29] and the availability of atomic resolution STM images of the reconstructed surface would give an opportunity to develop theoretical models using the density functional methods. This would help to extend our knowledge of the reconstructed surfaces. In addition, it would be possible to perform theoretical calculations to determine the adsorption energy of individual molecules as well as the magic clusters.
- The reconstructed surfaces holds a great potential for the self-assembly of fullerenes. It may be interesting to investigate the arrangement of fullerenes C_{60} and C_{70} molecules on the 5×5 reconstruction at low temperatures, where the intra-molecular structure of fullerenes could be observed. In addition, STM could be used in combination with other characterization tools such as scanning tunnelling spectroscopy (STS) to get more insight to the nature of bonding interaction between the molecules and the substrate surface.
- In addition to the lighter empty cage fullerene molecules, work could be extended to investigate the arrangement of endohedral fullerenes such as $Sc_3N@C_{80}$ and $Nd@C_{82}$ molecules. The endohedral fullerenes contain atomic species at the centre, and are of particular interest for applications in solid state

quantum information processing systems. The opto-magnetic properties of such systems could be explored by using the ESR and photoluminescence techniques.

- It would also be interesting to use the patterned surfaces for the growth of nanocrystals such as Cobalt (Co), Nickel (Ni), Iron (Fe) and study their properties using STM in combination with ESR, and CL/PL. This study would allow the development of useful devices, whose structural, luminescence and magnetic properties could be controlled through the deposition of nanocrystals.

Recent years have witnessed the discovery of numerous defect driven properties of $SrTiO_3$ that have been previously unknown. This gives an opportunity to understand and control the defects in a way that may play a defining role in the engineering of novel systems ranging from spintronics to molecular-based electronic devices. I hope that the work presented in this thesis will aid in this process.

References

[1] D. Kan, T. Terashima, R. Kanda, A. Masuno, K. Tanaka, S. Chu, H. Kan, A. Ishizumi, Y. Kanemitsu, Y. Shimakawa, and M. Takano, Nat. Mater. **4**, 816 (2005).

[2] N. Zhou, K. Zhao, H. Liu, Z. Lu, H. Zhao, L. Tian, W. Liu, and S. Zhao, J. Appl. Phys. **105**, 083110 (2009).

[3] K. X. Jin, Y. F. Li, Z. L. Wang, H. Y. Peng, W. N. Lin, A. K. K. Kyaw, Y. L. Jin, K. J. Jin, X. W. Sun, C. Soci, and T. Wu, AIP Adv. **2**, 042131 (2012).

[4] K. Potzger, J. Osten, A. A. Levin, A. Shalimov, G. Talut, H. Reuther, S. Arpaci, D. Bürger, H. Schmidt, T. Nestler, and D. C. Meyer, J. Magn. Magn. Mater. **323**, 1551 (2011).

[5] Z. Q. Liu, W. M. Lü, S. L. Lim, X. P. Qiu, N. N. Bao, M. Motapothula, J. B. Yi, M. Yang, S. Dhar, T. Venkatesan, and Ariando, Phys. Rev. B **87**, 220405(R) (2013).

[6] J. H. Haeni, P. Irvin, W. Chang, R. Uecker, P. Reiche, Y. L. Li, S. Choudhury, W. Tian, M. E. Hawley, B. Craigo, A. K. Tagantsev, X. Q. Pan, S. K. Streiffer, L. Q. Chen, S. W. Kirchoefer, J. Levy, and D. G. Schlom, Nature **430**, 758 (2004).

[7] M. C. Tarun, F. A. Selim, and M. D. McCluskey, Phys. Rev. Lett. **111**, 187403 (2013).

[8] K. Ueno, S. Nakamura, H. Shimotani, A. Ohtomo, N. Kimura, T. Nojima, H. Aoki, Y. Iwasa, and M. Kawasaki, Nat. Mater. **7**, 855 (2008).

[9] M. R. Castell, Surf. Sci. **505**, 1 (2002).

[10] M. Cardona, Phys. Rev. **140**, A651 (1965).

[11] A. Ohtomo, and H. Y. Hwang, Nature **427**, 423 (2004).

[12] N. Reyren, S. Thiel, A. D. Caviglia, L. F. Kourkoutis, G. Hammerl, C. Richter, C. W. Schneider, T. Kopp, A.-S. Rüetschi, D. Jaccard, M. Gabay, D. A. Muller, J.-M. Triscone, and J. Mannhart, Science **317**, 1196 (2007).

[13] H.-L. Lu, L. Zhang, X.-M. Ma, G.-J. Lian, J.-B. Yang, D.-P. Yu, and Z.-M. Liao, Nanoscale **6**, 736 (2014).

[14] A. Brinkman, M. Huijben, M. Van Zalk, J. Huijben, U. Zeitler, J. C. Maan, W. G. Van Der Wiel, G. Rijnders, D. H. A. Blank, and H. Hilgenkamp, Nat. Mater. **6**, 493 (2007).

[15] L. Li, C. Richter, J. Mannhart, and R. C. Ashoori, Nat. Phys. **7**, 762 (2011).

[16] J. A. Bert, B. Kalisky, C. Bell, M. Kim, Y. Hikita, H. Y. Hwang, and K. A. Moler, Nat. Phys. **7**, 767 (2011).

[17] A. D. Caviglia, S. Gariglio, N. Reyren, D. Jaccard, T. Schneider, M. Gabay, S. Thiel, G. Hammerl, J. Mannhart, and J. M. Triscone, Nature **456**, 624 (2008).

[18] C. Cen, S. Thiel, J. Mannhart, and J. Levy, Science **323**, 1026 (2009).

[19] G. Cheng, P. F. Siles, F. Bi, C. Cen, D. F. Bogorin, C. W. Bark, C. M. Folkman, J. W. Park, C. B. Eom, G. Medeiros-Ribeiro, and J. Levy, Nat. Nanotechnol. **6**, 343 (2011).

[20] H. L. Lu, Z. M. Liao, L. Zhang, W. T. Yuan, Y. Wang, X. M. Ma, and D. P. Yu, Sci. Rep. **3**, 2870 (2013).

[21] N. Reyren, M. Bibes, E. Lesne, J. M. George, C. Deranlot, S. Collin, A. Barthélémy, and H. Jaffrès, Phys. Rev. Lett. **108**, 186802 (2012).

[22] G. Herranz, R. Ranchal, M. Bibes, H. Jaffrès, E. Jacquet, J. L. Maurice, K. Bouzehouane, F. Wyczisk, E. Tafra, M. Basletic, A. Hamzic, C. Colliex, J. P. Contour, A. Barthélémy, and A. Fert, Phys. Rev. Lett. **96**, 027207 (2006).

[23] C. H. Ahn, S. Gariglio, P. Paruch, T. Tybell, L. Antognazza, and J.-M. Triscone, Science **284**, 1152 (1999).

[24] F. Silly, A. C. Powell, M. G. Martin, and M. R. Castell, Phys. Rev. B **72**, 165403 (2005).

[25] M. S. J. Marshall, and M. R. Castell, Phys. Rev. Lett. **102**, 146102 (2009).

[26] J. A. Enterkin, A. K. Subramanian, B. C. Russell, M. R. Castell, K. R. Poeppelmeier, and L. D. Marks, Nat. Mater. **9**, 245 (2010).

[27] D. S. Deak, F. Silly, D. T. Newell, and M. R. Castell, J. Phys. Chem. B **110**, 9246 (2006).

[28] M. R. Castell, Surf. Sci. **516**, 33 (2002).

[29] B. C. Russell, and M. R. Castell, J. Phys. Chem. C **112**, 6538 (2008).

[30] D. S. Deak, F. Silly, K. Porfyrakis, and M. R. Castell, Nanotechnology **18**, 075301 (2007).

[31] F. Silly, and M. R. Castell, Phys. Rev. Lett. **94**, 046103 (2005).

[32] F. Silly, and M. R. Castell, ACS Nano **3**, 901 (2009).

[33] D. Choudhury, S. Mukherjee, P. Mandal, A. Sundaresan, U. V. Waghmare, S. Bhattacharjee, R. Mathieu, P. Lazor, O. Eriksson, B. Sanyal, P. Nordblad, A. Sharma, S. V. Bhat, O. Karis, and D. D. Sarma, Phys. Rev. B **84**, 125124 (2011).

[34] A. B. Posadas, C. Mitra, C. Lin, A. Dhamdhere, D. J. Smith, M. Tsoi, and A. A. Demkov, Phys. Rev. B **87**, 144422 (2013).

[35] D. Choudhury, B. Pal, A. Sharma, S. Bhat, and D. D. Sarma, Sci. Rep. **3**, 1433 (2013).

[36] D. Kan, R. Kanda, Y. Kanemitsu, Y. Shimakawa, M. Takano, T. Terashima, and A. Ishizumi, Appl. Phys. Lett. **88**, 191916 (2006).

[37] S. A. Wolf, D. D. Awschalom, R. A. Buhrman, J. M. Daughton, S. von Molnár, M. L. Roukes, A. Y. Chtchelkanova, and D. M. Treger, Science **294**, 1488 (2001).

[38] R. Jansen, Nat. Mater. **12**, 779 (2013).

[39] A. Spinelli, M. A. Torija, C. Liu, C. Jan, and C. Leighton, Phys. Rev. B **81**, 155110 (2010).

[40] Y. Y. Guo, H. M. Liu, D. P. Yu, and J. M. Liu, Phys. Rev. B **85**, 104108 (2012).

[41] M. Choi, F. Oba, and I. Tanaka, Phys. Rev. Lett. **103**, 185502 (2009).

[42] W.-J. Yin, S.-H. Wei, M. M. Al-Jassim, and Y. Yan, Phys. Rev. B **85**, 201201 (2012).

[43] T. Kolodiazhnyi, M. Tachibana, H. Kawaji, J. Hwang, and E. Takayama-Muromachi, Phys. Rev. Lett. **104**, 147602 (2010).

[44] J. Mannhart, and D. G. Schlom, Nature **430**, 620 (2004).

[45] Y.-M. Kim, J. He, M. D. Biegalski, H. Ambaye, V. Lauter, H. M. Christen, S. T. Pantelides, S. J. Pennycook, S. V. Kalinin, and A. Y. Borisevich, Nat. Mater. **11**, 888 (2012).

[46] M. S. J. Marshall, A. E. Becerra-Toledo, D. J. Payne, R. G. Egdell, L. D. Marks, and M. R. Castell, Phys. Rev. B **86**, 125416 (2012).

[47] B. Bryant, C. Renner, Y. Tokunaga, Y. Tokura, and G. Aeppli, Nat. Commun. **2**, 212 (2011).

[48] A. Tselev, P. Ganesh, L. Qiao, W. Siemons, Z. Gai, M. D. Biegalski, A. P. Baddorf, and S. V. Kalinin, ACS Nano **7**, 4403 (2013).

[49] J. F. Watts, and J. Wolstenholme, *An Introduction to Surface Analysis by XPS and AES* (Wiley, 2003).

[50] D. A. Muller, N. Nakagawa, A. Ohtomo, J. L. Grazul, and H. Y. Hwang, Nature **430**, 657 (2004).

[51] B. Bhushan, *Scanning probe microscopy in nanoscience and nanotechnology* (Springer-Verlag, 2010), Vol. 2.

[52] P. Samorì, *Scanning probe microscopies beyond imaging* (Wiley-VCH, 2006).

[53] C. J. Chen, *Introduction to scanning tunneling microscopy* (Oxford University Press, 2008).

[54] D. T. Newell, *D.Phil Thesis* (University of Oxford, 2007).

[55] B. C. Russell, *D.Phil Thesis* (University of Oxford, 2008).

[56] M. S. J. Marshall, *D.Phil Thesis* (University of Oxford, 2009).

[57] C. Wu, *D.Phil Thesis* (University of Oxford, 2010).

[58] D. S. Deak, *D.Phil Thesis* (University of Oxford, 2007).

[59] *Instruction Manual: PSP Vacuum Technology Ion Source ISIS3000* (PSP Vacuum Technology, 1991).

[60] G. Binning, H. Rohrer, C. Gerber, and E. Weibel, Phys. Rev. Lett. **49**, 57 (1982).

[61] G. Binnig, H. Rohrer, C. Gerber, and E. Weibel, Phys. Rev. Lett. **50**, 120 (1983).

[62] M. R. Castell, in *Nanocharacterisation*, edited by A. I. K. a. J. L. Hutchison (Royal Society of Chemistry, Cambridge, U.K., 2007), pp. 66.

[63] *Single Filament Effusion Cell SFC-H-5-SH: Instruction Manual* (Createc Fischer & Co., 2002).

[64] E. Zavoisky., J. Phys. USSR **9**, 211 (1945).

[65] J. A. Weil, and J. R. Bolton, *Electron paramagnetic resonance: elementary theory and practical applications* (Wiley, 2007).

[66] A. Lund, S. Shimada, and M. Shiotani, *Principles and applications of ESR spectroscopy* (Springer, 2010).

[67] P. H. Rieger, *Electron spin resonance: analysis and interpretation* (Royal Society of Chemistry, 2007).

[68] P. Zeeman., Nature **55**, 347 (1897).

[69] D. Schmalbein, G. G. Maresch, A. Kamlowski, and P. Höfer, Appl. Magn. Reson. **16**, 185 (1999).

[70] R. T. Weber, J. Jiang, and D. P. Barr, Billerica, MA, Bruker Instruments **2** (1998).

[71] S. Boggs, and D. Krinsley, *Application of cathodoluminescence imaging to the study of sedimentary rocks* (Cambridge University Press, 2006).

[72] L. J. Brillson, R. E. Viturro, J. L. Shaw, and H. W. Richter, J. Vac. Sci. Technol. A **6**, 1437 (1988).

[73] L. J. Brillson, J. Phys. D: Appl. Phys. **45**, 183001 (2012).

[74] X.-M. Tao, C.-M. Feng, P.-G. Cai, B. Yang, and G.-X. Ye, Solid State Commun. **131**, 419 (2004).

[75] S. X. Zhang, R. D. McDonald, A. Shekhter, Z. X. Bi, Y. Li, Q. X. Jia, and S. T. Picraux, Appl. Phys. Lett. **101**, 202403 (2012).

[76] Q. Shi, C. L. Snow, J. Boerio-Goates, and B. F. Woodfield, J. Chem. Thermodyn. **42**, 1107 (2010).

[77] F. M. Smits, Bell Syst. Tech. J. **37**, 711 (1958).

[78] *Instructions: TM-51320 Indirect heating holder, JEOL Ltd*.

[79] A. Pojani, F. Finocchi, and C. Noguera, Surf. Sci. **442**, 179 (1999).

[80] J. Goniakowski, F. Finocchi, and C. Noguera, Rep. Prog. Phys. **71**, 016501 (2008).

[81] W. J. Lo, and G. A. Somorjai, Phys. Rev. B **17**, 4942 (1978).

[82] L. Wei Jen, C. Yip Wah, and G. A. Somorjai, Surf. Sci. **71**, 199 (1978).

[83] H. Tanaka, and T. Kawai, Surf. Sci. **365**, 437 (1996).

[84] W. M. Sigmund, M. Rotov, F. Aldinger, Q. D. Jiang, J. Brunen, and J. Zegenhagen, Appl. Phys. A **64**, 219 (1997).

[85] Y. Haruyama, Y. Aiura, H. Bando, Y. Nishihara, and H. Kato, J. Electron Spectrosc. Relat. Phenom. **88-91**, 695 (1998).

[86] S. Sekiguchi, M. Fujimoto, M. G. Kang, S. Koizumi, S. B. Cho, and J. Tanaka, Jpn. J. Appl. Phys., Part 1 **37**, 4140 (1998).

[87] S. Sekiguchi, M. Fujimoto, M. Nomura, S. B. Cho, J. Tanaka, T. Nishihara, M. G. Kang, and H. H. Park, Solid State Ionics **108**, 73 (1998).

[88] B. C. Russell, and M. R. Castell, Phys. Rev. B **75**, 155433 (2007).

[89] A. N. Chiaramonti, C. H. Lanier, L. D. Marks, and P. C. Stair, Surf. Sci. **602**, 3018 (2008).

[90] J. Feng, X. Zhu, and J. Guo, Surf. Sci. **614**, 38 (2013).

[91] L. D. Marks, A. Chiaramonti, F. Tran, and P. Blaha, Surf. Sci. **603**, 2179 (2009).

[92] A. Pojani, F. Finocchi, and C. Noguera, Appl. Surf. Sci. **142**, 177 (1999).

[93] H. W. Kroto, J. R. Heath, S. C. O'Brien, R. F. Curl, and R. E. Smalley, Nature **318**, 162 (1985).

[94] W. Kratschmer, L. D. Lamb, K. Fostiropoulos, and D. R. Huffman, Nature **347**, 354 (1990).

[95] W. I. F. David, R. M. Ibberson, J. C. Matthewman, K. Prassides, T. J. S. Dennis, J. P. Hare, H. W. Kroto, R. Taylor, and D. R. M. Walton, Nature **353**, 147 (1991).

[96] R. D. Johnson, C. S. Yannoni, H. C. Dorn, J. R. Salem, and D. S. Bethune, Science **255**, 1235 (1992).

[97] D. R. McKenzie, C. A. Davis, D. J. H. Cockayne, D. A. Muller, and A. M. Vassallo, Nature **355**, 622 (1992).

[98] H. Park, J. Park, A. K. Lim, E. H. Anderson, A. P. Alivisatos, and P. L. McEuen, Nature **407**, 57 (2000).

[99] Y. Maeyoshi, A. Saeki, S. Suwa, M. Omichi, H. Marui, A. Asano, S. Tsukuda, M. Sugimoto, A. Kishimura, K. Kataoka, and S. Seki, Sci. Rep. **2** (2012).

[100] D. M. Guldi, B. M. Illescas, C. M. Atienza, M. Wielopolski, and N. Martin, Chem. Soc. Rev. **38**, 1587 (2009).

[101] J. A. Gardener, G. A. D. Briggs, and M. R. Castell, Phys. Rev. B **80**, 235434 (2009).

[102] X. Zhang, L. Tang, and Q. Guo, J. Phys. Chem. C **114**, 6433 (2010).

[103] Y.-C. Xie, L. Tang, and Q. Guo, Phys. Rev. Lett. **111**, 186101 (2013).

[104] L. Tang, Y. Xie, and Q. Guo, J. Chem. Phys. **135**, 114702 (2011).

[105] L. Tang, and Q. Guo, Phys. Chem. Chem. Phys. **14**, 3323 (2012).

[106] M. Hinterstein, X. Torrelles, R. Felici, J. Rius, M. Huang, S. Fabris, H. Fuess, and M. Pedio, Phys. Rev. B **77**, 153412 (2008).

[107] M. Pedio, R. Felici, X. Torrelles, P. Rudolf, M. Capozi, J. Rius, and S. Ferrer, Phys. Rev. Lett. **85**, 1040 (2000).

[108] A. Ogawa, M. Tachibana, M. Kondo, K. Yoshizawa, H. Fujimoto, and R. Hoffmann, J. Phys. Chem. B **107**, 12672 (2003).

[109] L.-L. Wang, and H.-P. Cheng, Phys. Rev. B **69**, 045404 (2004).

[110] G. Dutton, and X. Y. Zhu, J. Phys. Chem. B **108**, 7788 (2004).

[111] G. Costantini, S. Rusponi, E. Giudice, C. Boragno, and U. Valbusa, Carbon **37**, 727 (1999).

[112] C. Cepek, R. Fasel, M. Sancrotti, T. Greber, and J. Osterwalder, Phys. Rev. B **63**, 125406 (2001).

[113] C. Cepek, A. Goldoni, and S. Modesti, Phys. Rev. B **53**, 7466 (1996).

[114] R. Felici, M. Pedio, F. Borgatti, S. Iannotta, M. Capozi, G. Ciullo, and A. Stierle, Nat. Mater. **4**, 688 (2005).

[115] T. Orzali, D. Forrer, M. Sambi, A. Vittadini, M. Casarin, and E. Tondello, J. Phys. Chem. C **112**, 378 (2007).

[116] M. Casarin, D. Forrer, T. Orzali, M. Petukhov, M. Sambi, E. Tondello, and A. Vittadini, J. Phys. Chem. C **111**, 9365 (2007).

[117] T. Sakurai, X. D. Wang, Q. K. Xue, Y. Hasegawa, T. Hashizume, and H. Shinohara, Prog. Surf. Sci. **51**, 263 (1996).

[118] P. J. Moriarty, Surf. Sci. Rep. **65**, 175 (2010).

[119] L. Sánchez, R. Otero, J. M. a. Gallego, R. Miranda, and N. Martín, Chem. Rev. **109**, 2081 (2009).

[120] X.-Q. Shi, M. Hove, and R.-Q. Zhang, J. Mater. Sci. **47**, 7341 (2012).

[121] Y. Z. Li, M. Chander, J. C. Patrin, J. H. Weaver, L. P. F. Chibante, and R. E. Smalley, Phys. Rev. B **45**, 13837 (1992).

[122] T. Sakurai, X. D. Wang, T. Hashizume, Y. Nishina, H. Shinohara, and Y. Saito, Appl. Surf. Sci. **67**, 281 (1993).

[123] X. D. Wang, T. Hashizume, H. Shinohara, Y. Saito, Y. Nishina, and T. Sakurai, Jpn. J. Appl. Phys. **31**, L983 (1992).

[124] C.-P. Huang, C.-C. Su, and M.-S. Ho, Appl. Surf. Sci. **254**, 7712 (2008).

[125] X. Du, F. Chen, X. Chen, X. Wu, Y. Cai, X. Liu, and L. Wang, Appl. Phys. Lett. **97**, 253106 (2010).

[126] J. I. Pascual, J. Gómez-Herrero, C. Rogero, A. M. Baró, D. Sánchez-Portal, E. Artacho, P. Ordejón, and J. M. Soler, Chem. Phys. Lett. **321**, 78 (2000).

[127] H. Wang, C. Zeng, Q. Li, B. Wang, J. Yang, J. G. Hou, and Q. Zhu, Surf. Sci. **442**, L1024 (1999).

[128] D. Chen, and D. Sarid, Phys. Rev. B **49**, 7612 (1994).

[129] D. Chen, J. Chen, and D. Sarid, Phys. Rev. B **50**, 10905 (1994).

[130] H. Shim, J. Woo, and G. Lee, J. Korean Phys. Soc. **55**, 1707 (2009).

[131] X. Chen, F. Chen, X. Du, S. Yu, Y. Cai, X. Liu, and L. Wang, Surf. Sci. **606**, 1308 (2012).

[132] H. Xu, D. M. Chen, and W. N. Creager, Phys. Rev. Lett. **70**, 1850 (1993).

[133] D. M. Chen, H. Xu, W. N. Creager, and P. Burnett, J. Vac. Sci. Technol. B **12**, 1910 (1994).

[134] T. Hashizume, X. D. Wang, Y. Nishina, H. Shinohara, Y. Saito, Y. Kuk, and T. Sakurai, Jpn. J. Appl. Phys. **31**, L880 (1992).

[135] X. D. Wang, T. Hashizume, H. Shinohara, Y. Saito, Y. Nishina, and T. Sakurai, Phys. Rev. B **47**, 15923 (1993).

[136] J. A. Stroscio, R. M. Feenstra, and A. P. Fein, Phys. Rev. Lett. **57**, 2579 (1986).

[137] X.-D. Wang, Q. Xue, T. Hashizume, H. Shinohara, Y. Saito, Y. Nishina, and T. Sakurai, Appl. Surf. Sci. **76-77**, 334 (1994).

[138] X.-D. Wang, Q. Xue, T. Hashizume, H. Shinohara, Y. Nishina, and T. Sakurai, Phys. Rev. B **49**, 7754 (1994).

[139] A. W. Dunn, E. D. Svensson, and C. Dekker, Surf. Sci. **498**, 237 (2002).

[140] D. Chen, and D. Sarid, Surf. Sci. **329**, 206 (1995).

[141] D. Chen, M. J. Gallagher, and D. Sarid, J. Vac. Sci. Technol. B **12**, 1947 (1994).

[142] A. V. Matetskiy, D. V. Gruznev, A. V. Zotov, and A. A. Saranin, Phys. Rev. B **83**, 195421 (2011).

[143] D. Gruznev, A. Matetskiy, L. Bondarenko, O. Utas, A. Zotov, A. Saranin, J. Chou, C. Wei, M. Lai, and Y. Wang, Nat. Commun. **4**, 1679 (2013).

[144] K. Tsuchie, T. Nagao, and S. Hasegawa, Phys. Rev. B **60**, 11131 (1999).

[145] M. D. Upward, P. Moriarty, and P. H. Beton, Phys. Rev. B **56**, R1704 (1997).

[146] T. Nakayama, J. Onoe, K. Takeuchi, and M. Aono, Phys. Rev. B **59**, 12627 (1999).

[147] D. V. Gruznev, A. V. Matetskiy, L. V. Bondarenko, A. V. Zotov, A. A. Saranin, J. P. Chou, C. M. Wei, and Y. L. Wang, Surf. Sci. **612**, 31 (2013).

[148] H. Xu, D. M. Chen, and W. N. Creager, Phys. Rev. B **50**, 8454 (1994).

[149] M. Fanetti, L. Gavioli, C. Cepek, and M. Sancrotti, Phys. Rev. B **77**, 085420 (2008).

[150] J. C. Dunphy, D. Klyachko, H. Xu, and D. M. Chen, Surf. Sci. **383**, L760 (1997).

[151] D. Klyachko, and D. M. Chen, Phys. Rev. Lett. **75**, 3693 (1995).

[152] D. V. Klyachko, J. M. Lopez-Castillo, J. P. Jay-Gerin, and D. M. Chen, Phys. Rev. B **60**, 9026 (1999).

[153] D. Klyachko, and D. Chen, J. Vac. Sci. Technol. B **14**, 974 (1996).

[154] Y. Z. Li, J. C. Patrin, M. Chander, J. H. Weaver, L. P. F. Chibante, and R. E. Smalley, Science **252**, 547 (1991).

[155] Y. Z. Li, M. Chander, J. C. Patrin, J. H. Weaver, L. P. F. Chibante, and R. E. Smalley, Science **253**, 429 (1991).

[156] Y. Z. Li, J. C. Patrin, M. Chander, J. H. Weaver, K. Kikuchi, and Y. Achiba, Phys. Rev. B **47**, 10867 (1993).

[157] D. K. Biegelsen, R. D. Bringans, J. E. Northrup, and L. E. Swartz, Phys. Rev. B **41**, 5701 (1990).

[158] Q. Xue, T. Ogino, Y. Hasegawa, H. Shinohara, and T. Sakurai, Phys. Rev. B **53**, 1985 (1996).

[159] T. Hashizume, Q. K. Xue, J. Zhou, A. Ichimiya, and T. Sakurai, Phys. Rev. Lett. **73**, 2208 (1994).

[160] T. Hashizume, Q. K. Xue, A. Ichimiya, and T. Sakurai, Phys. Rev. B **51**, 4200 (1995).

[161] T. Sakurai, Q. Xue, T. Hashizume, and Y. Hasegawa, J. Vac. Sci. Technol. B **15**, 1628 (1997).

[162] Q. Xue, T. Hashizume, J. M. Zhou, T. Sakata, T. Ohno, and T. Sakurai, Phys. Rev. Lett. **74**, 3177 (1995).

[163] L. Felix, B. Ralf, S. Jens, O. Frank, R. Michael, and K. Angelika, Nanotechnology **20**, 065606 (2009).

[164] L. Felix, R. Philipp, and K. Angelika, Nanotechnology **20**, 264010 (2009).

[165] F. Loske, and A. Kühnle, Appl. Phys. Lett. **95**, 043110 (2009).

[166] M. Ashino, Y. Sugawara, S. Morita, and M. Ishikawa, Phys. Rev. Lett. **86**, 4334 (2001).

[167] F. Ken-ichi, and S. Motoyoshi, Jpn. J. Appl. Phys. **45**, 2063 (2006).

[168] K. Fukui, and M. Sakai, J. Phys. Chem. B **110**, 21118 (2006).

[169] D. S. Deak, F. Silly, K. Porfyrakis, and M. R. Castell, J. Am. Chem. Soc. **128**, 13976 (2006).

[170] D. S. Deak, K. Porfyrakis, and M. R. Castell, Chem. Commun., 2941 (2007).

[171] C. Lu, E. Zhu, Y. Liu, Z. Liu, Y. Lu, J. He, D. Yu, Y. Tian, and B. Xu, J. Phys. Chem. C **114**, 3416 (2010).

[172] S. Uemura, I. Taniguchi, M. Sakata, and M. Kunitake, J. Electroanal. Chem. **623**, 1 (2008).

[173] H. Unoki, and T. Sakudo, J. Phys. Soc. Jpn. **35**, 1128 (1973).

[174] P. Koidl, K. W. Blazey, W. Berlinger, and K. A. Müller, Phys. Rev. B **14**, 2703 (1976).

[175] K. A. Müller, W. Berlinger, and R. S. Rubins, Phys. Rev. **186**, 361 (1969).

[176] K. W. Blazey, and K. A. Muller, J. Phys. C **16**, 5491 (1983).

[177] W. C. Zheng, H. G. Liu, W. Q. Yang, and B. X. Li, Philos. Mag. **90**, 2899 (2010).

[178] B. W. Faughnan, Phys. Rev. B **5**, 4925 (1972).

[179] O. F. Schirmer, A. Forster, H. Hesse, M. Wohlecke, and S. Kapphan, J. Phys. C **17**, 1321 (1984).

[180] L. Rimai, and G. A. deMars, Phys. Rev. **127**, 702 (1962).

[181] K. A. Müller, Solid State Commun. **9**, 373 (1971).

[182] T. Sakudo, H. Unoki, and Y. Fujii, J. Phys. Soc. Jpn. **21**, 2739 (1966).

[183] K. A. Muller, M. Aguilar, W. Berlinger, and K. W. Blazey, J. Phys.: Condens. Matter **2**, 2735 (1990).

[184] T. W. Kool, and M. Glasbeek, J. Phys.: Condens. Matter **3**, 9747 (1991).

[185] T. W. Kool, and M. Glasbeek, Solid State Commun. **32**, 1099 (1979).

[186] O. F. Schirmer, W. Berlinger, and K. A. Müller, Solid State Commun. **18**, 1505 (1976).

[187] K. A. Müller, J. Phys. (Paris) **42**, 551 (1981).

[188] K. K. A. Muller, and T. W. Kool, *Properties of Perovskites and Other Oxides* (World Scientific, 2010).

[189] R. Merkle, and J. Maier, Angew. Chem., Int. Ed. **47**, 3874 (2008).

[190] B. Bleaney, and A. Abragam, *Electron Paramagnetic Resonance of Transition Ions* (Oxford University Press, 1970).

[191] R. L. Berney, and D. L. Cowan, Phys. Rev. B **23**, 37 (1981).

[192] R. Berney, D. Cowan, and F. Morin, Solid State Commun. **26**, 579 (1978).

[193] M. E. Zvanut, S. Jeddy, E. Towett, G. M. Janowski, C. Brooks, and D. Schlom, J. Appl. Phys. **104**, 064122 (2008).

[194] J. Dashdorj, M. E. Zvanut, and L. J. Stanley, J. Appl. Phys. **107**, 083513 (2010).

[195] S. Kazan, A. G. Şale, J. I. Gatiiatova, V. F. Valeev, R. I. Khaibullin, and F. A. Mikailzade, Solid State Commun. **150**, 219 (2010).

[196] Y. S. Chen, H. Y. Guo, J. Chi Yang, Y. H. Chu, W. F. Wu, and J. G. Lin, J. Appl. Phys. **112**, 123720 (2012).

[197] C. Lenser, A. Kalinko, A. Kuzmin, D. Berzins, J. Purans, K. Szot, R. Waser, and R. Dittmann, Phys. Chem. Chem. Phys. **13**, 20779 (2011).

[198] T. von Waldkirch, K. A. Müller, and W. Berlinger, Phys. Rev. B **5**, 4324 (1972).

[199] T. W. Kool, ArXiv cond-mat. mtrl-sci1201.3386 (2012).

[200] H. Unoki, and T. Sakudo, J. Phys. Soc. Japan **23**, 546 (1967).

[201] W. I. Dobrov, R. F. Vieth, and M. E. Browne, Phys. Rev. **115**, 79 (1959).

[202] E. S. Kirkpatrick, K. A. Müller, and R. S. Rubins, Phys. Rev. **135**, A86 (1964).

[203] R. Baer, G. Wessel, and R. S. Rubins, J. Appl. Phys. **39**, 23 (1968).

[204] R. G. Pontin, E. F. Slade, and D. J. E. Ingram, J. Phys. C **2**, 1146 (1969).

[205] T. W. Kool, and M. Glasbeek, J. Phys.: Condens. Matter **5**, 361 (1993).

[206] A. Lagendijk, M. Glasbeek, and J. D. W. Van Voorst, Chem. Phys. Lett. **20**, 92 (1973).

[207] O. F. Schirmer, W. Berlinger, and K. A. Müller, Solid State Commun. **16**, 1289 (1975).

[208] K. W. Blazey, O. F. Schirmer, W. Berlinger, and K. A. Müller, Solid State Commun. **16**, 589 (1975).

[209] B. W. Faughnan, Phys. Rev. B **4**, 3623 (1971).

[210] F. J. Morin, and J. R. Oliver, Phys. Rev. B **8**, 5847 (1973).

[211] K. A. Müller, T. von Waldkirch, W. Berlinger, and B. W. Faughnan, Solid State Commun. **9**, 1097 (1971).

[212] T. W. Kool, and M. Glasbeek, Solid State Commun. **22**, 193 (1977).

[213] T. W. Kool, ArXiv cond-mat. mtrl-sci1105.0616 (2011).

[214] M. D. Glinchuk, I. P. Bykov, A. M. Slipenyuk, V. V. Laguta, and L. Jastrabik, Phys. Solid State **43**, 841 (2001).

[215] A. Lagendijk, R. J. Morel, M. Glasbeek, and J. D. W. van Voorst, Chem. Phys. Lett. **12**, 518 (1972).

[216] R. S. de Biasi, and M. L. N. Grillo, Mater. Res. **15**, 473 (2012).

[217] I. Bykov, M. Makarova, V. Trepakov, A. Dejneka, L. Yurchenko, A. Jäger, and L. Jastrabik, Phys. Status Solidi B **250**, 821 (2013).

[218] F. La Mattina, J. G. Bednorz, S. F. Alvarado, A. Shengelaya, and H. Keller, Appl. Phys. Lett. **93**, 022102 (2008).

[219] T. W. Kool, H. J. d. Jong, and M. Glasbeek, J. Phys.: Condens. Matter **6**, 1571 (1994).

[220] F. La Mattina, J. G. Bednorz, S. F. Alvarado, A. Shengelaya, K. A. Müller, and H. Keller, Phys. Rev. B **80**, 075122 (2009).

[221] S. A. Basun, U. Bianchi, V. E. Bursian, A. A. Kaplyanskii, W. Kleemann, L. S. Sochava, and V. S. Vikhnin, J. Lumin. **66–67**, 526 (1995).

[222] S. F. Alvarado, F. La Mattina, and J. G. Bednorz, Appl. Phys. A **89**, 85 (2007).

[223] K. A. Muller, and W. Berlinger, J. Phys. C **16**, 6861 (1983).

[224] H. D. Meierling, Phys. Status Solidi B **43**, 191 (1971).

[225] A. G. Badalyan, D. Azamat, R. A. Babunts, E. V. Neverova, A. Dejneka, V. A. Trepakov, and L. Jastrabik, Phys. Solid State **55**, 1454 (2013).

[226] D. V. Azamat, A. Dejneka, J. Lančok, V. A. Trepakov, L. Jastrabik, and A. G. Badalyan, J. Appl. Phys. **113**, 174106 (2013).

[227] K. W. Blazey, J. M. Cabrera, and K. A. Müller, Solid State Commun. **45**, 903 (1983).

[228] V. V. Laguta, I. V. Kondakova, I. P. Bykov, M. D. Glinchuk, A. Tkach, P. M. Vilarinho, and L. Jastrabik, Phys. Rev. B **76**, 054104 (2007).

[229] A. G. Badalyan, C. B. Azzoni, P. Galinetto, M. C. Mozzati, J. Rosa, A. Deyneka, L. Jastrabik, and V. A. Trepakov, Ferroelectrics **367**, 89 (2008).

[230] C. B. Azzoni, M. C. Mozzati, A. Paleari, V. Massarotti, M. Bini, and D. Capsoni, Solid State Commun. **114**, 617 (2000).

[231] A. G. Badalyan, C. B. Azzoni, P. Galinetto, M. C. Mozzati, V. A. Trepakov, M. Savinov, A. Deyneka, L. Jastrabik, and J. Rosa, J. Phys.: Conf. Ser. **93**, 012012 (2007).

[232] A. G. Badalyan, P. P. Syrnikov, C. B. Azzoni, P. Galinetto, M. C. Mozzati, J. Rosa, V. A. Trepakov, and L. Jastrabik, J. Appl. Phys. **104**, 033917 (2008).

[233] K. A. Müller, Phys. Rev. Lett. **2**, 341 (1959).

[234] R. A. Serway, W. Berlinger, K. A. Müller, and R. W. Collins, Phys. Rev. B **16**, 4761 (1977).

[235] D. V. Azamat, A. Dejneka, J. Lancok, V. A. Trepakov, L. Jastrabik, and A. G. Badalyan, J. Appl. Phys. **111**, 104119 (2012).

[236] D. V. Azamat, A. G. Badalyan, A. Dejneka, V. A. Trepakov, L. Jastrabik, and Z. Frait, J. Phys. Chem. Solids **73**, 822 (2012).

[237] O. F. Schirmer, and K. A. Müller, Phys. Rev. B **7**, 2986 (1973).

[238] P. P. J. van Engelen, and J. C. M. Henning, Phys. Lett. A **25**, 733 (1967).

[239] Z. Yuan, W. Xiao-Xuan, H. Lv, and Z. Wen-Chen, J. Phys. Chem. Solids **68**, 1652 (2007).

[240] K. W. Blazey, R. Koch, and K. A. Müller, Mater. Res. Bull. **16**, 1149 (1981).

[241] V. V. Laguta, M. D. Glinchuk, R. O. Kuzian, S. N. Nokhrin, I. P. Bykov, J. Rosa, L. Jastrabík, and M. G. Karkut, J. Phys.: Condens. Matter **14**, 13813 (2002).

[242] C. Lee, J. Destry, and J. L. Brebner, Phys. Rev. B **11**, 2299 (1975).

[243] O. N. Tufte, and P. W. Chapman, Phys. Rev. **155**, 796 (1967).

[244] H. P. R. Frederikse, W. R. Thurber, and W. R. Hosler, Phys. Rev. **134**, A442 (1964).

[245] D. Parker, and J. Yahia, Phys. Rev. **169**, 605 (1968).

[246] C. Lee, J. Yahia, and J. L. Brebner, Phys. Rev. B **3**, 2525 (1971).

[247] H. Yamada, and G. R. Miller, J. Solid State Chem. **6**, 169 (1973).

[248] R. Astala, and P. D. Bristowe, Model. Simul. Mater. Sci. Eng. **9**, 415 (2001).

[249] D. D. Cuong, B. Lee, K. M. Choi, H.-S. Ahn, S. Han, and J. Lee, Phys. Rev. Lett. **98**, 115503 (2007).

[250] Z. Hou, and K. Terakura, J. Phys. Soc. Jpn. **79**, 114704 (2010).

[251] K. Szot, W. Speier, G. Bihlmayer, and R. Waser, Nat. Mater. **5**, 312 (2006).

[252] R. H. Wang, Y. M. Zhu, and S. M. Shapiro, Phys. Rev. Lett. **80**, 2370 (1998).

[253] A. E. Paladino, L. G. Rubin, and J. S. Waugh, J. Phys. Chem. Solids **26**, 391 (1965).

[254] K. Szot, W. Speier, R. Carius, U. Zastrow, and W. Beyer, Phys. Rev. Lett. **88**, 075508 (2002).

[255] Z. Q. Liu, D. P. Leusink, X. Wang, W. M. Lü, K. Gopinadhan, A. Annadi, Y. L. Zhao, X. H. Huang, S. W. Zeng, Z. Huang, A. Srivastava, S. Dhar, T. Venkatesan, and Ariando, Phys. Rev. Lett. **107**, 146802 (2011).

[256] K. S. Takahashi, D. Matthey, D. Jaccard, and J. M. Triscone, Ann. Phys. **13**, 68 (2004).

[257] M. Schultz, and L. Klein, Appl. Phys. Lett. **91**, 151104 (2007).

[258] C. Rodenbücher, S. Wicklein, R. Waser, and K. Szot, Appl. Phys. Lett. **102**, 101603 (2013).

[259] H. Gross, N. Bansal, Y.-S. Kim, and S. Oh, J. Appl. Phys. **110**, 073704 (2011).

[260] X. D. Zhu, Y. Y. Fei, H. B. Lu, and G. Z. Yang, Appl. Phys. Lett. **87**, 051903 (2005).

[261] T. Hasegawa, M. Shirai, and K. Tanaka, J. Lumin. **87–89**, 1217 (2000).

[262] J. Zhang, S. Walsh, C. Brooks, D. G. Schlom, and L. J. Brillson, J. Vac. Sci. Technol. B **26**, 1466 (2008).

[263] J. Zhang, D. Doutt, T. Merz, J. Chakhalian, M. Kareev, J. Liu, and L. J. Brillson, Appl. Phys. Lett. **94**, 092904 (2009).

[264] R. A. Rosenberg, Y. Choi, K. Vijayalakshmi, M. Kareev, J. Tchakhalian, S. Balaz, and L. J. Brillson, Appl. Phys. Lett. **102**, 192910 (2013).

[265] L. Grabner, Phys. Rev. **177**, 1315 (1969).

[266] T. Feng, Phys. Rev. B **25**, 627 (1982).

[267] J. Rho, S. Jang, Y. D. Ko, S. Kang, D.-W. Kim, J.-S. Chung, M. Kim, M. Han, and E. Choi, Appl. Phys. Lett. **95**, 241906 (2009).

[268] J. Rho, S. Jung, S. Shin, J. Kwon, M. Kim, J. Song, and E. Choi, J. Lumin. **130**, 1687 (2010).

[269] J. Rho, and E. Choi, J. Lumin. **131**, 69 (2011).

[270] J. Rho, J. Kim, S. Shin, J. Kwon, M. Kim, J. Song, and E. Choi, J. Lumin. **130**, 1784 (2010).

[271] H. Ihrig, J. H. T. Hengst, and M. Klerk, Z. Phys. B: Condens. Matter **40**, 301 (1981).

[272] M. Aguilar, and F. Agullo-Lopez, J. Appl. Phys. **53**, 9009 (1982).

[273] R. Leonelli, and J. L. Brebner, Solid State Commun. **54**, 505 (1985).

[274] F. Chen, H. Liu, K. Wang, H. Yu, S. Dong, X. Chen, X. Jiang, Z. Ren, and J. Liu, J. Phys.: Condens. Matter **17**, L467 (2005).

[275] V. S. Vikhnin, R. I. Eglitis, and G. Borstel, Ferroelectrics **299**, 21 (2004).

[276] R. Eglitis, E. Kotomin, and G. Borstel, J. Phys.: Condens. Matter **14**, 3735 (2002).

[277] R. Plugaru, A. Cremades, and J. Piqueras, J. Phys.: Condens. Matter **16**, S261 (2004).

[278] T. R. N. Kutty, and M. Avudaithai, Mater. Res. Bull. **25**, 821 (1990).

[279] K.-H. Yang, T.-Y. Chen, N.-J. Ho, and H.-Y. Lu, J. Am. Ceram. Soc. **94**, 1811 (2011).

[280] K. D. Sung, R. Kumar, A. Pratap Singh, C. S. Kim, K. J. Yee, and J. H. Jung, Phys. B **405**, 2581 (2010).

[281] M. A. Henderson, Surf. Sci. **419**, 174 (1999).

[282] Z. Wang, F. Yang, Z. Zhang, Y. Tang, J. Feng, K. Wu, Q. Guo, and J. Guo, Phys. Rev. B **83**, 155453 (2011).

[283] F. Li, Z. Wang, S. Meng, Y. Sun, J. Yang, Q. Guo, and J. Guo, Phys. Rev. Lett. **107**, 036103 (2011).

[284] O. Bondarchuk, and I. Lyubinetsky, Rev. Sci. Instrum. **78**, 113907 (2007).

[285] M. Blanco-Rey, J. Abad, C. Rogero, J. Mendez, M. F. Lopez, J. A. Martin-Gago, and P. L. de Andres, Phys. Rev. Lett. **96**, 055502 (2006).

[286] Y. Sugimoto, P. Pou, M. Abe, P. Jelinek, R. Pérez, S. Morita, and O. Custance, Nature **446**, 64 (2007).

[287] S. Morita, J. Vac. Sci. Technol. A **31**, 050802 (2013).

[288] G.-z. Zhu, G. Radtke, and G. A. Botton, Nature **490**, 384 (2012).

[289] D. M. Kienzle, and L. D. Marks, CrystEngComm **14**, 7833 (2012).

[290] Y. Jiang, Y. Wang, J. Sagendorf, D. West, X. Kou, X. Wei, L. He, K. L. Wang, S. Zhang, and Z. Zhang, Nano Lett. **13**, 2851 (2013).

[291] D. S. Deak, Mater. Sci. Technol. **23**, 127 (2007).

[292] S. A. Krasnikov, S. I. Bozhko, K. Radican, O. Lübben, B. E. Murphy, S.-R. Vadapoo, H.-C. Wu, M. Abid, V. N. Semenov, and I. V. Shvets, Nano Res. **4**, 194 (2011).

[293] M. Grobis, X. Lu, and M. F. Crommie, Phys. Rev. B **66**, 161408 (2002).

[294] W. W. Pai, C.-L. Hsu, M. C. Lin, K. C. Lin, and T. B. Tang, Phys. Rev. B **69**, 125405 (2004).

[295] E. Giudice, E. Magnano, S. Rusponi, C. Boragno, and U. Valbusa, Surf. Sci. **405**, L561 (1998).

[296] E. I. Altman, and R. J. Colton, Phys. Rev. B **48**, 18244 (1993).

[297] S. I. Bozhko, S. A. Krasnikov, O. Lübben, B. E. Murphy, K. Radican, V. N. Semenov, H. C. Wu, B. Bulfin, and I. V. Shvets, Phys. Rev. B **84**, 195412 (2011).

[298] N. Katsonis, A. Marchenko, and D. Fichou, Adv. Mater. **16**, 309 (2004).

[299] P. Wang, H.-J. Zhang, Y.-J. Li, C.-Q. Sheng, Y. Shen, H.-Y. Li, S.-N. Bao, and H.-N. Li, Phys. Rev. B **85**, 205445 (2012).

[300] A. J. Maxwell, P. A. Brühwiler, D. Arvanitis, J. Hasselström, M. K. J. Johansson, and N. Mårtensson, Phys. Rev. B **57**, 7312 (1998).

[301] C. Lin, and A. A. Demkov, Phys. Rev. Lett. **111**, 217601 (2013).

[302] S. Middey, C. Meneghini, and S. Ray, Appl. Phys. Lett. **101**, 042406 (2012).

[303] Z. Q. Liu, W. M. Lü, S. L. Lim, X. P. Qiu, N. N. Bao, M. Motapothula, J. B. Yi, M. Yang, S. Dhar, T. Venkatesan, and Ariando, Phys. Rev. B **87**, 220405 (2013).

[304] J. F. Schooley, W. R. Hosler, and M. L. Cohen, Phys. Rev. Lett. **12**, 474 (1964).

[305] C. Lee, J. Yahia, and J. Brebner, Phys. Rev. B **3**, 2525 (1971).

[306] G. Herranz, M. Basletić, M. Bibes, C. Carrétéro, E. Tafra, E. Jacquet, K. Bouzehouane, C. Deranlot, A. Hamzić, J. M. Broto, A. Barthélémy, and A. Fert, Phys. Rev. Lett. **98**, 216803 (2007).

[307] J. Carrasco, F. Illas, N. Lopez, E. A. Kotomin, Y. F. Zhukovskii, R. A. Evarestov, Y. A. Mastrikov, S. Piskunov, and J. Maier, Phys. Rev. B **73**, 064106 (2006).

[308] C. Mitra, C. Lin, J. Robertson, and A. A. Demkov, Phys. Rev. B **86**, 155105 (2012).

[309] D. Ricci, G. Bano, G. Pacchioni, and F. Illas, Phys. Rev. B **68**, 224105 (2003).

[310] K. Blazey, R. Koch, and J. Bednorz, J. de Physique, Coll. **41**, C6 (1980).

[311] R. Moos, and K. H. Hardtl, J. Am. Ceram. Soc. **80**, 2549 (1997).